

Galvanic Porous Silicon: Processing and Characterization for Nanoenergetics

by

Collin R. Becker

B.S. Chemical and Biological Engineering, University of Colorado, 2005

M.S. Mechanical Engineering, University of Colorado, 2008

A thesis submitted to the

Faculty of the Graduate School of the

University of Colorado in partial fulfillment

of the requirements for the degree of

Doctor of Philosophy

Department of Mechanical Engineering

2010

This thesis entitled:
Galvanic Porous Silicon: Processing and Characterization for Nanoenergetics
written by Collin R. Becker
has been approved for the Department of Mechanical Engineering

Conrad R. Stoldt

Victor M. Bright

Date_____

The final copy of this thesis has been examined by the signatories, and we find that both the content and the form meet acceptable presentation standards of scholarly work in the above mentioned discipline.

Becker, Collin R. (Ph.D., Mechanical Engineering, University of Colorado, 2010)

Galvanic Porous Silicon: Processing and Characterization for Nanoenergetics

Thesis directed by Prof. Conrad Stoldt

Porous silicon (PS) is a silicon (Si) based material composed of pores with diameters ranging from several nanometers to several micrometers. Typically PS is formed by electrochemically etching a Si wafer in a hydrofluoric acid (HF) based electrolyte. This route requires a custom built etch cell and a power supply and is difficult to integrate with the batch processing techniques of conventional Microsystems fabrication. In the first part of this work, a galvanic etching approach is used to fabricate PS in which neither a power supply nor custom etch cell are required. Galvanic etching methods are developed to fabricate thick, mechanically stable PS on lightly doped p-type Si wafers. A detailed characterization of galvanic PS, including specific surface area measurements, etch rates, high resolution transmission electron microscopy, and photoluminescence measurements, is also presented. As a means to model galvanic Si etching (corrosion) on Si Microsystems, we present a finite element method (FEM) enabled simulation.

In the second half of this work, galvanic PS for nanoenergetics is investigated. Nanoenergetic composite materials are composed of nanometer-scale fuel and oxidizer components that have energy release rates much greater than the bulk materials. In this case, PS fuel is impregnated with sodium perchlorate (NaClO_4) oxidizer to yield a nanoenergetic composite. The data presented here include the first measurements of nanoenergetic PS using thermal analysis techniques including bomb calorimetry and differential scanning calorimetry (DSC). Additionally, the reaction products are revealed to be composed of nearly spherical,

interconnected nanoparticles of amorphous silica. Using bomb calorimetry, the heat of reaction of galvanic PS- NaClO_4 nanoenergetic composites is determined to be 9.9 ± 1.8 kJ/g and 27.3 ± 3.2 kJ/g of PS when ignited under N_2 and O_2 , respectively. DSC, coupled with Fourier transform infrared spectroscopy (FTIR) data, reveals that the energy output is dependent on the hydrogen termination of the PS. Lastly, the flame propagation velocity of the PS- NaClO_4 composite is measured with a novel on-chip diagnostic technique and high-speed video data taken at 930,000 frames per second. A velocity averaging $\sim 3,050$ m/s is observed, and is currently the fastest velocity reported for nanoenergetic materials.

Dedication

This thesis is dedicated to my parents for their unwavering love
and support in my every endeavor.

Acknowledgments

I must first say an enormous thank you to my friends who have through the years provided laughter, camaraderie, and adventure. Without you, I would not be the person I am and this thesis would not have been possible. Some of you I have known since preschool and others for just a few years, but you have added so much to my life. Whether we made turns in deep powder, mountain biked Colorado singletrack, enjoyed happy hour burgers, or stayed up late finishing big projects I thank you for being part of my life and I am looking forward to what the future holds.

Thank you to my former lab mates Dr. Brian Larsen, Dr. Dave Miller, Dr. Steve Lammers, and Michael Haag for friendship and professional advice. Thank you especially to Dave as your research was a major motivation behind this thesis. I would also like to thank my undergraduate research advisor from the CU Chemical and Biological Engineering Department, Prof. Richard Noble and his graduate student at the time, Dr. Dean Camper for introducing me to the research process. Thank you also to the many people at the University of Colorado (faculty, staff, and students) who have helped me over the years; this campus and the people who work and study here are truly amazing! I especially acknowledge my committee members for taking time to provide feedback and guidance on this thesis.

Thank you to the many people at the Army Research Lab for providing both financial and professional support for my research. Dr. Brett Piekarski (also on my committee!), Dr. Luke Currano, Wayne Churaman and Dr. Chris Morris deserve big thanks for involving me with nanoenergetic research. The collaboration between CU and ARL has been very successful and I am very glad you took the risk of accepting me through the SMART program. Also, thank you to Brian Isaacson for his extremely rapid wafer processing!

Thank you to Steven Apperson from the University of Missouri for help in the final design of the on-chip porous silicon velocity measurements and valuable discussions about measurement techniques for nanoenergetics.

Thank you to the Department of Defense SMART scholarship for providing funding for me to pursue this research. Also thank you to the Army Research Office (grant no. W911NF-06-1-0342) for funding during the initial phases of this work.

Thank you to Bobby Gill and Brendan Hanrahan for being excellent roommates in the very strange place that is Beltsville, Maryland.

Thank you to Janie Lorber for being an amazing girlfriend, making me laugh, cooking delicious dinners, and being very supportive especially during the last months of this work.

Finally, thank you to my advisor Conrad Stoldt. Your patience, guidance, and financial support were instrumental in this work and in helping me develop professionally. Your mentorship and friendship have meant so much to me during my time at CU.

Contents

Chapter

1. Introduction of the Thesis	1
1.1 Introduction.....	1
1.1.1 Research Theme and Scope	1
1.1.2 Motivation: Porous Silicon as an Energetic Material	1
1.2 Literature Review.....	2
1.2.1 Porous Silicon Literature Review	2
1.2.2 Nanoenergetics Literature Review.....	9
1.3 Research Significance	12
2. Modeling Galvanic Corrosion.....	14
2.1 Preface.....	14
2.2 Introduction.....	15
2.3 Experimental	19
2.3.1 Specimens and Electrochemical Characterization	19
2.4 Numerical Analysis.....	21
2.4.1 Fundamental Assumptions.....	21
2.4.2 Accounting for Electrochemical Kinetics	25
2.4.3 Validation of the Finite Element Method	29
2.5 Results and Discussion	31
2.5.1 Examination of Uniformity of Corrosion Using Focused Ion Beam	31

2.5.2 Examination of Electrochemical Phenomena Using Finite Element Method and Comparison to Focused Ion Beam Results	35
2.6 Conclusion	43
3. Galvanic Etching of Si	45
3.1 Preface.....	45
3.2 Introduction.....	45
3.2.1 Electrochemical Etching Methods	47
3.2.2 Galvanic Corrosion Etching Methods.....	48
3.3 Morphological Characterization	49
3.3.1 Electrochemical PS	49
3.3.2 Galvanic Porous Silicon.....	57
3.4 Galvanic Porous Silicon Microstructure	62
3.5 Conclusion	68
4. Thermal Analysis of the Exothermic Reaction between Galvanic Porous Silicon and Sodium Perchlorate	69
4.1 Preface.....	69
4.2 Introduction.....	69
4.3 Galvanic PS Samples for Thermal Analysis	71
4.4 Gravimetric Analysis of PS-NaClO ₄	74
4.5 Thermal Analysis Results and Discussion	76
4.6 Conclusion	84

5. Nanometer Amorphous Silica Particles Resulting from the Combustion of Porous Silicon Based Nanoenergetic Composites	86
5.1 Preface.....	86
5.2 Introduction.....	86
5.3 Sample Preparation	88
5.4 Results and Discussion	89
5.5 Conclusion	96
6. Galvanic Porous Silicon Composites for High Velocity Nanoenergetics	97
6.1 Preface.....	97
6.2 Introduction.....	97
6.3 Results and Discussion	98
6.4 Conclusion	108
7. Conclusions and Future Directions	109
7.1 Conclusions.....	109
7.2 Future Directions	112
8. Bibliography	117

Appendix

A. Techniques for Preparation of Highly reactive Electrochemical Porous Silicon.....	128
A.1. Preface.....	128
A.2. Summary of Electrochemical PS Ignition Studies	129
A.3. Raman Characterization of PS Stress.....	132

A.3.1. Sample Preparation	132
A.3.2. Laser Ignition Testing	133
A.3.3. Raman Spectroscopy Characterization	134
B. Porous Silicon Velocity Strips: Processing and Additional Characterization.....	138
B.1. Preface	138
B.2. Porous silicon velocity strip process flow	138
B.3. Gas Adsorption Measurements	139
B.4. Porous Silicon SEM Analysis	141
B.5. Velocity Analysis	142

Tables

Table 2.1: Analogy between electrical and thermal units in FEM.	25
Table 2.2: Key parameters obtained from the potentiodynamic measurement of Si in the three electrolyte solutions.	28
Table 6.1: PS properties for 3:1 and 20:1 PS.....	103
Table 6.2: Flame propagation velocities for 3:1 and 20:1 PS.....	107
Table A.1: Etch conditions, drying methods, and energetic reaction strength: 25% HF/EtOH.	130
Table A.2: Etch conditions, drying methods, and energetic reaction strength: 33% HF/EtOH.	130
Table A.3: Raman spectroscopy results and predicted stress in the sample at several laser power densities and accumulation times.....	137

Figures

Figure 1.1: Conventional electrochemical setup for PS fabrication with optical images of typical PS shown to the left.	4
Figure 1.2: Galvanic corrosion mechanism of PS. The noble metal Pt serves as the cathode while Si serves as the anode. A silicon nitride (Si_3N_4) etch mask defines the active area of Si for PS formation.	6
Figure 1.3: The PS formation mechanism. Step 1: An anodic bias promotes a hole to the surface and a nucleophilic attack from one fluoride ion replaces a hydrogen made vulnerable by the hole. Step 2: A second nucleophilic attack from a fluoride ion species on the remaining hydrogen injects an electron. Step 3: The Si-F bonds polarize the Si backbonds which are attacked by H^+ from HF or H_2O	8
Figure 1.4: Timeline of energetic porous silicon research.	11
Figure 2.1: Optical image of four-point resistive probe immersed in UDHF: H_2O (1:1) for 24 minutes (a) and UDHF:Triton (20:1) for 12 minutes (b). (c) shows a device without gold after immersion in an HF based electrolyte.	17
Figure 2.2: Boundary conditions and governing equations for galvanic corrosion. For the system (a), and interface region (b), an infinitesimal element of the electrolyte (c) is used to show charge balance.	23
Figure 2.3: Measured Tafel profiles for Si/Au in the three HF electrolytes. The inset shows the profiles as represented using piecewise regions. The arrows at the top of the plot indicate the direction of the voltage scan from the OCP of either Au or Si.	27
Figure 2.4: Validation of FEM model for a simple geometry: The potential profiles for the electrolyte along the surface of the anode and cathode for three different electrolyte depths. The electric field potential distribution (and mesh) is shown in the inset.	30
Figure 2.5: Four-point probe structure after 24 minutes of immersion in (UDHF: H_2O), including: (a) entire structure (oriented as in Fig. 1 (a)), (b) shows the Au-Si interface (c) the gage section of the device - revealing “macroscopic” pitting and pores, (d) the cross section of the region near the gold, and (e) cross section of the gage region.	32
Figure 2.6: Four-point probe structure after 12 minutes of immersion in UDHF:Triton (Figure 2.1 (b)). The cuts reveal a nearly uniform PS thickness across the device contrary to the UDHF: H_2O device. (b) is a cross section on the Si lead near the gold cathode that shows a uniform PS depth across the entire cut, (c) is a cut near the Au cathode, and (d) is a cut in the gage section.	33
Figure 2.7: Thickness variation along a specific lead of the UDHF: H_2O resistive probe structure examined using FIB milling, shown relative to visual appearance at the same location.	

The micrograph insets identify the PS thickness along the arm. The optical inset identifies where the cut was made on the lead. Three separate SEM images were spliced to show the full length of the lead.....	34
Figure 2.8: Dynamic SIMS measurement of phosphorous (^{31}P) in a pristine SOI sample from SOIMUMPS fabrication run 14.....	35
Figure 2.9: Empirical (resistive probe) and analytic (FEM) data for current density vs. SAR for resistive probe structures, where corrosion is limited to the top Si surface.....	37
Figure 2.10: FEM results from a four-point probe model in UDHF:Triton showing the effect of device size on corrosion current density. (a) shows a device with gold pad dimensions on the order of a meter, (b) shows a device with dimensions on the order of 10 cm, (c) shows a device with dimensions on the order of 1 mm, and (d) shows the actual device dimensions on the order of 100 μm	41
Figure 2.11: Plots of FEM data for unique SAR values of a four-point resistive probe and a simple square geometry model. The results from each model for each HF-based electrolyte are nearly colinear (the arrow for each electrolyte is overlapping both models), with the results from the four-point resistive probe model being slightly larger than the square geometry model.	42
Figure 3.1: Gas adsorption isotherm of porous silicon (18 mA/cm^1 in 25% HF/EtOH electrolyte).	51
Figure 3.2: BJH adsorption cumulative pore volume of porous silicon (18mA/cm^2 in 25% HF/EtOH electrolyte).....	52
Figure 3.3: BJH adsorption pore volume distribution of porous silicon (18 mA/cm^2 in 25% HF/EtOH electrolyte).....	52
Figure 3.4: Pores sizes and surface area for 1:1 and 2:1 PS at varying current densities for a 30 minute etch time.....	53
Figure 3.5: Gas adsorption curves for electrochemical PS formed at varying current densities in 2:1 (black, solid) and 1:1 (red, dotted) HF:EtOH.	53
Figure 3.6: Gas adsorption curve for PS formed on p^{++}Si	55
Figure 3.7: Pore diameters and surface areas of PS formed on p^{++}Si	55
Figure 3.8: Porosity of electrochemical PS.....	56
Figure 3.9: Etch depth for electrochemical PS samples are 30 minutes of etching.....	57
Figure 3.10: The backside of a Si wafer showing the Pt thin film after 30 minute etching in 3:1 HF:EtOH composed of 2.4% by volume H_2O_2 without a Pt anneal (a), and with a Pt	

anneal (b). In (a) dark regions appear where Pt has peeled and PS has been generated and in (b) the Pt thin film is left intact.	58
Figure 3.11: A) SEM image of the ignitor wire after 10 minutes of galvanic etching. B) Optical image of the ignitor wire.	59
Figure 3.12: General etch depth trends based on H_2O_2 concentration and SAR for p^+ Si without performing an anneal after Pt deposition.	60
Figure 3.13: Gas Adsorption for galvanic PS	61
Figure 3.14: PL spectra of 30 min and 60 min galvanic PS	63
Figure 3.15: PS powder (orange PL) in a glass vial under UV illumination after being broken apart from the Si wafer in an ultrasonic bath. Some of the powder has coated the walls of the vial, while in the bottom the original PS chips are submerged in ethanol. The ethanol is not anhydrous and the vial was sealed in laboratory air.	64
Figure 3.16: XRD spectra of 30 and 60 min PS powders.	65
Figure 3.17: High resolution TEM images of PS powder. a),b) 30 minute PS powder. c) 60 minute PS powder.	66
Figure 3.18 High resolution TEM image of 30 minute PS powder showing Si crystallites with unique alignment. The red lines help guide the eye to the alignment of the Si crystallites.	67
Figure 3.19: Raman spectra of 60 and 30 minute PS thin films and Si single crystal substrate..	68
Figure 4.1: Cross sections of PS formed after (a) 30 minute and (b) 60 minute etch.....	73
Figure 4.2: (a) The solid line represents the theoretical capacity of PS for NaClO_4 assuming all void space is filled with NaClO_4 . Experimental and theoretical data for the stoichiometry are also shown. Inset: Schematic showing an idealized PS structure filled with oxidizer. (b) Bomb calorimetry results for 30 minute PS. The theoretical heat of reaction corresponding to equation (4.3) is also given. All values are in terms of grams of Si and error bars represent the standard deviation of triplicate measurements.....	77
Figure 4.3: DSC scans (of absolute heat flow) of PS- NaClO_4 , NaClO_4 , PS powder, and PS films (10°C/min) (a) 60 and 30 minute PS- NaClO_4 in N_2 , and 60 minute PS- NaClO_4 after the PS had been subjected to heat treatment up to 450°C in N_2 . (b) NaClO_4 and 30 min PS- NaClO_4 , the arrow indicates the endothermic peak of NaClO_4 initiates at the same temperature as the exothermic peak of PS- NaClO_4 . (c) 60 and 30 minute PS powders in air and N_2 (d) 60 and 30 minute PS films on Si substrate in air and nitrogen.	79
Figure 4.4: DSC scans of 30 minute PS- NaClO_4 and NaClO_4 (10°C/min) (a) Increase of SiO_2 oxidation peak with increasing molar ratio of NaClO_4 :Si. Compared to pure NaClO_4 , the decomposition of NaClO_4 in PS occurs slightly below the NaClO_4 melting point rather	

than after the melting point. (b) Enhanced view of the 0.122 molar ratio peak from a) showing the backbond oxidation peak, hydrogen desorption, and Si oxidation.....	81
Figure 4.5: (a) Fourier Transform Infrared Spectroscopy (FTIR) of 30 minute PS. Curve 1 shows the PS after a mild anneal of 250°C in O ₂ for 60s, curve 2 shows the PS-NaClO ₄ after the DSC run, curve 3 shows PS that had NaClO ₄ fill the pores but then was rinsed with MeOH, and curve 4 shows fresh PS. (b) FTIR of fresh 60 minute PS and 60 minute PS after a DSC scan from 30-450°C in N ₂	83
Figure 5.1: SEM, with optical inset, (a) and TEM (b) images of the powder residue from the PS-NaClO ₄ composite.	90
Figure 5.2: TEM images of the powder residue from (a) and (b) PS-NaClO ₄ and (c) a representative SAED pattern.....	91
Figure 5.3: a) TEM of PS powder prior to combustion with SAED pattern inset. b) XRD spectra of PS- NaClO ₄ mixture prior to combustion (top, red) and after combustion (bottom, black).....	92
Figure 5.4: Raman spectra of PS pre- and PS-NaClO ₄ post-combustion.	94
Figure 5.5: High speed video of a PS-NaClO ₄ sample ignited in an acrylic dry box showing the flame from the reaction at 156 μs (a) and 312 μs (b) from the time of the first visible light from the explosion.	95
Figure 6.1: a) An optical image of the microfabricated velocity diagnostic device with integrated Au wire resistors spaced 5mm apart for velocity measurement along the length of the PS-NaClO ₄ composite layer, and b) a close-up optical image of the Au igniter wire.....	100
Figure 6.2: Images in profile of the on-chip velocity diagnostic device a) prior to ignition and b) 61 μs after ignition. The high speed camera captures the nearly 4 cm high flame as it propagates down the length of the device during PS-NaClO ₄ combustion. c) Top-view of a remnant of a single velocity wire after the combustion reaction.	101
Figure 6.3: a) Illustration of the galvanic etching mechanism used for on-chip PS formation. b) SEM cross section of the 20:1 galvanic PS layer bordering the Si ₃ N ₄ mask.....	102
Figure 6.4: Electrical schematic of the on-chip velocity diagnostic device.	104
Figure 6.5: Velocity analysis of the PS-NaClO ₄ reaction (20:1 PS). a) Voltage output from the on-chip velocity test with the dotted lines indicating the time at which the voltage drops. b) Selected frames from high speed video analysis of the reaction (930,000 frames/s) with the image time stamps on the left measured from the time of the sample trigger and the velocity (as measured from the position of the flame at 11.8 μs) on the right.....	106
Figure A.1: 36 mA/cm ² ignition tests. The chip on the left broke in half, the chip on the right did not.	131

Figure A.2: SEM images of PS. A) Cross section near surface of PS, B) full cross-section of PS film, and C) oblique view of the textured surface.	133
Figure A.3: Raman spectroscopy results of PS samples without NaClO ₄ . The solid curves are spectra collected at unique power densities and accumulation times. The dotted curves represent predicted spectra. The vertical bars aid in visualizing the shift of each sample.	136
Figure B.1: Process flow for PS velocity strips	139
Figure B.2: Gas adsorption isotherms for 20:1 and 3:1 PS.....	140
Figure B.3: SEM cross sections of 3:1 PS near the Si ₃ N ₄ etch mask a) and under the igniter wire c). An SEM image of the igniter wire on the PS is shown in b).	141
Figure B.4: Oscilloscope data from 3:1 PS (a) and frames from high speed video (b).	142
Figure B.5: Oscilloscope data from 20:1 PS (a) and frames from high speed video (b).	144

Chapter 1

Introduction of the Thesis

1.1 Introduction

1.1.1 Research Theme and Scope

The scope of this work falls within the realm of materials science: the processing of silicon (Si) by chemical etching gives rise to a unique material structure that when combined with a strong oxidizer under the proper conditions can produce a highly exothermic reaction. Specifically, processing Si with a galvanic corrosion technique to fabricate porous silicon (PS) capable of combustion and explosion with the strong oxidizer, sodium perchlorate (NaClO_4), was examined. Since the processing, properties, structure, and performance of PS for nanoenergetics is a very broad field, this thesis focuses on large surface area ($>\sim 400 \text{ m}^2/\text{g}$) PS that reacts with NaClO_4 to yield a reaction velocity (flame propagation rate) of several kilometers per second. This work seeks to demonstrate a solid state energetic material composed of Si fuel with properties most similar to high explosives such as TNT and RDX and with a faster reaction velocity than current nanoscale thermite materials. A tremendous opportunity for further research into the processing and structure of galvanic PS and into the explosive nature of PS-oxidizer composites exists.

1.1.2 Motivation: Porous Silicon as an Energetic Material

The slow diffusion of oxygen through the native oxide layer renders the oxidation of bulk Si too slow for explosive applications. Porous silicon offers a large surface area to volume ratio typical of nanoscale materials and contains a network of pores that can be filled with oxidizer. When a silicon fuel source is combined with an oxidizer on the nanoscale, kinetic limitations of

silicon oxidation are overcome. Heats of formation indicate that silicon oxidation (SiO_2 formation) is much more exothermic than carbon oxidation (CO_2 formation). Silicon oxidation releases -911 kJ/mol compared to -394 kJ/mol for carbon oxidation, and researchers report an estimated energy yield of 12 kJ/g for PS-oxidizer composites while the traditional explosive material, trinitrotoluene (TNT), only yields 4.2 kJ/g[1].

Advantages of an explosive porous silicon system lie in the ease of incorporation with current electronic and MEMS devices. A bulk Si wafer serves as the substrate and PS is etched monolithically from the wafer. Therefore, fabrication challenges resulting from the need to deposit a film of particles as in thermite materials of metal and metal oxide particles do not arise. Microthrusters, self-destructing chips, and “smart” ignition systems for conventional explosives are potential applications for this explosive system. Additionally, Si is typically considered compatible with biological systems and the explosive system may be compatible with needle-less drug delivery techniques or examining cellular damage resulting from a shockwave.

1.2 Literature Review

1.2.1 Porous Silicon Literature Review

In 1990, Canham discovered porous silicon (PS) displayed room temperature photoluminescence [2]. This finding subsequently led to extensive research into the material resulting in thousands of publications ranging in scope from basic research of the PS structure to microsystem devices incorporating PS. Fortunately, several reviews of PS have been written that serve as compilations of the major findings [3-8]. Basic research studies into the photoluminescence of PS provide evidence of contributions from amorphous Si [9], siloxene [10, 11], and quantum confinement [12, 13]. While it is now generally accepted that quantum size effects are responsible for the light emission from PS, there still exists some debate, and research

into light emission from other Si nanostructures continues with findings indicating a quantum confinement mechanism is indeed present [14]. Applications involving power and energy for PS include gas diffusion [15] and fuel cell membranes [16, 17], sacrificial etch layers [18] (PS is readily dissolved in alkaline solutions of sodium or potassium hydroxide), anode materials for lithium-ion batteries (in powder or thin film form) [19, 20], antireflection coatings for solar cells [21], or even p-n junctions in photovoltaics [22]. Biological and sensor related applications include volatile organic compound microsenors [23], non-toxic, bio-degradable drug release agents [24], and biosensors [25]. As most of the references listed above will indicate, the stability of the surface of PS is the primary challenge to the development of devices that implement PS. From solar cell antireflective layers to sensors, if the highly reactive surface of PS is modified overtime, the performance of the device may change.

Porous silicon formation conventionally requires a custom Teflon etch cell or other material compatible with hydrofluoric acid. Additionally a power supply and noble metal cathode, typically gold or platinum, are necessary. The Si substrate is sandwiched between the top and bottom of the etch cell and connected to the power supply via electrical contact to the backside of the Si. The Si serves as the anode and the noble wire or mesh as the cathode. Figure 1.1 illustrates the conventional electrochemical porous silicon setup.

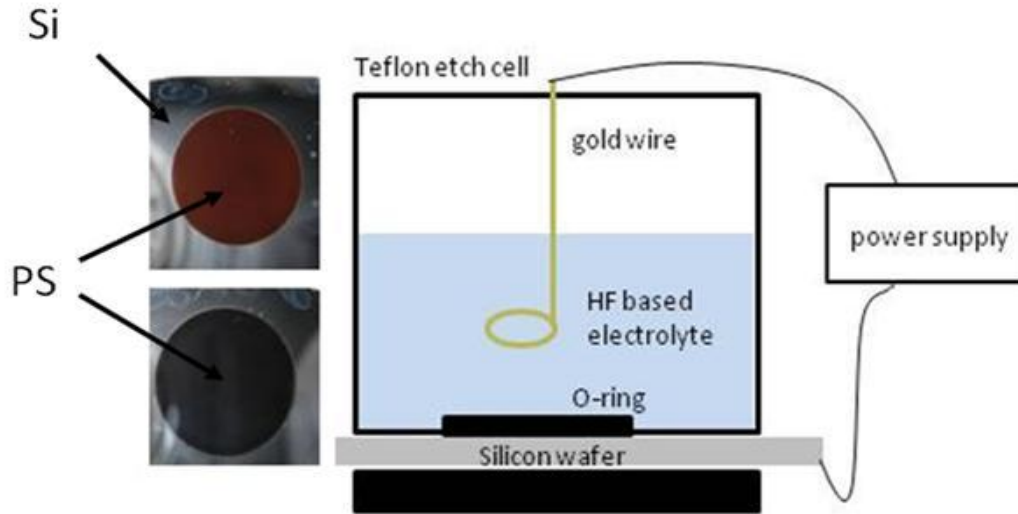


Figure 1.1: Conventional electrochemical setup for PS fabrication with optical images of typical PS shown to the left.

The electrochemical method is desirable because it allows a precise current to be employed for PS formation. However it suffers from the drawback that it is difficult to incorporate with other microsystems batch fabrication since wafers must be individually connected to power supplies. Additionally, the entire backside of the wafer must have a thin film of metal deposited to allow for electrical contact which makes any processing on the backside of the wafer difficult. Other drawbacks include the inability to etch completely through the wafer, for example in a membrane application, (even if a double side etch chamber is used a short circuit will develop [6]) and it is difficult to etch piece parts of a full wafer for research purposes without constructing a custom etch cell for each new geometry.

Methods for PS formation that do not require electrical contact include stain etching and galvanic corrosion. Stain etching of Si occurs by placing a Si wafer in a solution of hydrofluoric acid (HF) and nitric acid (HNO_3), [26, 27] or in place of HNO_3 mild oxidizing salts such as KIO_3 can be used[28]. This technique gives rise to inhomogeneous films that are relatively thin (~ 100 nm) [29]. However, stain etching has the benefit of not requiring electrical contact and Si wafers

of any size or shape can simply be placed in the etching solution to produce PS. Applications of stain etching include antireflection coatings on solar cells[30].

Considering the drawbacks of electrochemical and stain etching to form PS, galvanic corrosion is investigated. In the galvanic corrosion process, a noble metal such as gold or platinum is deposited on the Si surface such that when immersed in an HF-based electrolyte an electrochemical potential forms between the two materials. This potential motivates formation of a galvanic couple [31-35]. Silicon is the more active material in the Si-metal system. Any Si that is electrically connected to metal and exposed to HF serves as the anode, while the metal acts as the cathode. The oxidation of Si in the Au-Si galvanic cell is similar to applying an external bias to Si in HF to generate porous silicon (PS) by promoting holes from the bulk to the silicon-electrolyte interface [36, 34, 37, 32]. Corrosion of the Si surface is realized as either direct dissolution of Si (PS formation) or through the formation of a thick oxide at the surface (electropolishing), depending on the magnitude of the corrosion current [38, 39, 3, 32]. The galvanic cell arrangement is shown in Figure 1.2 with Pt as the cathode in this case. An electric field potential drives cations and anions in solution to migrate to the anode and cathode respectively[40].

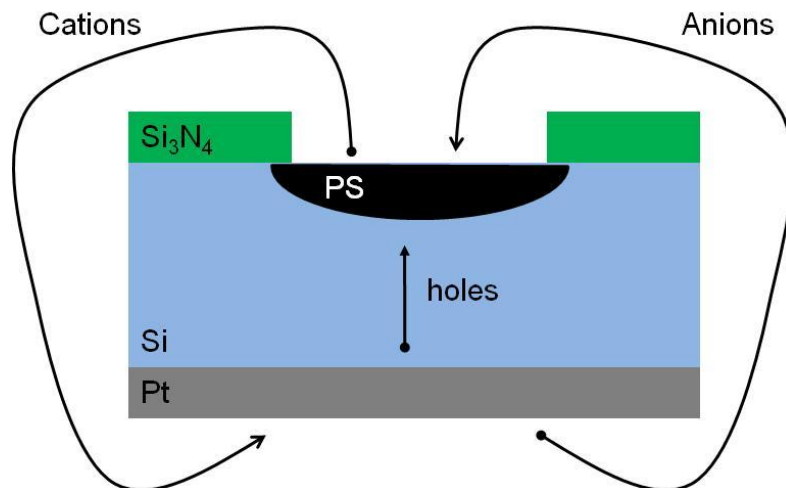
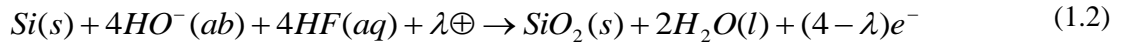
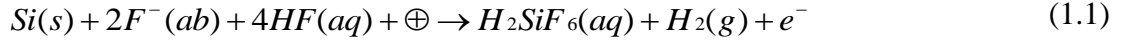


Figure 1.2: Galvanic corrosion mechanism of PS. The noble metal Pt serves as the cathode while Si serves as the anode. A silicon nitride (Si_3N_4) etch mask defines the active area of Si for PS formation.

This method thus allows formation of PS anywhere on the Si wafer where Si is exposed and in electrical contact with the noble metal. Additionally, PS formed with this method has layer thicknesses that can be $> 100 \mu\text{m}$ and has excellent uniformity and morphology that can be controlled by the choice of Si dopant, resistivity, lighting, and electrolyte composition. This method is especially beneficial in generating PS in localized regions on a Si wafer. For example, on a SOI wafer, only regions of Si directly connected to a metal layer will experience PS formation [31].

Porous silicon formation is electrochemical in nature and an excellent review of the models proposed for formation are provided in a book [38] and companion papers by X. G. Zhang [41, 42] as well as a book by V. Lehmann [39]. The complex mechanism of the formation is summarized by Lehmann[39], *“It is surprising that a defect-free, monocrystalline piece of silicon develops sponge-like porous structures....the explanation is a challenge....many models have been discussed...”* A governing principle of the proposed mechanism for PS formation is that an anodic bias is required and PS is formed when the reaction is limited by a charge supply of the

electrode and not by ionic diffusion in the electrolyte. The governing equation for PS formation is given in Equation ((1.1) [39, 43]. Above a certain current threshold which is dependent on the Si dopant type and concentration and electrolyte composition, electropolishing occurs according to Equation (1.2). These equations and the mechanism presented below apply for both electrochemical and galvanic PS.



In these equations, \oplus and e^- represent holes and electrons respectively, (ab) denotes the surface-adsorbed species, (aq) denotes the aqueous species, and (s) is solid species. The net valence of the reaction in Equation (1.1) with the gain of an electron and loss of a hole is thus 2. Figure 1.3 schematically shows the PS formation mechanism[39, 42] in three main steps.

In step 1, the rate limiting step, an anodic bias promotes a hole to the surface of the Si which promotes nucleophilic attack of the Si-H bond by a fluoride ion. In step 2, the Si-F bond makes the remaining Si-H bond vulnerable to nucleophilic attack from a fluoride ion in solution. As a result, a second Si-F bond forms and injects an electron in the Si. With the destruction of one hole and the gain of one electron, the total valence is now 2. In step 3, the Si-F bonds polarize the Si-Si backbonds and render them susceptible to attack from HF or H₂O (not shown). Upon this attack SiF₄ is generated in the gas form and subsequently reacts with two HF to form SiF₆²⁻ which remains in solution (not shown).

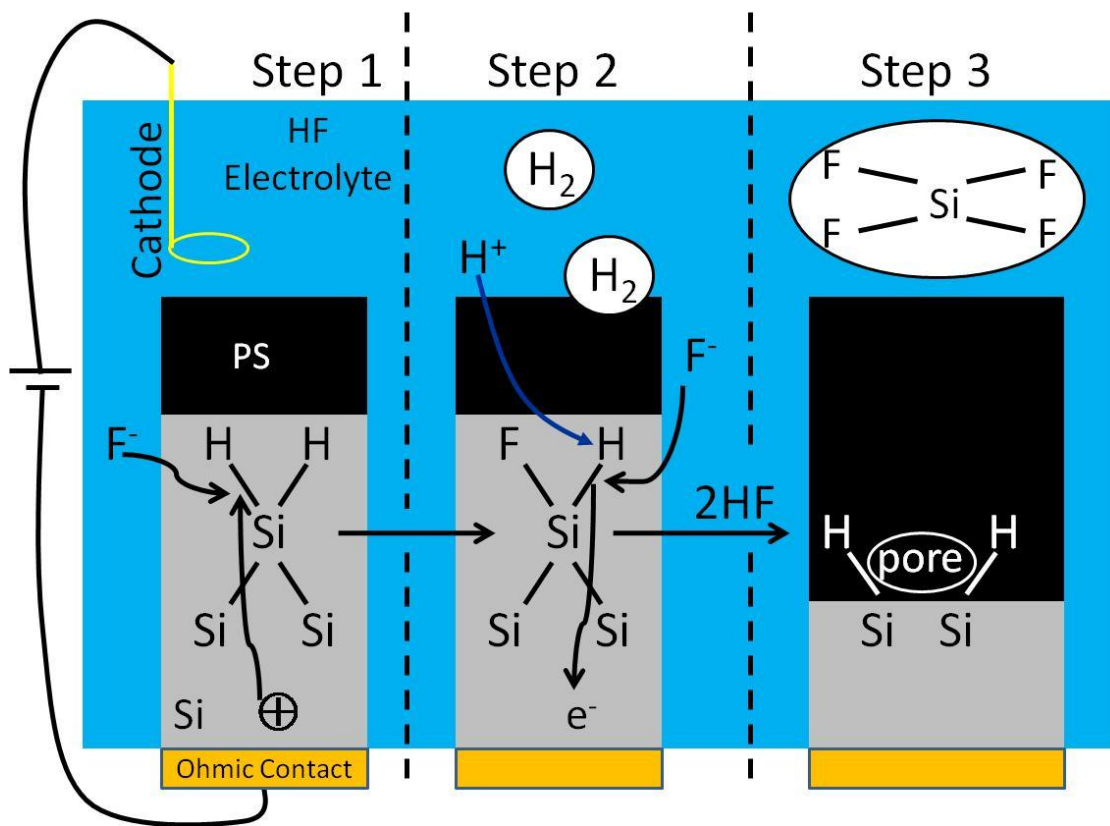


Figure 1.3: The PS formation mechanism. Step 1: An anodic bias promotes a hole to the surface and a nucleophilic attack from one fluoride ion replaces a hydrogen made vulnerable by the hole. Step 2: A second nucleophilic attack from a fluoride ion species on the remaining hydrogen injects an electron. Step 3: The Si-F bonds polarize the Si backbonds which are attacked by H^+ from HF or H_2O .

While out of the scope of this thesis, it is noted that significant research interest of metal-catalyzed dissolution of Si has been conducted recently. This type of nanoscale Si formation is quite similar to the galvanic process in that nanoscale noble metal particles are deposited on the surface of a Si wafer by vapor or liquid phase means and the wafer is subsequently immersed in an HF-based electrolyte. With this process Si wires and pores are formed that may have similar properties to PS and also offer a means of quickly and cheaply fabricating arrays of Si nanowires [44].

1.2.2 Nanoenergetics Literature Review

Nanoenergetics is a relatively new field of study where the large surface area and small dimensions of nanoscale materials are used to produce highly exothermic reactions [45]. These reactions are capable of generating large pressure and propagating at velocities near those of conventional energetic materials [46]. A large segment of nanoenergetic research focuses on nanoscale thermite materials such as aluminum and iron oxide [47], tin oxide [48], copper oxide [46, 49], molybdenum trioxide [50], and bismuth trioxide [51]. These materials all react according to the oxidation-reduction reaction in Equation (1.3) [45] where M and A represent metals or alloys and MO and AO are the corresponding oxides.



Fundamental research into nanoenergetics has focused largely on explaining the rapid energy release compared to bulk thermite materials [52, 53]. Aluminum nanoparticles especially have received a great deal of interest in determining the role of the thin oxide shell in controlling the reaction rate [54-56]. Additional research has investigated whether a shockwave is present in these solid-state energetic materials where the reactants are predicted to also be solid [57, 58]. Applications of nanoenergetics include micro initiators [59], thrusters [60], actuators, and power sources.

Similarly to nanothermite materials, the large surface area and small scale Si domains of PS lead to a material that is much more susceptible to oxidation than bulk Si. It has long been known that Si is a “highly oxidizable material.”[5] Oxidation of Si is of great importance to the integrated circuit community and as such has been studied extensively [61, 62]. These studies however involve bulk Si and the relatively slow growth of oxide layers. Porous silicon oxidation has also been investigated, and in this case techniques such as differential scanning calorimetry

(DSC), thermo gravimetric analysis (TGA), Fourier Transform Infrared Spectroscopy (FT-IR), and x-ray diffraction (XRD) are useful in analyzing the structure and surface termination of PS [63-66].

The above studies focused attention on the stability of PS in air and oxygen environments, but there have been several major breakthroughs in PS nanoenergetic research as shown in Figure 1.4. In 1992, McCord et. al. demonstrated that PS could explode (i.e. a bright flash and loud “bang” were observed) in the presence of the strong oxidizer nitric acid [10]. The result was attributed to the presence of siloxene in the PS structure. However, siloxene is now generally not accepted to reside in the pores of PS. In 2001, researchers discovered that when immersed in liquid O₂ PS exploded with enough power to shatter the Si substrate [1]. The term “explosion” is again used loosely here to mean that the authors observed a bright flash and loud “bang”. Then in 2002 an entirely solid-state Si energetic composite was developed by dropcasting, i.e. filling, the pores with the strong oxidizer gadolinium nitrate [67]. The PS-oxidizer salt composite could be ignited with heat, electric spark, or mechanical friction or impact to realize an explosion-like response. Further oxidizer salts and sulfur were evaluated in 2005 [68]. Finally an on-chip igniter for PS-NaClO₄ composite was developed at the U.S. Army Research Laboratory in 2009 [69]. Except for the 2005 and 2009 reports, the other reports were all accidental discoveries, and as such the evaluation of the reaction was published in high impact journals because it is such an impressive release of energy, but the analysis and characterization was quite limited.



Figure 1.4: Timeline of energetic porous silicon research.

In addition to the above reports, authors have attempted to correlate the PS pore size to the strength of the reaction [70, 71], however only a qualitative description of the reaction is given. Additionally, it has been proposed that the fireball [72] observed between PS and strong oxidizer salts is the result of a ball lightning [73] effect. Again, the report was primarily qualitative in describing the reaction strength.

Aside from sulfur and nitric acid, the investigations into energetic PS composites have all considered strong oxidizer salts. To be compatible with PS, these salts must be readily soluble in an alcohol solution so that the solution can be dropcast into the pores of the PS. The PS surface is organophillic and thus alcohol-based solutions readily penetrate into the PS film. Impregnating the pores with a strong oxidizer is a challenge because the most reactive PS material appears to have pore sizes of ~ 10 nm or less. Therefore, attempting to fill the pores with metal oxide nanoparticles for example is unlikely not only because the pore size is very small, but the pores follow a tortuous path such that nanoparticles cannot simply be dropcast into the film. However, a powder of PS particles, with 4-5 nm pores in individual PS particles, with copper oxide or bismuth oxide nanoparticles, 31 and 38 nm respectively, has been reported to achieve ignition that was qualitatively reported to burn at rates similar to aluminum and iron oxide nanothermite materials [74]. It is assumed that while the metal oxide particles are 6-7 times larger than the pores of the PS powder and are not actually filling the pores, it is likely that

some larger pores may exist on the surface of the particles where a reaction can occur. Regardless, there appears to be promise in using metal oxide materials as an oxygen source for PS combustion if a means of forming a composite can be designed.

1.3 Research Significance

A quick search on ISI Web of Knowledge reveals that since 1963 there have been ~4500 papers published with “porous silicon” in the title. Of those, ~4400 have been published since the discovery of PS photoluminescence in 1992, ~2400 since 2000, and ~1300 since 2005. However, as the literature review sections indicate, there is limited information for PS as a nanoenergetic material and only a few papers present the galvanic corrosion method of PS fabrication. The studies in this thesis focus on both characterizing the etching process and resulting morphology of galvanic porous silicon, in addition to highlighting the benefits of galvanic etching for nanoenergetics. Current literature for galvanic PS primarily focuses on unintentional Si etching during microsystems processing [36, 33, 75]. Of the reports where galvanic etching is used to create PS, the resulting PS films would not be ideal for nanoenergetics as a result of limited thickness and poor mechanical stability. Galvanic PS presented in this work is fabricated specifically for nanoenergetics and is possible to be greater than 150 μm thick and have specific surface area greater than 900 m^2/g . This is also the first report of photoluminescence from galvanic PS, the first microstructure investigation, and first measurement of specific surface areas using gas adsorption techniques.

The research presented on nanoenergetic PS also is meant to highlight the incredible amount of energy that may be stored and released by PS nanoenergetic materials through fundamental characterization. Prior literature has lacked detailed analysis of the PS- NaClO_4 reaction and currently information such as heat of reaction, reaction velocity, and reaction

pressure are unknown. Analysis techniques presented in this work are necessary for an evaluation of the material to determine how processing affects energetic performance. The methods used here are typical for studies of both traditional energetics and nanoenergetics, but for the first time are applied to the study of PS nanoenergetics. This thesis demonstrates how to use these techniques for the thin film PS material. It is revealed that the heat of reaction of PS- NaClO_4 may be as high as ~ 27 kJ/g of PS. Estimates of the fuel to oxidizer ratio are also noted for the first time, and the PS is seen to likely be under-oxidized.

Research here highlights the unique property of PS compared to other powder nanoenergetic materials: it can be monolithically integrated into a Si chip. Specifically, an on-chip velocity measurement technique is realized by using galvanic etching for PS formation. This technique provides complimentary data to high speed video analysis. At 3050 m/s, the velocity of the reaction, as measured by the flame propagation rate across a PS sample, is faster than any other nanoenergetic material to date.

Chapter 2

Modeling Galvanic Corrosion

2.1 Preface

This chapter contains text and figures from a published article by C.R. Becker in the *Journal of Microelectronics and Microengineering* [31]. Permission to reproduce this work in a thesis is granted by the publisher. In this chapter a finite element model is used to model the galvanic corrosion on a Si microsystems device. During the post-processing of silicon (Si) microsystems in hydrofluoric acid (HF) based solutions, a galvanic couple is formed between the Si (anode) and metallic overlayers (cathode), such as gold (Au). Electrochemical etching (corrosion) of the exposed Si results in a porous silicon (PS) film and substantial degradation of mechanical and electrical properties occurs. Focused ion beam milling (FIB) of micro-scale silicon-on-insulator (SOI) devices post-processed using HF solutions is used to determine the depth uniformity of the PS as a function of the geometry of the device. As the dopant concentration of the Si is critical to corrosion, dynamic SIMS is employed to assess the dopant concentration profile in SOI. As a means to model corrosion we present a finite element method (FEM) enabled simulation to model the galvanic corrosion process on Si microsystems exposed to HF. The model uses an analogy to heat transfer to represent electrical conduction and accounts for electrochemical kinetics using the Tafel equation to represent empirical electrochemical measurements of Au and Si in HF. The model reproduces the current limited condition resulting from the finite surface area of metal relative to silicon and predicts the uniform etch rate across the device for surfactant-enhanced HF solutions as seen in FIB. This

work can be extended to applications where forming PS using a galvanic method may be advantageous.

2.2 Introduction

Microelectromechanical[76] systems (MEMS) utilize mechanical and electrical components with a characteristic feature length on the order of micrometers. MEMS may be comprised of multiple material layers including ceramic, semiconductor, and metallic thin films that are patterned photolithographically for electrical, optical, or chemical applications [77, 78]. The small size of microsystem components renders a large surface-to-volume ratio, where surface wetting and electrostatic charge can compromise performance and reliability in product applications, especially when mechanically coupled components or tribological features are utilized [79, 80, 19]. In that regard, damage to MEMS resulting from galvanic corrosion during post-processing has been demonstrated to degrade electrical (resistivity) and mechanical characteristics (including modulus, resonant frequency, strength, and hardness)[81, 82, 33].

During post-processing, micromachined components are often immersed in hydrofluoric acid (HF) to remove sacrificial silicon dioxide (SiO_2) layers to render free standing structures or movable components. In this electrolytic solution, silicon (Si) and metal regions exist at inherently different electrochemical potentials, motivating formation of a galvanic couple[33, 38, 37]. In a galvanic couple current flows in the solution as positive ions from the anode follow a potential gradient to the cathode and negative ions from the metal cathode flow in the opposite direction[40]. In microsystems, gold (Au) is an often used metallic layer. Silicon is the more active material in the Si-Au system. Any Si that is electrically connected to Au and exposed to HF serves as the anode, while Au acts as the cathode. The oxidation of Si in the Au-Si galvanic cell is similar to applying an external bias to Si in HF to generate porous silicon (PS) by

promoting holes from the bulk to the silicon-electrolyte interface [36, 34, 37, 32]. Corrosion of the Si surface is realized as either direct dissolution of Si (PS formation) or through the formation of a thick oxide at the surface (electropolishing), depending on the magnitude of the corrosion current [38, 39, 3, 32]. In this work the magnitude of the corrosion current is well below the electropolishing regime, and Si corrosion is assumed to follow a PS formation mechanism.

The current distribution in a galvanic couple depends on the geometry of the couple, surface area ratio of the cathode to the anode, the solution resistivity, and other resistances to current flow that may exist in the couple[40]. The literature contains several papers on the Si-metal couple in HF that discuss PS formation, but these studies do not address the current distribution across the Si anode[34, 37, 35]. Current density on the Si will diminish with increasing distance from the Au cathode because of the resistance of the HF electrolyte, but no work has studied at what size scale this effect becomes significant. Additionally, work investigating PS formation has been conducted such that a metal cathode is deposited on the backside of a Si wafer causing corrosion to occur uniformly across the exposed front side of the wafer [35]. To our knowledge no studies investigate either the role of geometry in PS formation by Si galvanic corrosion or corrosion uniformity across micrometer scale Si devices.

This work further investigates a study from our group that demonstrates that corrosion in microsystems can be examined with a four-point resistive probe [33]. Figure 2.1 (a) and (b) show optical images of four-point “Van der Pauw” resistive probe structures[83] that are fabricated using the SOIMUMPs[84] technology. The image shows damage to the electrical leads (which appears as a visual discoloration resulting from optical interference effects [85]) owing to galvanic induced PS formation. The device in Figure 2.1 (b) (immersed in a 20:1

(vol:vol) electrolyte of 48% by weight undiluted HF to the nonionic surfactant Triton-X 100 (UDHF:Triton)) shows a uniform discoloration relative to the device in Figure 2.1 (a) (immersed in a 1:1 (vol:vol) electrolyte of UDHF:H₂O). As will be discussed later, an even discoloration indicates uniform PS thickness. The Triton surfactant aids in electrolyte wetting of the Si anode to help yield uniform corrosion. The probe structure is electrically isolated from the Si substrate by a 1 μm thick oxide layer such that corrosion is limited only to the probe structure. Figure 2.1 (c) reveals that corrosion does not occur when Au is not coupled to the Si.

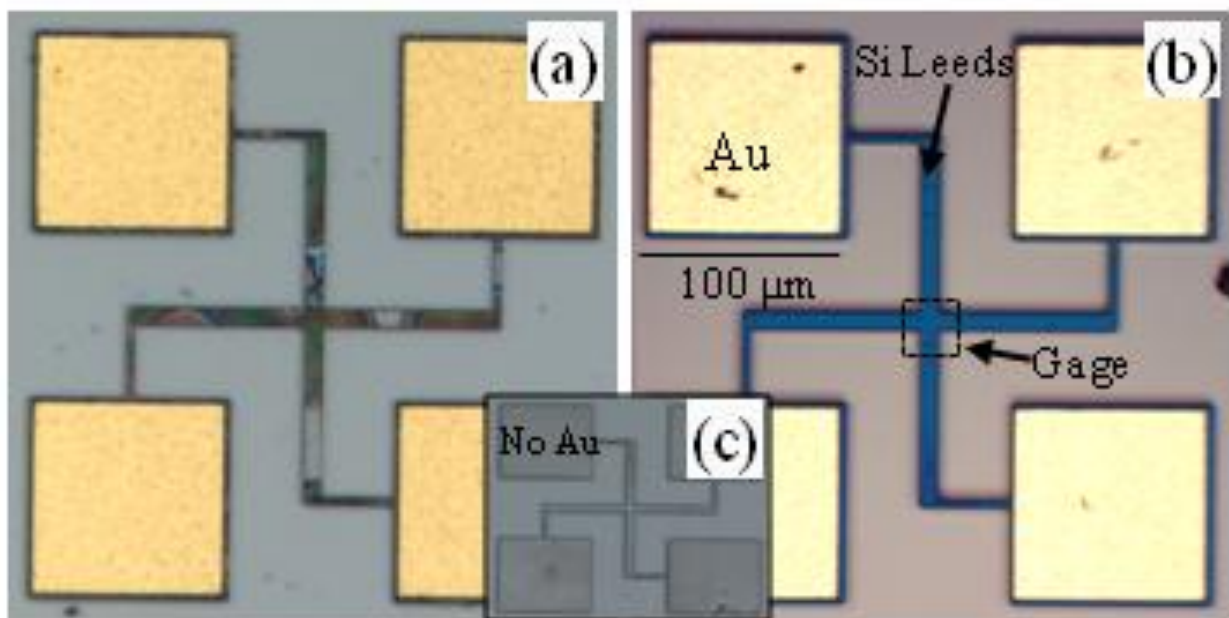


Figure 2.1: Optical image of four-point resistive probe immersed in UDHF:H₂O (1:1) for 24 minutes (a) and UDHF:Triton (20:1) for 12 minutes (b). (c) shows a device without gold after immersion in an HF based electrolyte.

The resistive probe is in the shape of a Greek cross such that a change in resistance of the central gage region occurs as a result of material dissolution. For corrosion studies, the

resistance is monitored (ex-situ) as a function of immersion time in HF solution. Four-point analysis ensures that the measurement applies specifically to the gage region. Since dopant is depleted during PS formation, rendering the corroded PS surface layer nonconductive, resistance increases as the cross section is consumed in HF [33]. As detailed in [33], the change in resistance is correlated to an effective area cross section allowing an etch rate (PS generation rate) to be determined. Using Faraday's law, Equation (2.1), the etch rate is converted to an electrical current density ($C/s \cdot m^2$) [40]. In the equation ρ is the density of Si (g/cm^3), λ is the net valence of the reaction (2 for PS generation and 4 for Si electropolishing[38]), r is the rate of corrosion (m/s), F is Faraday's constant (96,485.338 C/mol), P is the porosity of the remaining surface layer (often 10-50%), estimated by FE-SEM images of the surface of each sample [86, 33], and M_m is the molar mass of Si (g/mol).

$$j = \frac{\rho \lambda r F P}{M_m} \quad (2.1)$$

The resistive probe structures were used to examine current density and etch rate as a function of the surface area ratio (SAR) of Au relative to Si [33]. Specifically, both current density and etch rate increased with SAR, but it was assumed the corrosion was uniform as a function of distance from the cathode. Also, while BEM and FEM have been used to model macro-scale corrosion [87-91], the corrosion of microsystems components has not been modeled using numerical analysis techniques. To this end, the effect of three-dimensional (3-D) geometry, the use of electrically grounded or biased features, doping schemes, and the proximity of the cathode to the anode on corrosion in microsystems remain unexplored. Modeling may therefore provide a fundamental understanding, aiding to either mitigate corrosion damage, or as

a means to target PS growth to regions where researchers desire a PS film as in sacrificial etch layers and fuel cell applications[92, 16].

The goals of this study are to examine the effects of geometry, SAR, and electrolyte composition on corrosion uniformity in microsystems and compare corroded resistive probe devices to the results of FEM analysis. Analytical results as well as BEM simulation [93, 91] from the literature of a simple cube structure are used to first demonstrate proper functionality of the FEM model. To identify the extent of corrosion (by investigating the thickness of the PS layer at the surface as a function of distance from the Au cathode), a focused ion beam (FIB) is used in conjunction with field emission scanning electron microscopy (FE-SEM) to image the cross section of resistive probe structures. Since it is noted that corrosion occurs only on the top surface of the SOI device and dopant concentration of Si is critical to PS formation, a dynamic secondary ion mass spectrometry (SIMS) measurement of the dopant profile of SOI is also made. The corrosion current density recently estimated using the change in resistance of four-point resistive probe structures[33] is then compared to FEM. Lastly, FEM simulations demonstrating the effect of varying size scales and device geometry are presented.

2.3 Experimental

2.3.1 Specimens and Electrochemical Characterization

The electrochemical characterization and dynamic SIMS measurement of n-type SOI was carried out using wafers from SOIMUMPs fabrication run 14 (10 μ m thick Si)[84]. Phosphorous dopant is diffused into the SOI from an overlying phosphosilicate glass layer (PSG) according to a standard manufacturing procedure utilizing a thermal anneal for 1 h at 1050°C to aid its diffusion into the SOI layer. The nominal resistivity of the SOI is estimated to be $4.9 \times 10^{-3} \pm$

$1.0 \times 10^{-4} \text{ } \Omega\text{cm}$ [94]. Electrochemical characterization was performed in a custom electrochemical fixture that accommodates 2 cm X 2 cm Si dice and exposes a 0.982 cm^2 area of SOI to the HF solution. The polarization curves are taken with an Epsilon-E2 potentiostat/galvanostat (Bioanalytical Systems, Inc.). The custom electrochemical fixture consists of the Si working electrode, a platinum mesh counter electrode, and a Cu/CuF reference electrode and is further described in [95, 33, 96]. The Cu/CuF reference electrode is prepared by biasing a copper wire at +1 V relative to a platinum mesh for 5 minutes in UDHF. The Si dice are electrically connected to the fixture using colloidal silver paint.

Potentiodynamic polarization curves were recorded for SOI specimens at a rate of 20 mV/s. This scan rate was chosen such that the thin Si layer would not be completely consumed during the course of the measurement, yet slow enough such that maximum current density was accurately determined. Separate curves were obtained using UDHF, UDHF:H₂O, and UDHF:Triton. Solutions were illuminated during the scans using a tungsten filament at 250 lux. As previously observed [33], the high dopant concentration allows for PS formation on the n-type SOI even in the dark and only a modest difference (5-20%) between potentiodynamic scans under illumination and in the dark is seen. The SOI samples were illuminated here to limit any minor differences in the experiments.

The electrochemical characterization of gold was also performed in UDHF, UDHF:H₂O, and UDHF:Triton. The scans were performed at 1 mV/s, beginning at the open circuit potential (OCP) of Au and carried out just past the OCP of Si in the various etchant chemistries. The solution was stirred during the analysis to promote steady state conditions. The Au working electrode (Bioanalytical Systems, Inc.) has a known diameter and was polished prior to testing in

slurries of diamond and alumina. The system showed a steady OCP for 10 minutes prior to the formal scans.

To obtain direct comparison to the electrochemical characterization, four-point probe structures were fabricated using the SOIMUMPs technology (10 μm thick) in fabrication run 14 [84]. Samples were immersed in UDHF, UDHF:H₂O, and UDHF:Triton and were illuminated as in the potentiodynamic scans. To examine the corrosion on the SOI, subsequent focused ion beam (FIB) milling of corroded specimens was carried out with a NOVA 600i (FEI Co.) dual beam instrument. Prior to etching, platinum was deposited to mask the top surface to prevent re-deposition and maintain image quality. After the mask deposition, a gallium beam was used to rough cut (high current) the section and then smooth the cut (lower current). When viewed in SEM, the distinct interface between PS and bulk Si helps to identify the thickness of the PS. The PS thickness was measured with software that compensated for the tilt of the specimen.

2.4 Numerical Analysis

2.4.1 Fundamental Assumptions

Three-dimensional models of the resistive probe structures were created with a modeling software package (Solidworks, Dassault Systèmes) and then imported for FEM (Abaqus, Dassault Systèmes). The electrical properties of Au and Si are not required for the simulation because the electrolyte acts as the primary charge carrying medium. The conductivity for UDHF and H₂O:UDHF was interpolated from the literature between 0°C and 37.8°C [97, 98], being 0.56 and $0.28 \frac{1}{\Omega\text{cm}}$, respectively. The conductivity of the UDHF:Triton solution is assumed to be the same as the UDHF solution. As a point of reference, in corrosion studies of steel, a 5% NaCl aqueous solution, considered a strong electrolyte, has a conductivity of $0.0795 \frac{1}{\Omega\text{cm}}$ [99]. As

described in following sections, the viscosity and density of the electrolyte are not required, as they are inherent to the empirical polarization curves used to apply the FEM.

FEM of the electrochemical behavior is conducted according to Munn and Devereux [100, 101] , and is similar to the that described by Jia et al. [91]. The procedure for FEM is summarized in Figure 2.2, where Figure 2.2 (c) specifically shows an infinitesimal element of the charge conducting electrolyte. The empirically determined Tafel equations (discussed in section 2.4.2) for Au and Si in HF-based electrolytes serve as boundary conditions for the electrode-electrolyte interface in region b) of Figure 2.2. The OCP of Au and Si serve as the boundary conditions for the cathode and anode respectively and the I_0 and ϕ_0 are defined as 0 mA and 0 V respectively. The complete model of the electrode and electrolyte system in FEM, as shown in Figure 2.2 (a) and (b) consists of three components that are drawn and meshed as individual entities: the anode, the cathode, and the electrolyte. The three are then assembled into one model, where boundaries remain between the components.

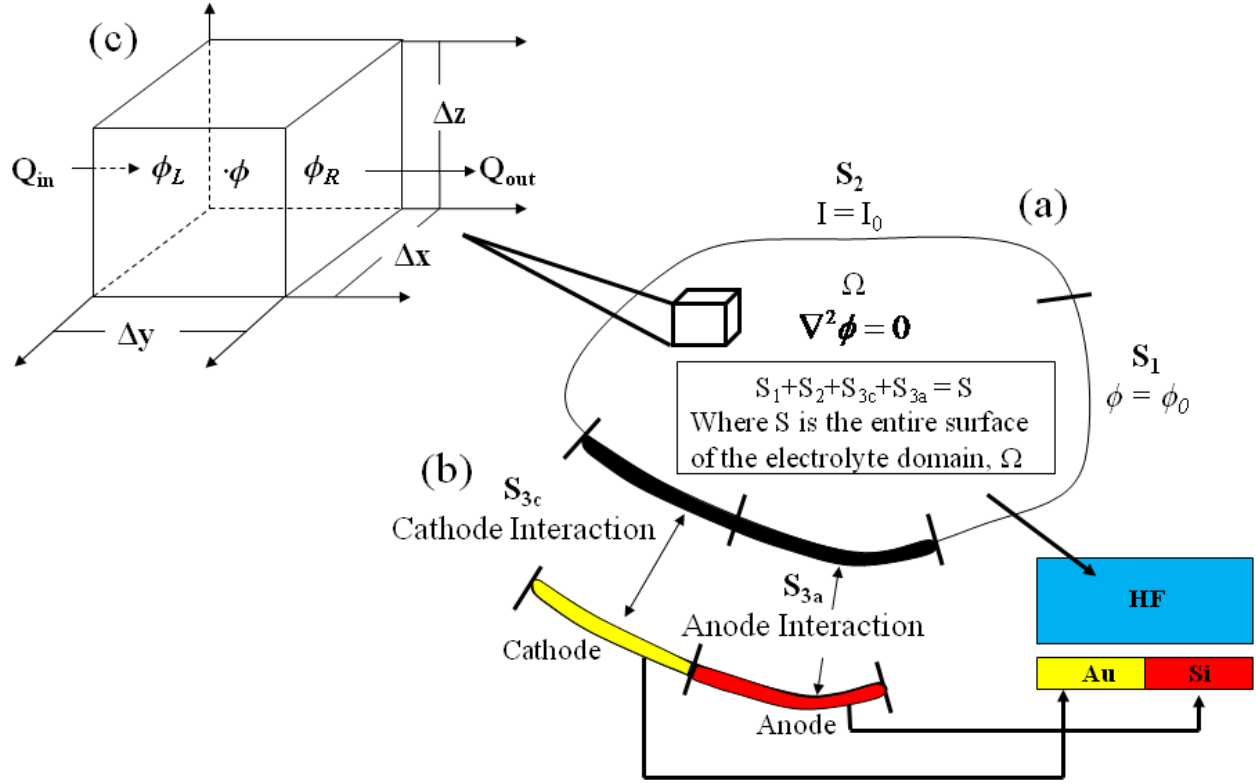


Figure 2.2: Boundary conditions and governing equations for galvanic corrosion. For the system (a), and interface region (b), an infinitesimal element of the electrolyte (c) is used to show charge balance.

The potentials on the left (ϕ_L) and right (ϕ_R) side of the element may be written in terms of ϕ , the potential at the center of the element, equations (2.2) and (2.3).

$$\phi_L = \phi - \frac{1}{2} \frac{\partial \phi}{\partial x} \Delta x \quad (2.2)$$

$$\phi_R = \phi + \frac{1}{2} \frac{\partial \phi}{\partial x} \Delta x \quad (2.3)$$

Charge conduction across the element is analyzed according to Fourier-Ohm conduction. For a conductive medium such as the HF-based electrolytes, equation (2.4) describes the charge

transfer across the boundary of the one-dimensional infinitesimal element, where Q is the transferred charge, σ is the conductivity, A is area, x is the element size, and t is time.

$$Q = -\sigma A \frac{\partial \phi}{\partial x} \Delta t \quad (2.4)$$

For the Fourier-Ohm equation, used to apply a charge balance, the net charge gain for the element, (area of $\Delta y \Delta z$) results in equation (2.5).

$$\begin{aligned} Q &= Q_{in} - Q_{out} \\ &= \sigma \Delta y \Delta z \frac{\partial^2 \phi}{\partial^2 x} \Delta x \Delta t \end{aligned} \quad (2.5)$$

Equation (2.6) presents the net charge gain for a volume element [100]:

$$\begin{aligned} Q &= \sigma \left(\frac{\partial^2 \phi}{\partial^2 x} + \frac{\partial^2 \phi}{\partial^2 y} \right. \\ &\quad \left. + \frac{\partial^2 \phi}{\partial^2 z} \right) \Delta x \Delta y \Delta z \Delta t \end{aligned} \quad (2.6)$$

The potential change accompanying the storage of the charge, Q , is given in equation (2.7), where ρ is the volume mass density and c is the electric capacitance.

$$Q = \frac{1}{\rho c \Delta x \Delta y \Delta z \Delta t} \quad (2.7)$$

The Fourier equation, equation (2.8) results from combining equations (2.6) and (2.7) to eliminate Q as $\Delta t \rightarrow 0$, and by use of the operator notation $\nabla^2 \equiv \partial^2 / \partial x^2 + \partial^2 / \partial y^2 + \partial^2 / \partial z^2$:

$$\frac{\sigma}{\rho c} \nabla^2 \phi = \frac{\partial \phi}{\partial t} \quad (2.8)$$

Finally, for steady state, equation (2.8), simplifies to $\nabla^2 \phi = 0$.

FEM provides the capability to model current flow by invoking an analogy to heat transfer [76]. A subroutine, applied at the electrode-electrolyte interface, allows the current (heat flux) into a body to be specified with an equation that makes use of the difference in voltage (temperature) between the two nearest nodes on opposing surfaces. Table 2.1 identifies the analogy between thermal and electrical units [76, 88].

Table 2.1: Analogy between electrical and thermal units in FEM.

Temperature (K)	→	Electrical Potential (V)
Thermal Conductivity (W/m·K)	→	Electrical Conductivity (S/m)
Thermal Flux (W/m ²)	→	Electrical Current Density (A/m ²)

Steady-state electric fields are governed by the Laplace equation, $\nabla \cdot \sigma \nabla \phi = 0$, where σ is the electrical conductivity, ϕ is the electric potential, and ∇ is the gradient operator [88]. Analogously, temperature fields in steady-state heat conduction are governed by $\nabla \cdot k \nabla T = \dot{q}$, [88] where k is the thermal conductivity, T is the temperature, and \dot{q} is the internal heat generation rate per unit volume. The electric field, $E = -\nabla \phi$, is likewise similar to the temperature gradient ∇T . Furthermore, the current density $J = -\sigma \nabla \phi$ is analogous to the heat flux $-k \nabla T$. In this manner, the FEM model predicts the steady state potential field and current density distribution of the system. As discussed later, steady state for an electrochemical system implies the potential and current fields established at the beginning of immersion in an electrolyte [102].

2.4.2 Accounting for Electrochemical Kinetics

Both electrical and chemical activity occurs at the electrode-electrolyte interface. Typically, there is a discontinuity in the potential field at the interface, referred to as the surface

overpotential, $\Delta\phi = \phi_A - \phi_B$, where the current density required to drive the reaction depends on the overpotential and ϕ_A and ϕ_B are the potentials on either side of the discontinuity[88]. In FEM, points A and B are considered spatially coincident[88].

The boundary conditions for the electrochemical field problem is commonly known as the “*fourth boundary-value problem*”[100], where the relation between current flux through the boundary and the potential on the boundary is non-linear. Specifically, the Tafel equation, equation (2.9), relates the current density to the surface overpotential [103].

$$j = j_o(e^{2.303\Delta\phi/\beta_a} - e^{-2.303\Delta\phi/\beta_c}) \quad (2.9)$$

In equation (2.9), β_a and β_c are the anodic and cathodic transfer coefficients of the reaction occurring at each electrode with units of V per decade of current density, and j_o is the exchange current density with units of mA/cm². Equation (2.9) serves as the boundary condition at the electrode-electrolyte interface. In FEM, this is facilitated through a subroutine that computes the overpotential between a node on the electrolyte surface and a node shared with the surface of the anode or cathode. The subroutine accepts an input of the overpotential between the electrolyte and the anode (or cathode) and computes a current density from the measured polarization data for Si (or Au) in the HF electrolytes.

The incorporation of empirical polarization curves have been treated in varying manners in the literature [100, 101, 91, 104]. For simple systems, some studies rely solely on the Tafel equation, whereas others either import individual data points into a database referenced by the FEM or BEM or use piecewise representations of the polarization curves. Figure 2.3 shows the measured polarization curves from Si and Au in HF based electrolytes, while the inset of Figure

2.3 shows the piece-wise modeled Tafel profiles obtained from the empirical curves.

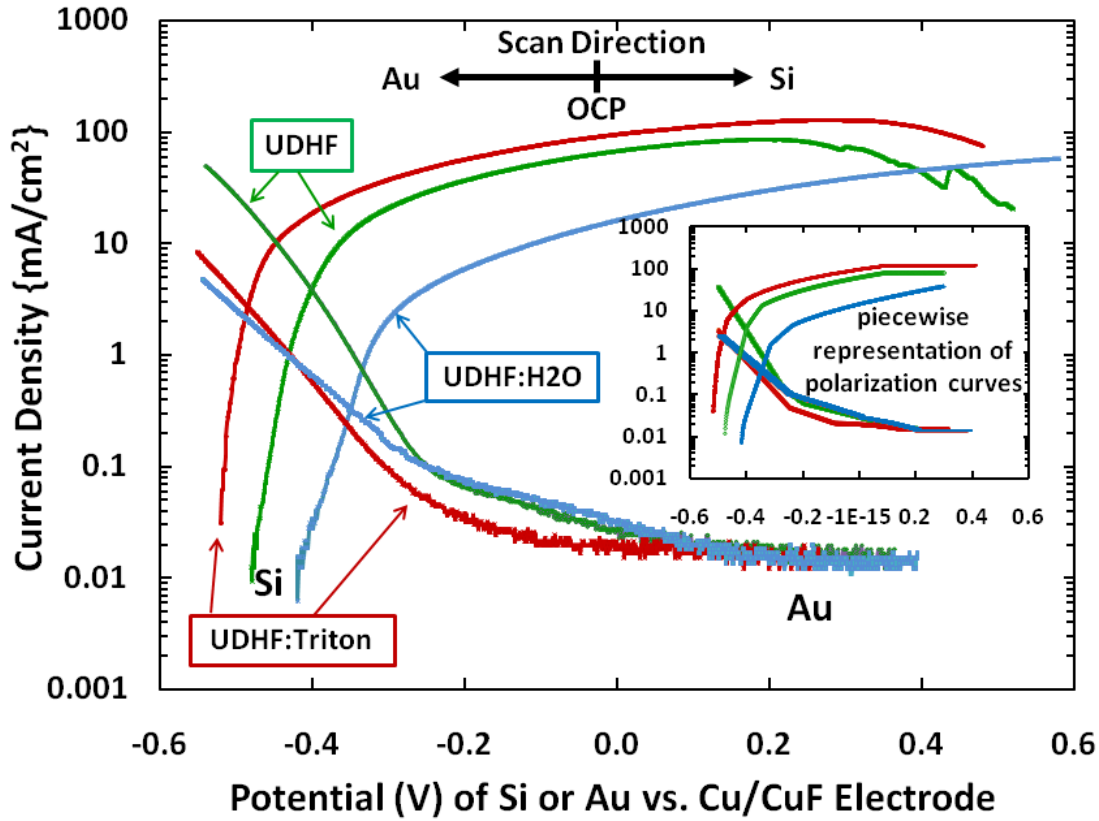


Figure 2.3: Measured Tafel profiles for Si/Au in the three HF electrolytes. The inset shows the profiles as represented using piecewise regions. The arrows at the top of the plot indicate the direction of the voltage scan from the OCP of either Au or Si.

In Figure 2.3, piecewise representations are used because passivation regions exist for both Si and Au and each curve shows deviation from linearity on the log plot. The Tafel equation accounts for the charge transfer activity only and cannot represent passivation, where mass transfer dominates. The curves are therefore divided into several linear regions on the log plot and each region is assigned specific Tafel coefficients. The coefficients in regions several hundred mV above the OCP do not necessarily have physical meaning, but instead provide a simple basis for representing the measured Tafel curves.

Table 2.2 gives the relevant electrochemical parameters for Si at low overpotentials where the Tafel parameters do have physical meaning. Tafel slopes were extracted in the ranges of 0.04-1.00 mA/cm² (13-49 mV above OCP), 0.06-1.03 mA/cm² (35-93 mV above OCP), and 0.09-1.03 mA/cm² (5-22 mV above OCP) for UDHF, UDHF:H₂O, and UDHF:Triton respectively, rendering 26, 46, and 17 mV/dec for UDHF, UDHF:H₂O, and Triton, respectively.

Table 2.2: Key parameters obtained from the potentiodynamic measurement of Si in the three electrolyte solutions.

	UDHF	UDHF:H ₂ O	Triton
β_a (V)	0.028	0.016	0.016
β_c (V)	0.037	0.052	0.015
j_0 (mA/cm ²)	0.028	0.014	0.044
OCP (V)	0.480	0.420	0.520
Mixed Potential (V)	0.395	0.348	0.482
j_0 at Mixed Pair Potential (mA/cm ²)	4.73	0.36	3.17
% Error in j_0 for Fitted vs. Actual Polarization Curves at Mixed Pair Potential			
	9.6 ± 6.7	6.5 ± 4.6	13.0 ± 3.2

The values for Si in UDHF and UDHF:Triton are considerably lower than those typically reported for Si in HF based electrolytes, which is typically near 60 mV/dec[38]. The Tafel slope, however, importantly follows the same trend as surface wetting, in that UDHF:Triton electrolyte has a significantly lower contact angle (better wetting) than UDHF:H₂O [33]. Increasing the surface area of the anode through increased wetting, is known to reduce the Tafel slope, especially in the case of PS formation [38]. Additionally, for a high dopant concentration such as seen in the SOI specimens, the Tafel slope will be lowered from the 60 mV/dec since the surface is at the threshold of degeneracy. Here, charge transfer in the Helmholtz double layer is limiting, the Fermi level lies within the conduction band, and the

materials behave like a metal electrode[38]. In Table 2.2 the current density at the mixed pair potential is shown to be quite similar for UDHF and UDHF:Triton, but an order of magnitude lower for UDHF:H₂O. This decrease in UDHF:H₂O current density is explained by sessile drop characterization in [33] that reveals UDHF:H₂O has poor surface wetting, reducing the flux of reactants to the Si surface.

The potentiodynamic scans of Au in the HF electrolytes reveal a mass transport limited region followed by a charge transfer controlled region beginning at approximately 238 mV above the resting potential for UDHF:H₂O (217 mV above the resting potential for UDHF). In the charge transfer region, the Tafel slope is 478 mV/dec and 541 mV/dec for UDHF and UDHF:H₂O respectively. Au in UDHF:Triton lacks the charge transfer region shown by the other two HF solutions. Comparison across the full scan ranges of the representative and empirical potentiodynamic profile identifies variation of current density of $7 \pm 5\%$ and $15 \pm 8\%$, for Au and Si respectively for UDHF; $4 \pm 2\%$ and $9 \pm 4\%$, respectively for UDHF: H₂O; and $11 \pm 10\%$ and $5 \pm 3\%$, respectively for UDHF:Triton.

2.4.3 Validation of the Finite Element Method

To verify appropriate interaction for the electrode-electrolyte system in the FEM software, the FEM solution was compared against a more basic geometry solved using the finite difference method (FDM) [93] and the BEM (BEASY, BEASY Software) [91]. The anode and cathode are represented as two separate cubes of width 1cm and the electrolyte is modeled as a cube of varying height (simulating varying the depth of electrolyte surrounding the immersed anode and cathode) with conductivity of $1 \frac{1}{\Omega cm}$. The electrical potential of the anode is set to -0.5 V and that of the cathode is +0.5 V. In the Tafel equation, $\beta_a = \beta_c = -0.05$ V and $j_0 = 0.1$ mA/cm² [91].

The potential distribution at the electrode-electrolyte interface ($z = 0$) as a function of location and for three different electrolyte depths is shown in Figure 2.4 for the FEM. The results compare favorably to those in [93] (not shown in figure) where the electrolyte heights of 1 and 10 cm are nearly collinear, and for the depth of 0.1 cm, the potential at the interface more closely approaches the OCP of the anode or cathode.

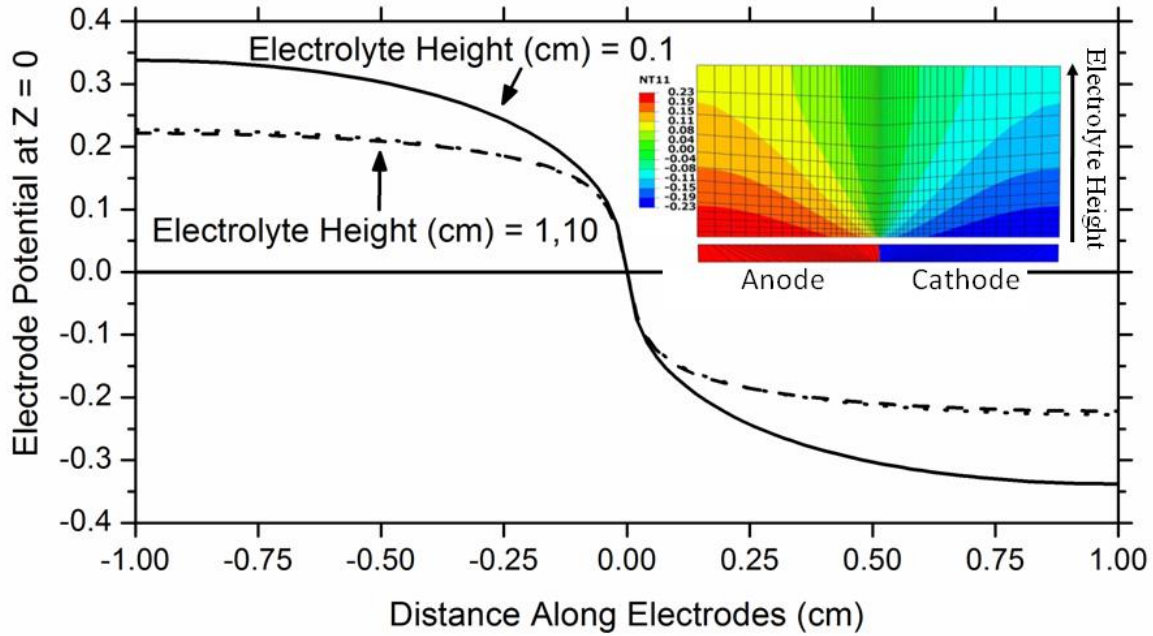


Figure 2.4: Validation of FEM model for a simple geometry: The potential profiles for the electrolyte along the surface of the anode and cathode for three different electrolyte depths. The electric field potential distribution (and mesh) is shown in the inset.

The results in Figure 2.4 therefore give insight into the effect of electrolyte depth (the height of electrolyte in the FEM model) on potential and current density, which can only be evaluated numerically [93, 91]. As the depth is decreased, the isopotential field lines become normal to the electrode surface. As the depth is increased, the field lines become more parallel to the electrode surface[93]. The field distribution depicted in Figure 2.4 importantly identifies that to accurately model an electrochemical interaction in which the electrolyte depth is nearly infinite with respect to the dimensions of an immersed electrode, the electrolyte needs to have a depth (height) similar

to width of the electrodes. If the electrolyte is too shallow, the potential at the electrode-electrolyte interface will approach the OCP of the electrodes and the overpotential and current density will be reduced.

2.5 Results and Discussion

2.5.1 Examination of Uniformity of Corrosion Using Focused Ion Beam

Ex-situ monitoring of the change in resistance of the four-point probe structures gives insight into the corrosion only at the gage region of the device. Therefore, in an effort to understand the uniformity of the Si corrosion across a micrometer scale device, FIB milling of four-point probe structures is conducted. Figure 2.5 shows SEM images, obtained after FIB milling, of a four-point probe structure that had previously been immersed for 24 minutes in UDHF:H₂O. Figure 2.5 (a) identifies where the FIB cuts were made, and the Pt, PS, and Si layers are labelled in Figure 2.5 (c)-(e) according to their contrast in the image. The structure was cut immediately adjacent to the Au layer in Figure 2.5 (d) where the PS region (the region is known to most likely be PS as TEM cross sections show in [86]) was 733 nm thick and below this region is a 100 nm separation from the uncorroded Si. In the regions where cross sections are imaged, the separation appears near the Au layer, but is not observed in the gage section. A separate cut was also made in the gage section, Figure 2.5 (e), revealing a 508 nm thick region of PS. Figure 2.5 (b) shows the detail near the Au layer. Here, a trench several hundred nanometers wide is observed around the periphery of the Au.

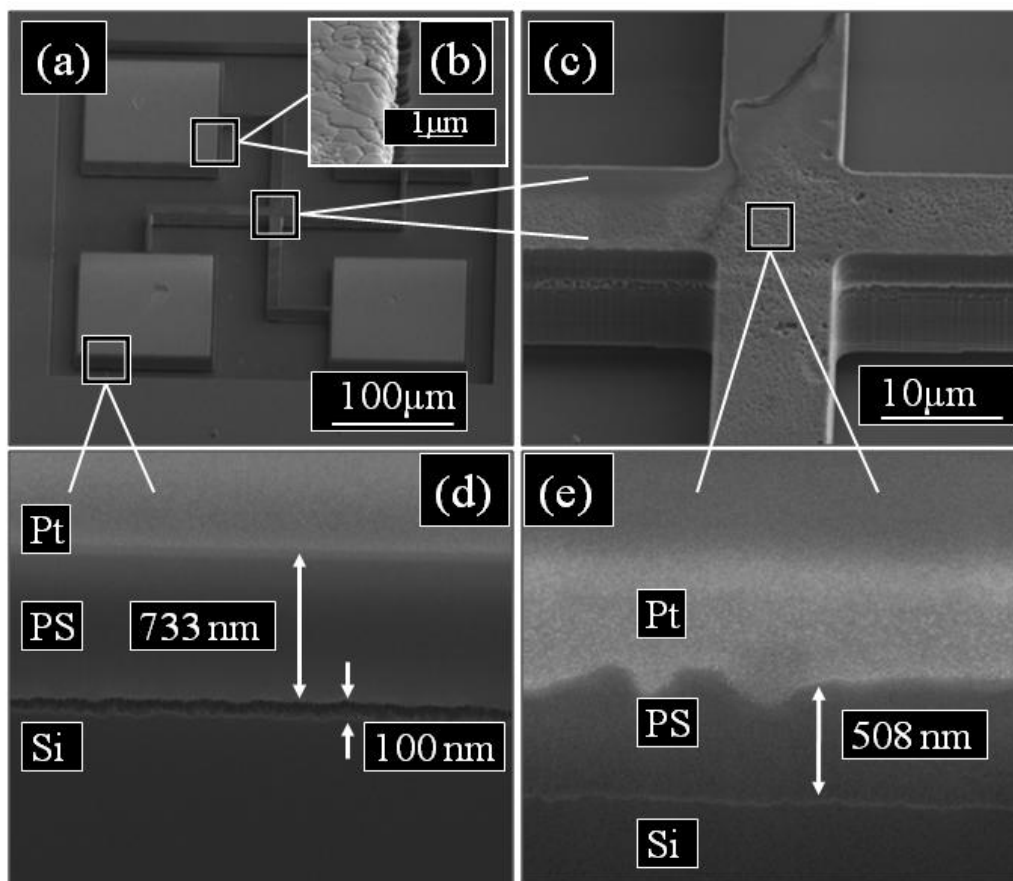


Figure 2.5: Four-point probe structure after 24 minutes of immersion in (UDHF:H₂O), including: (a) entire structure (oriented as in Fig. 1 (a)), (b) shows the Au-Si interface (c) the gage section of the device - revealing “macroscopic” pitting and pores, (d) the cross section of the region near the gold, and (e) cross section of the gage region.

Figure 2.6 shows SEM images of a four-point probe structure that has been immersed for 12 minutes in UDHF:Triton. As in Figure 2.5, the probe has been cross sectioned in three regions to quantify the thickness of the PS. In this case the PS has a nearly uniform thickness across the device, *i.e.* 211, 233, and 242 nm in the lead, near the Au, and gage, respectively. The small fluctuations in PS thickness are probably a result of localized wetting problems. Considering the gage section (furthest from the cathode) shows the thickest PS layer, it can be assumed that on this size scale and for the relatively small current densities, the distance of the

anode from the cathode has a negligible effect on current density. A trench (not shown) similar to that in Figure 2.5 is, however, seen at the top of the Si, along the perimeter of the Au pad.

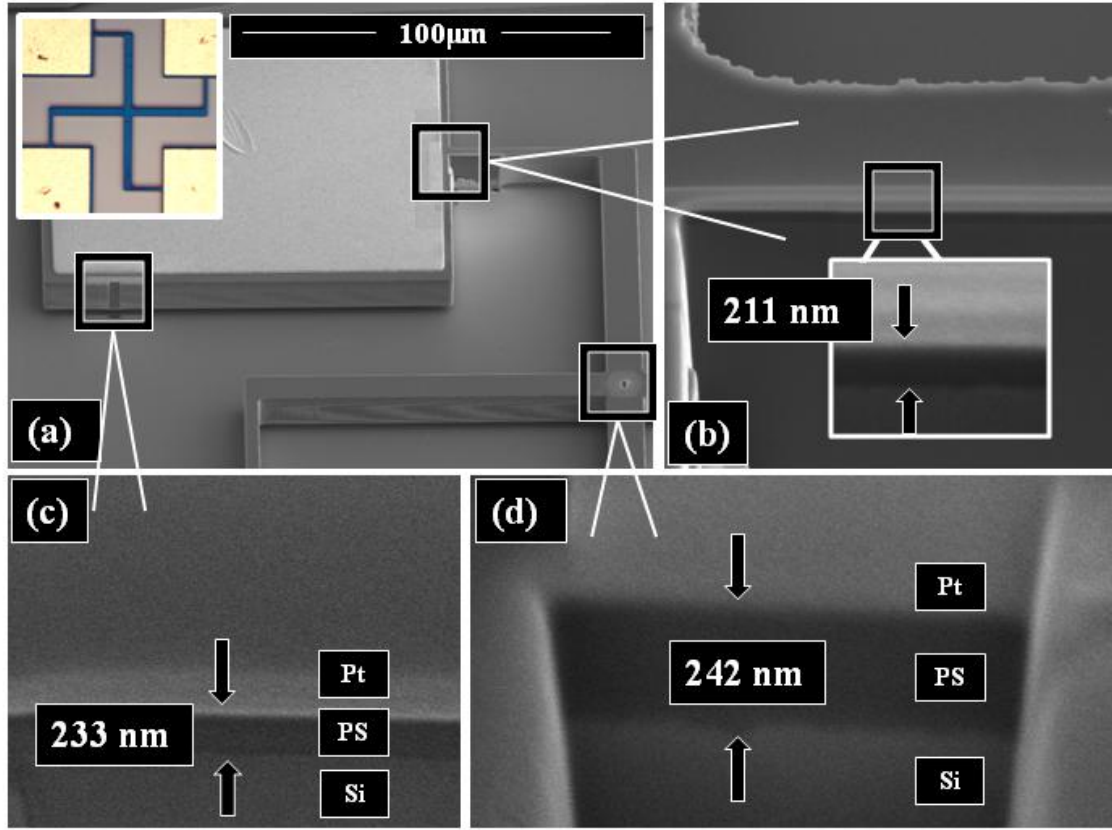


Figure 2.6: Four-point probe structure after 12 minutes of immersion in UDHF:Triton (Figure 2.1 (b)). The cuts reveal a nearly uniform PS thickness across the device contrary to the UDHF:H₂O device. (b) is a cross section on the Si lead near the gold cathode that shows a uniform PS depth across the entire cut, (c) is a cut near the Au cathode, and (d) is a cut in the gage section.

The FIB cross sections importantly reveal that galvanic corrosion of Si microsystems structures is uniform across the device provided the HF electrolyte wets the Si surface (as in UDHF:Triton), but varies significantly if the electrolyte exhibits poor wetting characteristics (as in UDHF:H₂O). A cross-sectional trench along the entire length of one lead of the UDHF:H₂O device, was made to specifically investigate the uniformity of the corrosion in areas of visual

discoloration, Figure 2.7. In the figure, large pits are seen at either end of the leed whereas the middle region is relatively smooth. The thickness of the corroded layer varies by a factor of 6 (from 142 nm in the center to 852 nm near the Au) as indicated in the figure. In the corner of the leed in Figure 2.7, localized separation, as in Figure 2.5, between the PS and underlying Si is observed along the leed.

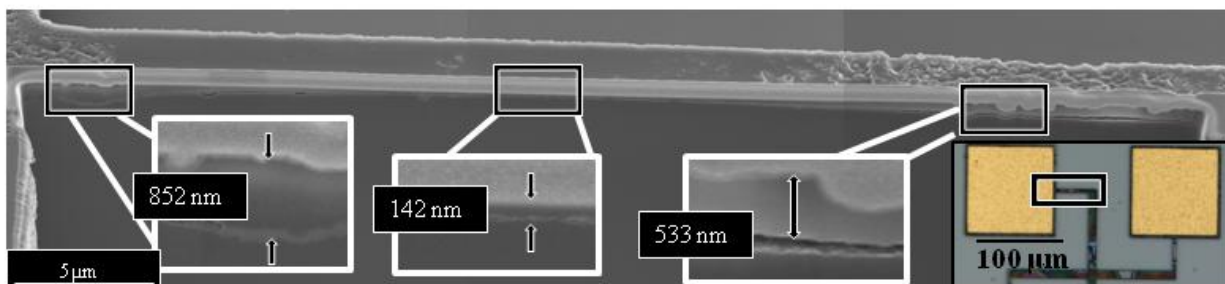


Figure 2.7: Thickness variation along a specific leed of the UDHF:H₂O resistive probe structure examined using FIB milling, shown relative to visual appearance at the same location. The micrograph insets identify the PS thickness along the arm. The optical inset identifies where the cut was made on the leed. Three separate SEM images were spliced to show the full length of the leed.

The variation in thickness of the corroded surface layer along the leed structure could be attributed to a combination of current density gradient along the beam (although this is found to be unlikely in FEM analysis discussed in section 2.5.2) and poor surface wetting of the UDHF:H₂O electrolyte (identified in the previous study [33]). Visually, the coloration of the Si surface is observed to vary on the resistive probe as seen in Figure 2.1 (online color version). The UDHF:Triton corroded device in Figure 2.1 on the other hand displays a uniform blue color consistent with a constant etch depth across the device. The local separation of the PS from the substrate is most likely attributed to damage from the FIB milling. Electropolishing is not thought to play a role in the separation because the measured corrosion current densities are well below this regime.

2.5.2 Examination of Electrochemical Phenomena Using Finite Element Method and Comparison to Focused Ion Beam Results

It was determined using transmission electron microscopy (TEM) that only the top surface of the SOI resistive probe structures corrodes[33]. The sides and bottom of the leads do not corrode, despite being exposed to the electrolyte. This likely owes to the variation in dopant concentration through the thickness of the Si. Figure 2.8 shows a dynamic secondary ion mass spectrometry (SIMS) measurement of phosphorous (^{31}P) dopant in an uncorroded SOI layer. Figure 2.8 also includes a measurement of Si (^{28}Si) through the thickness to ensure the oxide layer beneath the Si was not reached.

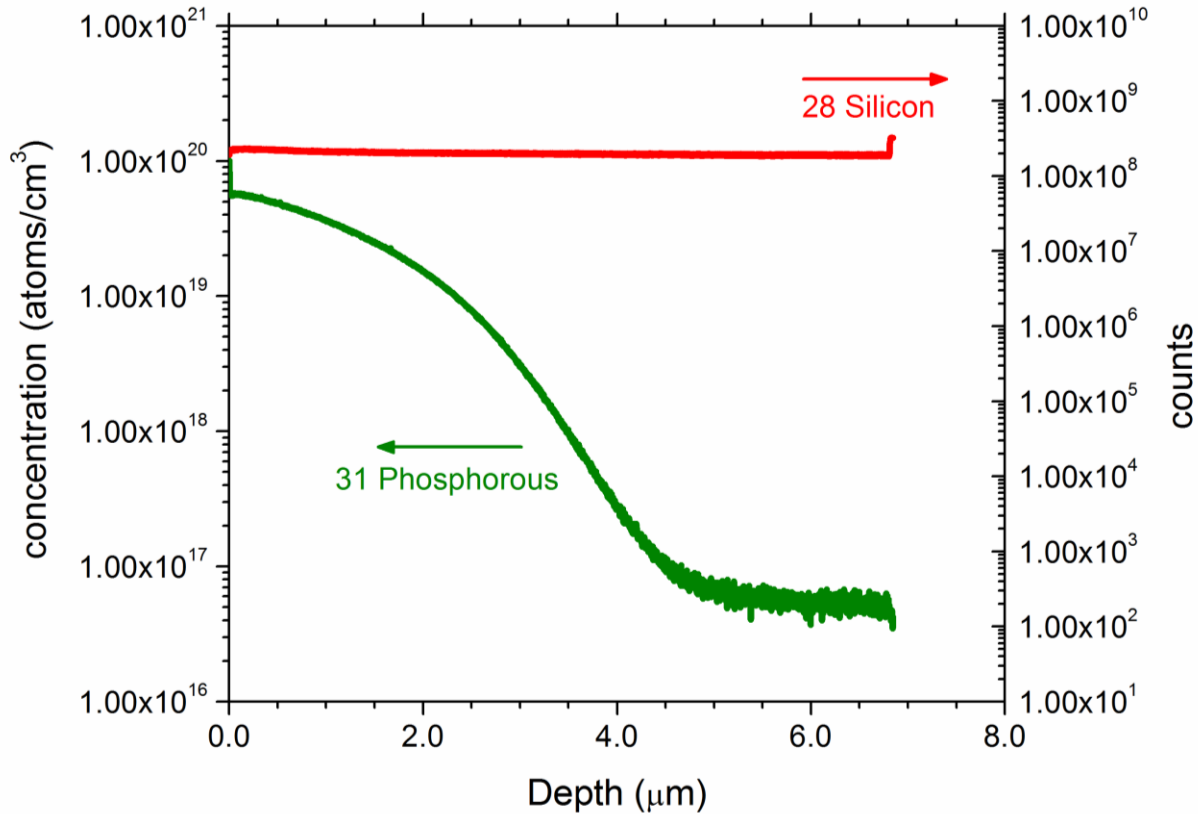


Figure 2.8: Dynamic SIMS measurement of phosphorous (^{31}P) in a pristine SOI sample from SOIMUMPS fabrication run 14.

The dramatic decrease of dopant through the thickness indicates that corrosion would be limited to the top surface of the device where the highest concentration of holes are available for PS formation [3]. Therefore, to address the issue of surface-specific corrosion, the FEM model was constructed to represent the condition where only the top surface of the Si was allowed to interact with the electrolyte through the FEM subroutine. In other words, the full 3-D probe structure is modeled, but the subroutine is only called at the top surface of the probe.

The SIMS data reveals that dopant concentration is roughly uniform in the first micron of the SOI, which is a thicker region than corrodes on the resistive probe structures, as Figure 2.5-Figure 2.7 show. With a nearly uniform dopant concentration through the first micron of SOI, the PS morphology (*i.e.* the porosity and pore size) are expected to be constant through the PS thickness. Also, as the potentiodynamic scans were performed fast enough to consume less than 100 nm of SOI in the regime from OCP to the mixed pair voltage, these scans provide accurate data for FEM boundary conditions.

Experimental results from the resistive probe structures reveal a cathode limited condition for the corrosion current, *i.e.* corrosion is limited by the available area of Au and is constrained to the PS formation regime and not the electropolishing regime[33]. In [33], the current density increased with the surface area of Au (for the same underlying Si structure). FEM also predicts this trend and is in reasonable agreement with the best values that can be obtained with the methods used in [33]. Figure 2.9 shows the current density predicted by FEM as well as the experimentally obtained maximum current densities for the actual and nominal SAR on the SOI probe structures. The nominal SAR (0.85) of the probe accounts for all exposed Si regions on the device whereas the actual SAR (~4.52) accounts for only the top surfaces of the Si since those are the surfaces observed to corrode[86]. The experimentally (ex-situ)

obtained maximum current is measured by investigating the change in resistance of the device after a 3 minute immersion in an HF electrolyte. The 3 minute immersion time is long enough to produce a PS layer thick enough to reveal a resistance change while being brief enough to nearly capture the maximum etch rate and corrosion current density. Therefore discrepancy between the experimental maximum current density and the modeled maximum current density primarily stems from the inability to accurately experimentally measure the initial steady-state current formed across the Si device. In practice, the current is transient such that immediately following immersion the current is greatest but falls off rapidly as shown in [33]. This drop in current may be the result of loss of connectivity of the Au cathode with the Si device as HF attacks the Cr adhesion layer, or as a result of the gradient in phosphorous doping through the device.

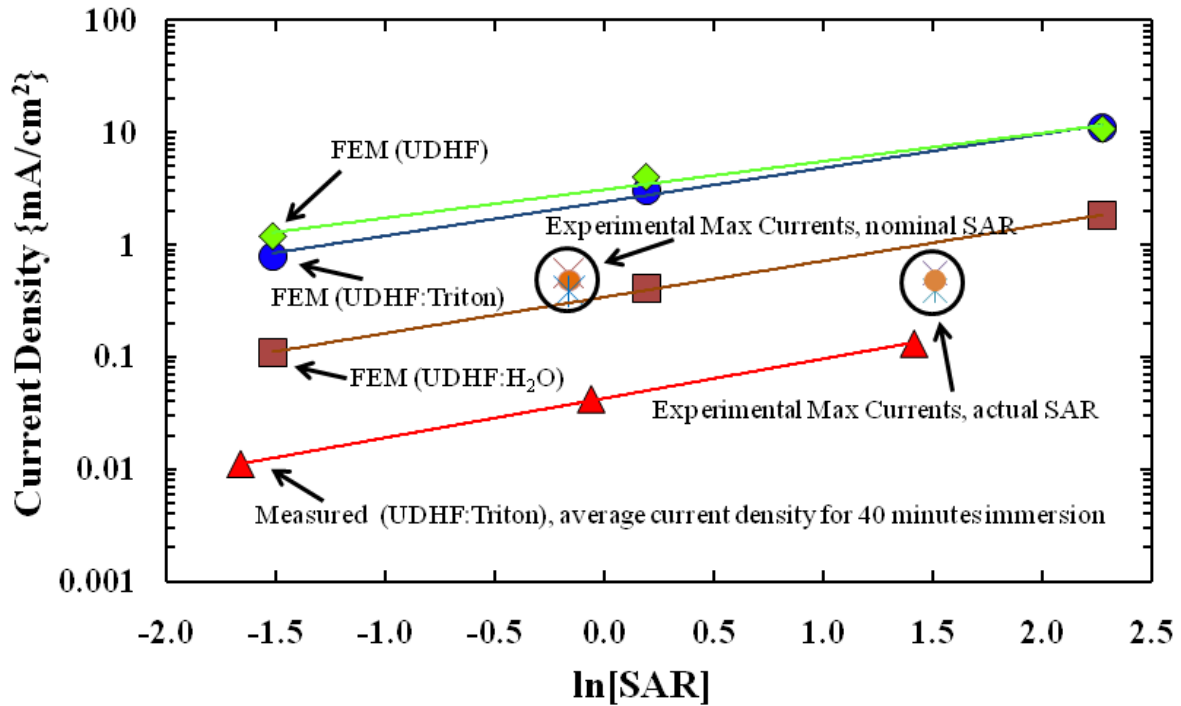


Figure 2.9: Empirical (resistive probe) and analytic (FEM) data for current density vs. SAR for resistive probe structures, where corrosion is limited to the top Si surface.

While data at unique SARs for maximum current densities were not taken, data are plotted in Figure 2.9 that represent the average current density for a 40 minute immersion in UDHF:Triton. The average current density (measured ex-situ from the change in resistance of the device) for this relatively long immersion time is much lower than the maximum current density seen for the brief 3 minute immersion, but the trend in current density versus SAR is expected to hold regardless of immersion time. The least squares fits, provided in the figure for each data set, are essentially parallel in all cases indicating the correct representation of current limited condition for corrosion. In contrast to the measured average current density, the FEM results in Figure 2.9 represent the maximum possible corrosion current (steady state) occurring as the result of the mixed pair potential of the Au-Si couple. To explain, the FEM results predict the theoretical maximum corrosion current and are not affected by other factors such as mass transport through the PS layer formed at the surface or as a result of the increased resistivity arising from the phosphorous dopant gradient [102]. Additionally, illumination of the Si device will play a larger role in the current density as the dopant concentration decreases as only highly doped n-type Si forms PS at a rate independent of illumination. Furthermore, the current density values corresponding to the nominal 0.85 SAR align much closer to the model and indicate that while corrosion occurs only on the top surface (with some stray etching on the sidewalls), the entire exposed area of Si should be included when modeling Si corrosion. In other words, if the model is designed so that only the top surface of the SOI is expected to corrode, then results from the model will align closely with the nominal SAR of a device. This indicates that while only the top surface of the Si corrodes, the remaining surfaces of Si are acting to reduce the SAR and thus lower the current density.

While some limitations do exist in trying to model the current density, FEM is able to nearly reproduce the experimental results. The maximum corrosion current density predicted by FEM for a device of 0.85 SAR in UDHF is 1.400 mA/cm^2 (UDHF) whereas the measured resistive probe shows a maximum current density of 0.550 mA/cm^2 . For UDHF:Triton, the model predicts 2.147 mA/cm^2 whereas the measured maximum current density for this electrolyte is 0.479 mA/cm^2 . The largest measured resistance in UDHF:H₂O implies a maximum current density of 0.387 mA/cm^2 , which is very close to the FEM prediction of 0.302 mA/cm^2 for the UDHF:H₂O electrolyte. This study suggests that during the corrosion of resistive probe structures, the maximum corrosion current density may be up to 4 times larger than experimentally measured. The experimental results are limited however in that the measurement of the current across the device immediately following immersion is difficult since the PS layer will be very thin and difficult to measure by FIB/SEM or by resistance based measurements. To this end, it is highly likely that the initial current density across the device is very near the predictions of the model.

As for the corrosion uniformity across the device, it is clear that FEM performs well in modeling the nearly uniform corrosion current density across the microsystems device immersed in UDHF:Triton. As shown in Figure 2.10(d), FEM predicts a current density gradient of only a few hundredths of mA/cm^2 along the Si leads. On the other hand, the UDHF:H₂O etchant resulted in varied visual coloration and a corroded surface layer that is nonuniform in thickness. These results are consistent with Si surface wetting by the UDHF:Triton electrolyte relative to the other two electrolyte compositions [33]. Enhanced wetting allows the exposed Si and Au surfaces to participate in the corrosion process, whereas the UDHF:H₂O electrolyte, demonstrates poor wetting that effectively increases the resistance in the electrolyte to the point

that uniform corrosion does not occur. Furthermore, electrical- and mass-transport to the Si could be blocked by hydrogen bubbles adhered to the surface[39]. These phenomena would not be considered in the FEM model. It should also be noted that since the model predicts a uniform current density, the trench seen in Figure 2.5 most likely stems from metal-catalyzed dissolution on the Au-Si interface[105], induced by the intermediate Cr adhesive layer. The trench represents bulk material removal, which would not be consistent with PS formation mechanisms; and while electropolishing is a possibility, it is found unlikely since the galvanic couple current density is too low for this effect.

It is known that the choice of oxidizing agent and the choice of metal cathode also influence the corrosion current[32]. Stronger oxidizing agents or higher concentrations of oxidizing agent will generally increase the limiting current of the galvanic cell. Oxygen, thought to be the active oxidizing agent here, will be reduced at the gold cathode according to equation (2.10).



In this work, the concentration of dissolved oxygen in the aqueous solutions is expected to be similar among all three electrolyte solutions and the cathodic reaction will be the same regardless of electrolyte composition. Additionally, the UDHF:Triton will enhance surface wetting to promote the cathodic and anodic reactions, further increasing the limiting current.

Since corrosion uniformity may be of interest to microsystems engineers hoping to employ selective PS galvanic formation, we show in Figure 2.10 the effect of device size on corrosion current uniformity. Figure 2.10 (a) shows a device with gold pad dimensions on the order of a meter, (b) shows a device with dimensions on the order of 10 cm, (c) shows a device with dimensions on the order of 1 mm, and (d) shows the actual device dimensions on the order

of 100 μm . It is clear that as the device dimensions increase, the current density becomes non-uniform. This is the result of the increased resistance in the electrolyte as the distance from the anode to the cathode increases[40]. While a 1 m device greatly exaggerates the effect, Figure 2.10 shows that as dimensions approach 1 cm, a gradient in current density is realized. Additionally, if another material system such as platinum-Si is used, which is known to produce higher currents than the Au-Si couple[35], a large gradient will result. Figure 2.10 illustrates the importance of using FEM to model the corrosion. Numerical simulations are necessary to predict the magnitude of current density across a device (or a particular geometry).

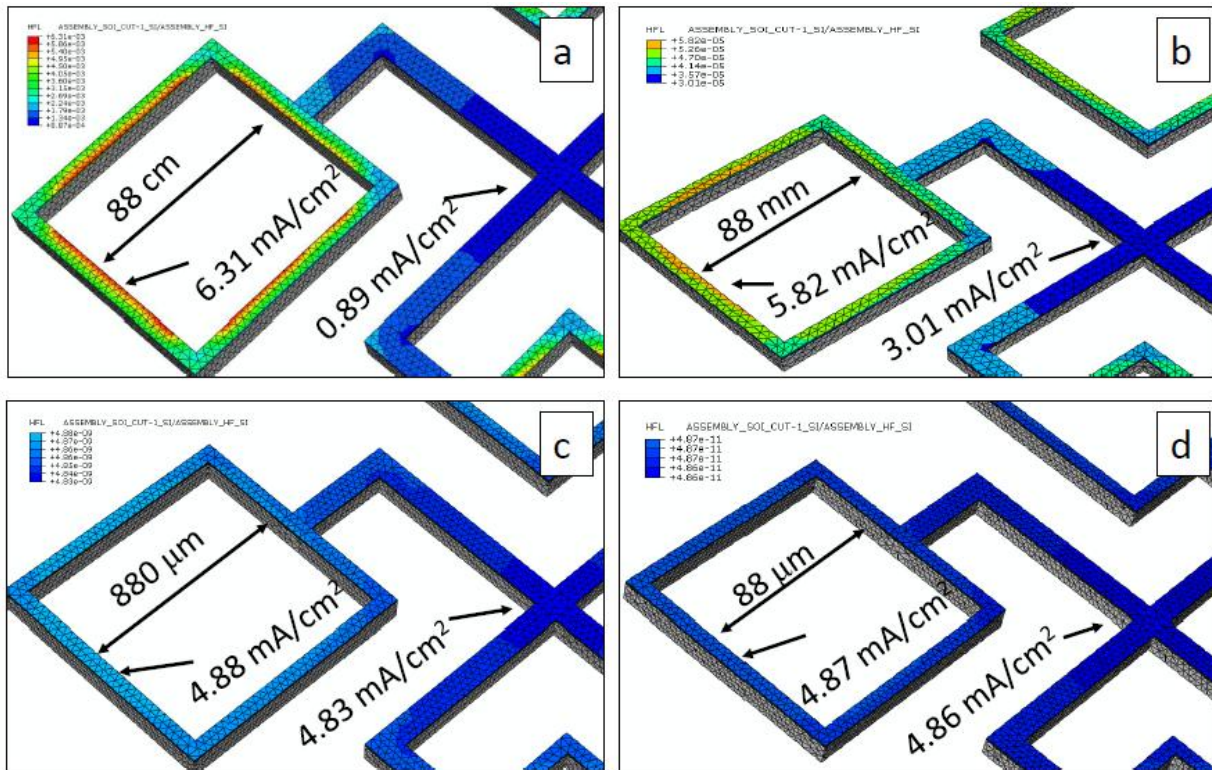


Figure 2.10: FEM results from a four-point probe model in UDHf:Triton showing the effect of device size on corrosion current density. (a) shows a device with gold pad dimensions on the order of a meter, (b) shows a device with dimensions on the order of 10 cm, (c) shows a device with dimensions on the order of 1 mm, and (d) shows the actual device dimensions on the order of 100 μm .

In Figure 2.11, FEM models of simple square geometry (similar to the model in Figure 2.4) with varying SAR are used to investigate the possible effects of geometry on galvanic corrosion.

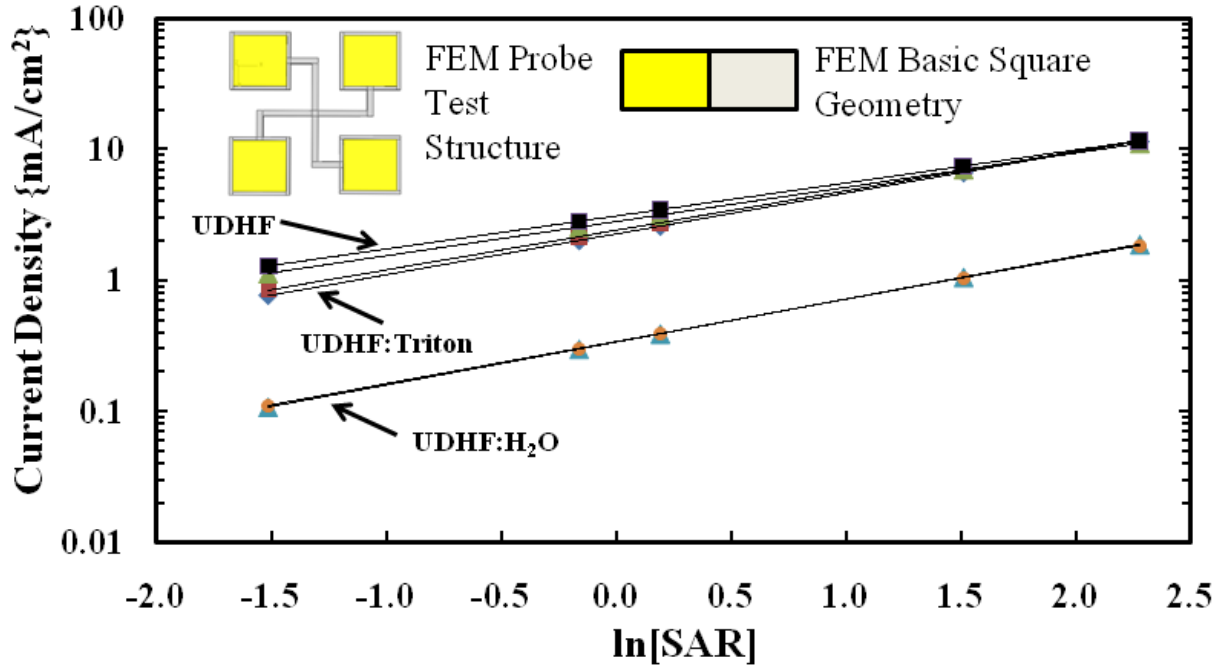


Figure 2.11: Plots of FEM data for unique SAR values of a four-point resistive probe and a simple square geometry model. The results from each model for each HF-based electrolyte are nearly colinear (the arrow for each electrolyte is overlapping both models), with the results from the four-point resistive probe model being slightly larger than the square geometry model.

Experimental results in [33] demonstrated that resistive probe structures of the same SAR as other SOI devices showed nearly identical corrosion current density as other SOI microsystem devices. Therefore FEM should show the same current density for unique devices as long as the SAR and critical device dimensions (*i.e.* micrometer scale devices) are used. For the simple square geometry, Figure 2.11 shows that FEM predicts that current density only varies by a few hundredths of mA/cm² across the Au and Si faces as in the resistive probe model. The trends in

current density with SAR are also nearly identical to those predicted for the more complicated geometry of the resistive probes. Figure 2.11 plots FEM results of both the simple cube model and the resistive probe model with the three electrolytes. The points at each SAR are nearly identical, with the four-point probe model being slightly higher, and this consistency further substantiates the capability of the FEM model to correctly predict corrosion as a function of SAR.

2.6 Conclusion

Reliability of Si microsystems has traditionally focused on issues such as tribology and mechanical robustness. More recent work from the microsystems community indicates the importance of electrochemical corrosion during post-processing on device reliability[33, 81, 36, 37]. The work here demonstrates that on the micrometer scale corrosion damage is uniform in hydrofluoric acid (HF) electrolytes that employ a surfactant. In this work Triton X-100 is used, but alcohol based wetting agents are thought to produce similar results. In HF electrolytes without a surfactant, the damage tends to be greater near the cathode and is nonuniform as distance is increased from the cathode. This is a result of inconsistent wetting of the electrolyte to the Si anode surface.

It is shown that a finite element method (FEM) simulation tool can be applied to analyze corrosion in Si microsystems. A simple geometric test case shows that the FEM simulations accurately predict corrosion using the Tafel equation as a boundary condition. The model makes use of empirical electrochemical polarization curves of silicon (Si) and gold (Au) in HF based electrolytes as boundary conditions in an FEM model of four-point resistive probe microscale devices. FEM predicts a uniform corrosion current density across the device as physically confirmed in FIB cross sections of resistive probes after exposure to a 20:1 (vol:vol) electrolyte

of 48% undiluted HF to Triton-X (UDHF:Triton). The model also accurately reproduces the increasing corrosion current with surface area ratio of Au to Si seen in empirical results. FEM served best for the UDHF:Triton solution and it should be noted that FEM examines the steady state corrosion current for pristine Si. The model predicts a maximum corrosion current density of 2.147 mA/cm^2 for the UDHF:Triton electrolyte compared to a measured maximum current density of 0.479 mA/cm^2 . The measured value will actually lie closer to the model value because current density decreases with increased immersion time and in this study the current density on the device immediately following electrolyte immersion could not be determined and rather related to an average etch rate following a 3 minute immersion. In the case where a surfactant is not present, FIB reveals a factor of six variation in current density (which directly relates to PS thickness) along the leads as well as PS thicknesses that vary across the Si leads.

For future work, FEM can be used to predict damage on other geometries and types of Si as well as in different electrolytes and for different galvanic couples such as platinum-Si. FEM could also be used to simulate the case where a sacrificial anode is employed to mitigate corrosion. The model could find use in predicting PS formation for applications where a galvanic corrosion process is favorable for PS formation compared to an electrochemical technique which requires a power supply and backside contact to the Si substrate.

Chapter 3

Galvanic Etching of Si

3.1 Preface

This chapter is intended to specifically address the morphology of porous silicon (PS) attained by galvanic etching of Si. Results in this chapter present analysis of surface area, porosity, and etch rate of PS that is ideally suited to nanoenergetics. Comparison to PS from electrochemical etching is made to demonstrate that trends in morphology arising from etching conditions (i.e. electrolyte composition and current density) are consistent to those observed with galvanic etching. Very few papers [34, 32, 35] concerning galvanic PS have been published, and these papers limit characterization to a brief mention of porosity and etch rate. Additionally, for nanoenergetics, high specific surface area PS of thickness on the order of tens of microns is desirable. However, previous reports presented data for either low resistivity [35] Si which yields low specific surface area or did not discuss the possibility of thick PS layers on lightly doped, p-type high resistivity (1-30 Ω -cm) Si. A study of the photoluminescence and crystallinity of the PS is also presented for the first time for galvanic PS. This characterization is achieved through gas adsorption studies, scanning electron microscope images, x-ray diffraction, and high resolution transmission electron microscopy.

3.2 Introduction

PS properties and morphology are influenced by a number of factors including Si dopant levels, electrolyte composition and concentration, lighting levels, crystal orientation, Si type (N or P), and applied current density. Properties of PS produced using an electrochemical etching technique [2] have been well characterized. However, the properties and formation

characteristics of galvanic PS have received very limited attention. In addition to aiding in the understanding of PS nanoenergetics, if the properties of galvanic PS are better understood, future applications making use of the material may be found.

In this study, PS with the qualitatively highest energy yield and fastest energy release is desired. Based on our work with calorimetry and velocity, a Si substrate that shatters upon ignition of the PS- NaClO_4 yields the most energy and the flame front propagates at the fastest rate. The specific surface area (m^2/g), pore size, porosity, and pore size are all thought to affect the strength of the PS- NaClO_4 reaction. Therefore we investigate both moderately doped, low resistivity p^{++} ($0.01\text{-}0.02\ \Omega\text{-cm}$) and lightly doped, high resistivity p^+ ($1\text{-}30\ \Omega\text{-cm}$) Si substrates for use in PS nanoenergetics. We find that p^+ substrates, which have pores sizes of only several nanometers in diameter, specific surface areas $> 400\ \text{m}^2/\text{g}$ and porosity similar to 65-80% demonstrate a stronger reaction than p^{++} samples (data presented in Appendix A is intended to supplement the information presented here) which have similar porosity but reduced surface area, $< 400\ \text{m}^2/\text{g}$, and larger pores $\sim 10\ \text{nm}$ compared to p^+ .

Our focus therefore is on p^+ Si substrates. Here we characterize the surface area, pore size, and porosity, and etch rate of p^+ PS formed by galvanic and electrochemical etching. The galvanic PS relies on formation of a galvanic cell between Si and a Pt cathode directly sputtered on the Si. The electrolyte used for galvanic etching is composed of hydrofluoric acid (HF), ethanol (EtOH), and hydrogen peroxide (H_2O_2). The ethanol is used as a surfactant to enable wetting of the hydrophobic surface by the HF as well as to facilitate removal of the hydrogen bubbles from the PS surface that are produced during etching. Etch rate increases with both H_2O_2 concentration and the surface area ratio (SAR) of Pt:Si. An addition of 2.4% by volume of 30% H_2O_2 in water is found to yield PS films of considerable thickness ($\sim > 60\ \mu\text{m}$) on the time

scale of < 30 minutes for the lowest SAR tested of 1:1 and even faster (~10 minutes) for increased SAR. Higher concentrations of H₂O₂ were found to approach the electropolishing regime of PS formation and would yield PS films that were cracked and mechanically unstable. Lower concentrations of H₂O₂ performed at slower than desired etch rates. It is important that etching thick films occurs as quickly as possible to limit damage from the HF attack of other materials deposited on the Si wafer such as a Si₃N₄ etch mask or noble metal electrical traces.

In addition to the morphology evaluation, we investigate the photoluminescence (PL) of galvanic PS to demonstrate this capability of the films. Also, because some debate continues as to whether PS contains amorphous Si, the crystallinity of galvanic PS was investigated by high resolution TEM, Raman spectroscopy, and x-ray diffraction. Our results indicate only crystalline Si is present, however we do note a disordered arrangement of Si crystallites which likely leads to the bimodal size distribution of crystallites observed with XRD.

3.2.1 Electrochemical Etching Methods

We produced PS thin films by a constant current electrochemical technique. We used double side polished, lightly doped p-type (p⁺) wafers (resistivity of 1-30 Ohm-cm). Prior to anodization, we sputtered a Ti/Pt layer on one side of the wafer and annealed in nitrogen for 60 s at 700 °C. This process served to create a backside contact for the wafer. All of our electrolytes are based on 49% HF, and the concentration is reduced to 25% (1 part 49% HF to 1 part EtOH) or 33% (2 parts 49% HF to 1 part EtOH).

The etching process is performed in a custom-built Teflon® cell. The cell is composed of a base and a machined top that is bolted to the base. An o-ring between the base and the top prevents electrolyte leakage. The top half of the cell has a 1.1 cm diameter and 1.6 cm depth cylinder machined out of the Teflon®. We place a piece of aluminum foil between the die and

the base of the Teflon® cell to serve as a backside electrical contact to the Si. We had three identical cells machined and used either a PXI-1042 power supply (National Instruments) or Keithley 2400 source meter power supply to anodically bias the Si die. Unless otherwise noted, all etch times are 30 minutes.

First we scribe our wafers into approximately 2cm x 2cm dice and clamp between the top and bottom halves of the cell. Once the top half of the cell is bolted to the base, the cylinder is filled with electrolyte, and a coiled gold (Au) wire that serves as the cathode is immersed just below the level of the electrolyte. The Au wire is parallel to the Si surface and coiled in a manner to increase the surface area of Au in the electrolyte and reduce variations in current density across the Si surface.

After the etching process is finished, the cell is rinsed with methanol and the PS is kept immersed in methanol as the cell is taken apart. The PS is then rinsed again in methanol and a thin layer of methanol is allowed to slowly evaporate from the PS. For higher current densities, and low HF concentrations, the PS was rinsed with anhydrous pentane (Sigma Aldrich). Pentane has a much lower surface tension than either methanol or ethanol, and has been shown to reduce PS cracking during drying [106].

3.2.2 Galvanic Corrosion Etching Methods

The galvanic etching in this chapter relies on the galvanic cell formation between Pt and Si. This system is used because it is recognized that the etch rate is drastically higher for Pt-Si than for Au-Si. We investigated several strategies to adhere Pt to Si. For reproducible and effective etching, the electrical connection of Pt to Si must be very robust. Typically, an adhesion layer is used between Si and the metal to be deposited. For example, when depositing gold (Au) onto Si, a chrome adhesion layer is used between Si and Au. We thus attempted to

deposit a multilayer film of Cr/Au/Pt using electron beam evaporation as well as sputtering. However, for p^+ Si, the electrical connection is rather poor and despite various annealing and conditions, the etch rate was poor and the metals eventually peeled from the substrate. We additionally attempted a platinum-tantalum (Pt/Ta) metal layer stack reported to have excellent adhesion in HF [107]. While the layer stack was extremely robust and did not peel even after several hours of immersion in HF-based electrolytes, only very minor etching occurred. Eventually, it was determined that directly sputtering Pt onto the Si substrate yielded the best etching results in terms of etch rate and uniformity. Further experimental details and a discussion of annealing the Pt film after deposition is presented in section 3.3.2.

3.3 Morphological Characterization

3.3.1 Electrochemical PS

The gas adsorption measurements are performed according to the BET theory [108] and the porosity measurements are calculated with BJH theory or with a gravimetric technique [109]. A Micromeritics ASAP 2010 with N_2 gas as the adsorbate is used for the analysis. The sample tube for the ASAP 2010 is narrow (~10 mm diameter) so our PS dice are cleaved prior to inserting into the sample tube. In all experiments we determined the mass of the total sample (bulk Si plus PS). From this, the ASAP 2010 software computed a total volume of gas adsorbed per mass.

We were able to determine the mass of just the PS after the gas adsorption measurement was made by using a gravimetric technique. With this technique the mass of the bulk Si plus the PS thin film is measured. The PS is then removed by immersing the sample in a 5% solution of sodium hydroxide. The mass of just the Si substrate is recorded and subtracted from the initial

mass of the samples. The difference in mass is the mass of the PS. Using a Mettler Toledo XP26 micro balance and measuring each sample in triplicate, we could record the mass of just the PS. This mass could then be used to compute a total volume of gas adsorbed in just the PS material. We confirmed, by analyzing bulk Si, that the volume of gas adsorbed by the bulk Si is insignificant (0.6%). The end result is that no errors result from analyzing a composite PS/bulk Si material, and the gas adsorption values correspond only to PS. For reliable results, enough mass to yield several m^2 of PS should be used.

Our primary focus is to characterize the morphological properties of PS such that properties can be coupled with information on the energetic reaction. From this, an understanding of the critical properties necessary for a particular reaction (i.e. tuning the reaction strength) can be determined. The analysis of gas adsorption isotherms has been widely used to determine porosity and pore size distributions in PS [3]. We begin by characterizing electrochemical PS since data in the literature is available with which to compare our values. Figure 3.1 shows a result from a sample of PS prepared with a current density of 18 mA/cm^2 for 30 minutes in an electrolyte composed of 2:1 HF(49% in water):EtOH. The isotherms presented here are noted to be of IUPAC Type IV, indicative of mesoporous (pores 2 – 50 nm in diameter) [110].

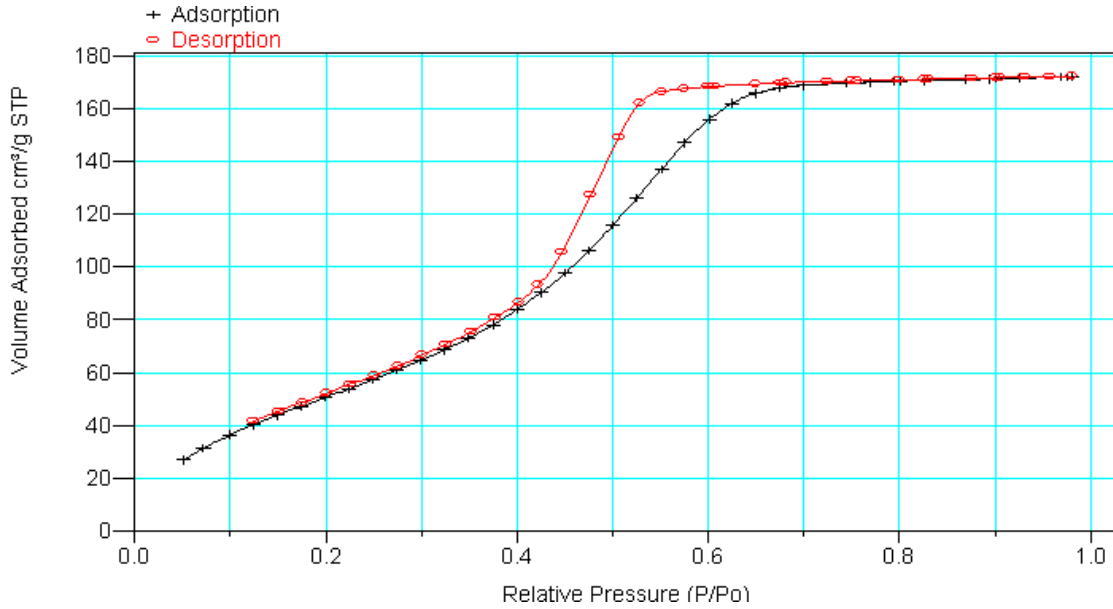


Figure 3.1: Gas adsorption isotherm of porous silicon (18 mA/cm¹ in 25% HF/EtOH electrolyte).

The gas adsorption method begins with N₂ adsorption inside the pores up to a partial pressure of about 0.4. At higher partial pressures, the N₂ actually begins to condense in the pores, and the curve continues until a plateau is reached that indicates all of the pores have been filled. Upon desorption, a hysteresis results from the inherently different conditions of desorption compared to adsorption [110]. For the case of lightly doped p-type Si, the microstructure of the material is observed to be an interconnected fine pore structure [111]. In such a system, it is recommended that the adsorption curve be used for pore size analysis [111]. The approach known as the BJH method is used to analyze the isotherms and obtain a pore size distribution [112, 109].

Figure 3.2 and Figure 3.3 present the pore size distribution versus the cumulative pore volume and the change in volume divided by the change in pore size (dV/dD) respectively. These figures reveal the pore size distribution in the PS is relatively narrow.

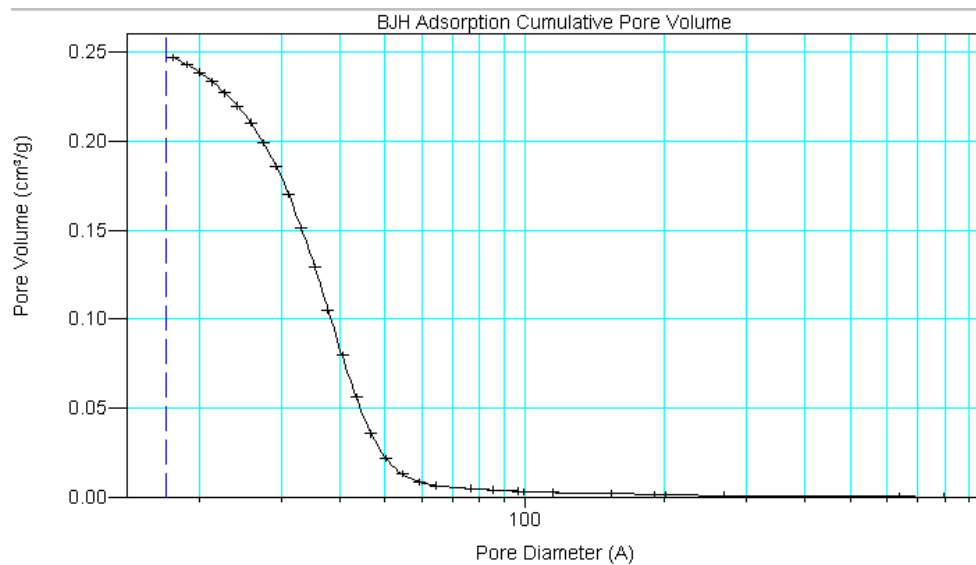


Figure 3.2: BJH adsorption cumulative pore volume of porous silicon (18 mA/cm^2 in 25% HF/EtOH electrolyte).

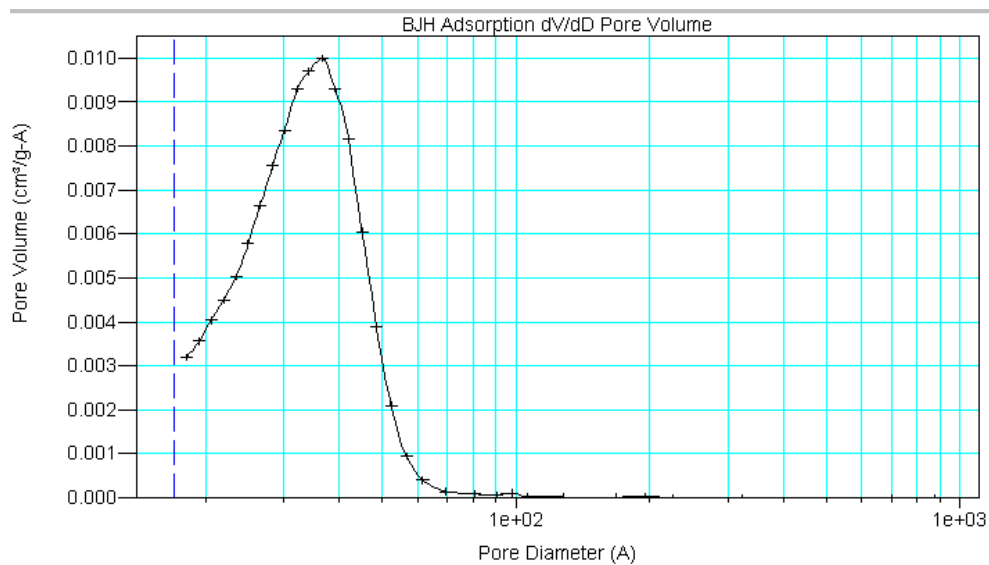


Figure 3.3. BJH adsorption pore volume distribution of porous silicon (18 mA/cm^2 in 25% HF/EtOH electrolyte).

Figure 3.4 presents the pore diameters formed in 1:1 and 2:1 HF:EtOH electrolyte. The trend of increasing pore size with current density follows expected results[108]. The gas adsorption curves in Figure 3.5 demonstrate that the hysteresis becomes less pronounced for smaller pores.

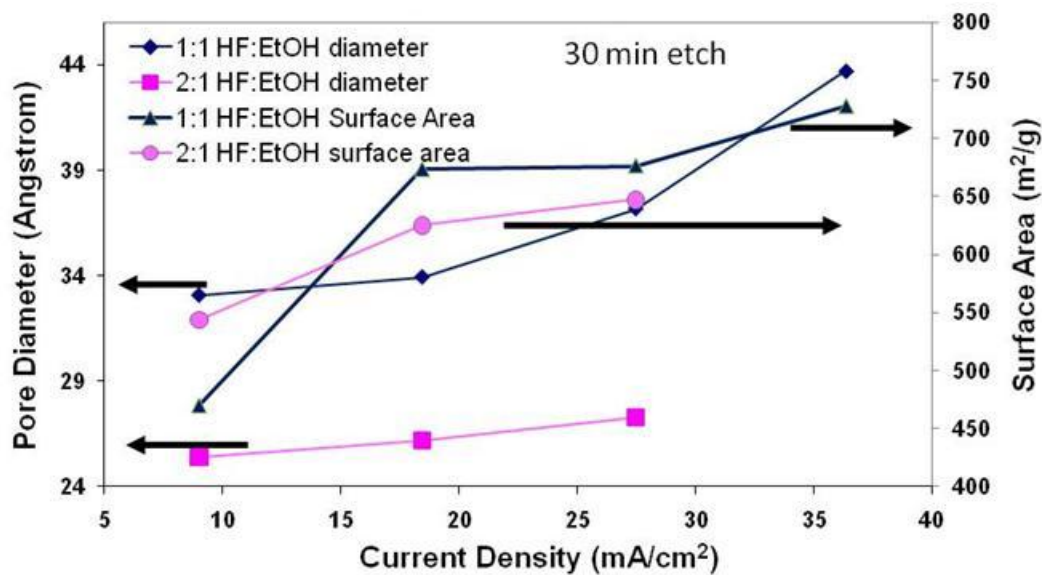


Figure 3.4: Pores sizes and surface area for 1:1 and 2:1 PS at varying current densities for a 30 minute etch time.

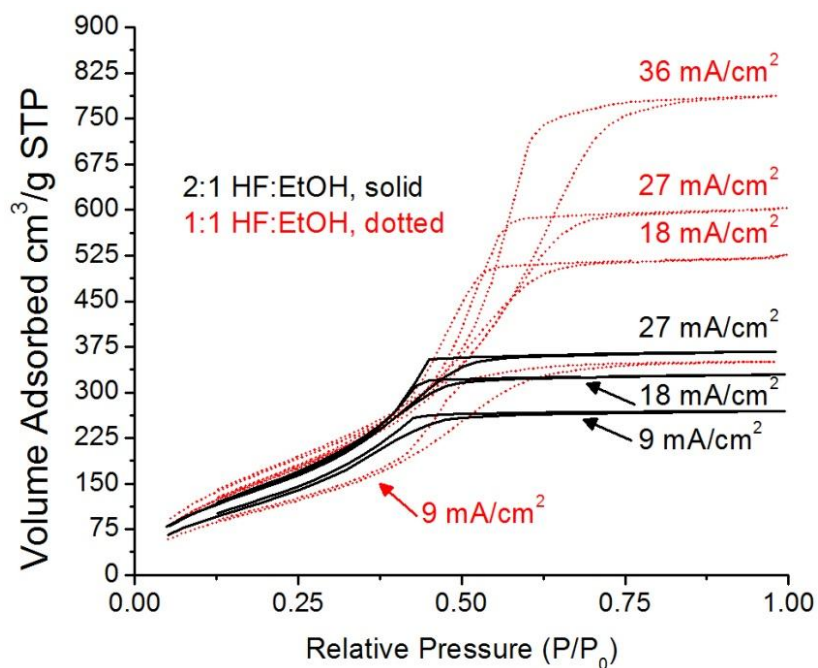


Figure 3.5: Gas adsorption curves for electrochemical PS formed at varying current densities in 2:1 (black, solid) and 1:1 (red, dotted) HF:EtOH.

Ruike et al. have shown, on 20 Ohm-cm Si samples, a mean pore diameter of 3.1 nm, and a much broader distribution of pore sizes (1.8-5.2 nm) at 10 mA/cm² compared to our results. However, Ruike et al. prepared 150 μm thick PS layers compared to our 17 μm thick thin films. Especially in low concentration HF solutions (25% HF or less), a dramatic broadening of pore size range occurs [3]. Ruike et al. does not note a specific etch time, but certainly it was on the order of hours and not minutes and it quite possible the PS network was attacked as hydroxide ions in solution competed to form an oxide layer in the PS network that would be subsequently etched by HF. Canham [3] specifically reports an increase in pore size for the same current density, electrolyte concentration, wafer resistivity, but increased etch time. Additionally, Ruike et al. notes that at the end of the etch, the PS layer was removed from the Si substrate by a high current pulse that served to electropolish the Si underneath and remove the PS layer. We have tried a similar approach using an 18 mA/cm² samples. Our work shows that the mean pore diameter increases from 3.3 to 4.5 nm in this method. Authors seem to differ in their approach on preparing samples for gas adsorption measurement, specifically if they render free-standing PS films, or measure the PS film with the bulk Si substrate[108, 111, 109]. To our knowledge there are no articles reporting on pore size distributions of free standing PS compared to PS still attached to the bulk Si.

Work at the Army Research Lab has concluded that moderately doped Si wafers (p⁺⁺) produce qualitatively weak nanoenergetic reactions evidenced by a dull “poof” noise when the reaction is triggered and a lack of damage to the Si chip. Figure 3.6 and Figure 3.7 show gas adsorption measurements and the corresponding pore sizes and surface areas from PS formed on p⁺⁺ wafers.

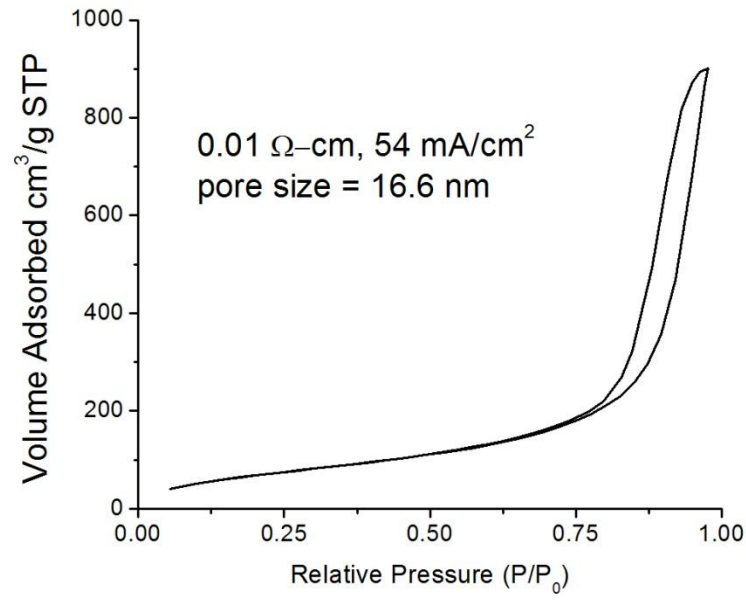


Figure 3.6: Gas adsorption curve for PS formed on p⁺⁺ Si.

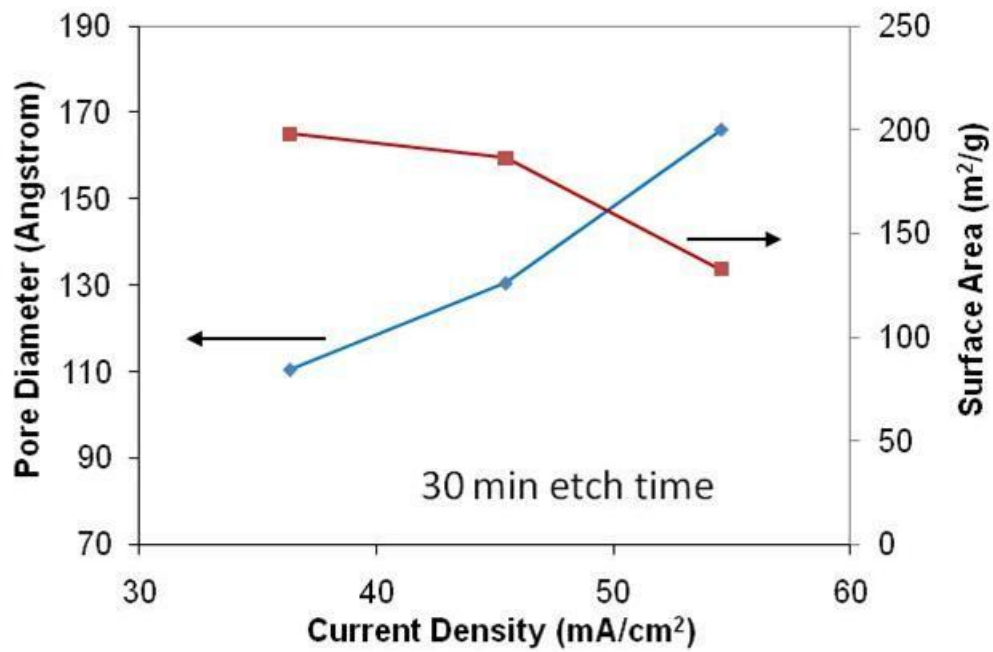


Figure 3.7: Pore diameters and surface areas of PS formed on p⁺⁺ Si.

Pore diameter does increase with current density as expected. The surface areas of these samples are roughly one third of those formed on p^+ wafers and we attribute this decrease to the weak energetic reaction.

Porosity was independently determined by gravimetric analysis. In the gravimetric analysis, the mass of the die prior to anodization (m_1), the mass of the die after anodization (m_2), and the mass of the die after removal of the PS layer in 5% sodium hydroxide at room temperature (m_3) are recorded. The porosity is given by Equation (3.1).

$$P = \frac{m_1 - m_2}{m_1 - m_3} 100\% \quad (3.1)$$

The thickness of the layers was also determined by either cleaving the samples for cross-section or measuring using a scanning electron microscope (SEM). Additionally, PS samples can be immersed in 5% sodium hydroxide solution to remove the PS and then measured with an optical or stylus profilometer with excellent agreement with SEM imaging.

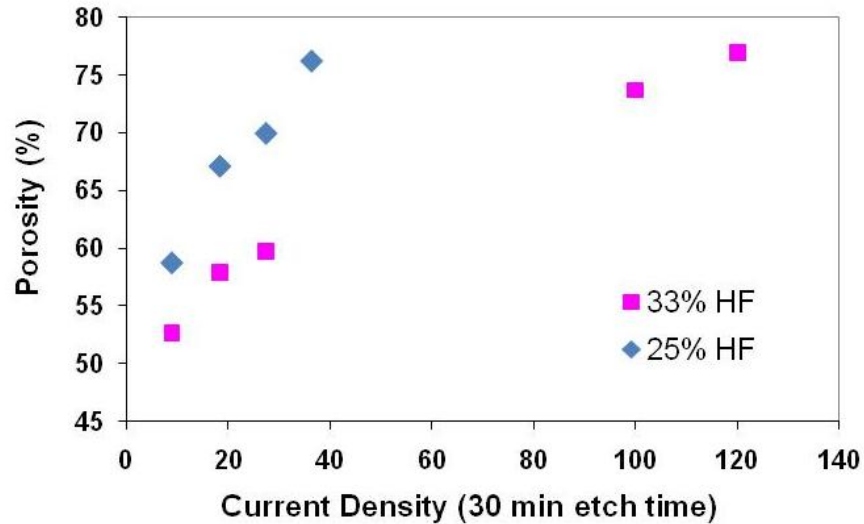


Figure 3.8: Porosity of electrochemical PS.

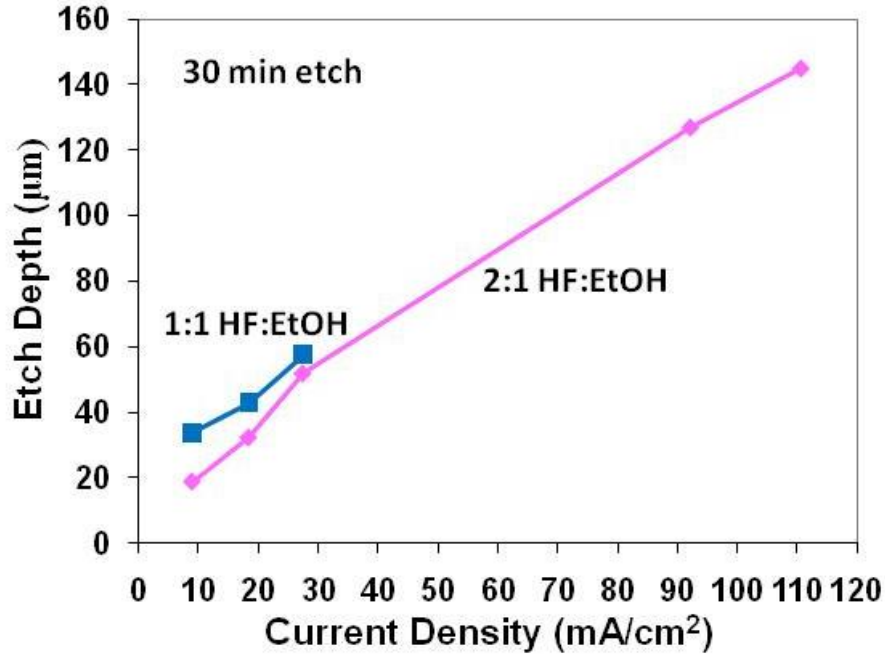


Figure 3.9: Etch depth for electrochemical PS samples are 30 minutes of etching.

3.3.2 Galvanic Porous Silicon

As significant time was devoted to developing the nanoenergetic application for galvanic PS, only the material found to be the most reactive was given a full morphological characterization. Critical to the work here, was the finding that performing an anneal after Pt deposition improved the Pt adhesion and electrical contact with the substrate during etching in HF-based electrolytes. Figure 3.10 shows the Pt film after a 30 minute etch in 3:1 HF:EtOH with 2.4 % H_2O_2 without an anneal, (a), and with an anneal (b). It is clear that the Pt film is left nearly unaffected by etching when an anneal has been performed.

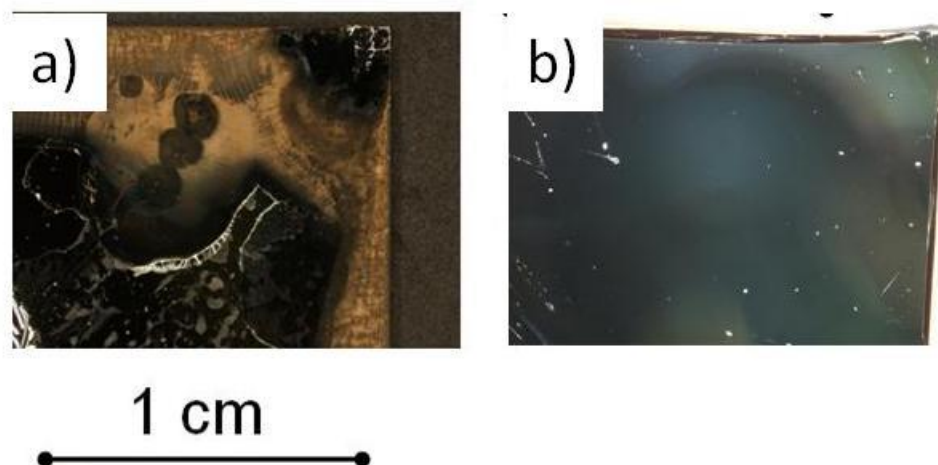


Figure 3.10: The backside of a Si wafer showing the Pt thin film after 30 minute etching in 3:1 HF:EtOH composed of 2.4% by volume H_2O_2 without a Pt anneal (a), and with a Pt anneal (b). In (a) dark regions appear where Pt has peeled and PS has been generated and in (b) the Pt thin film is left intact.

Prior to realizing the drastic improvements resulting from annealing, the choice of electrolytes was initially limited to ratios of HF to EtOH that were less than 5:1. Above this concentration the Pt would peel very quickly from the wafer. After annealing however, the Pt becomes remarkably stable and electrolyte compositions of HF:EtOH up to 200:1 were tested with very little degradation to the Pt layer even after 30 minutes of etching. While the annealing step has been determined to certainly improve the etching uniformity and Pt layer stability, the exact nature of the interface of the Pt-Si may require further investigation. The literature reports that the Pt-Si interface forms platinum silicide upon annealing [113, 114] provided the surface is oxide free. We have had excellent success and reproducibility using a sputter etch prior to sputter deposition of Pt to remove the native oxide. However, when rinsing the wafer with HF to remove a native oxide and forgoing the sputter etch, the Pt adhesion remains poor. When using a buffered oxide etchant with surfactant, the results are dramatically improved; however, the Pt adhesion is not as robust as with the sputter etch. This likely stems from native oxide growth on

the wafer surface during the time between the HF rinsing and the sputter deposition, despite the reports in the literature that use this method to remove native oxide prior to Pt deposition.

This work initially investigated whether the igniter developed by ARL [69] could be patterned on the Si substrate prior to galvanic etching and yet survive the etching process (the reader is directed to Chapter 6 and Appendix B for a more detailed discussion of the Microsystems process flow). As shown in Figure 3.11 with an SEM image a) and in an optical image in b) the wire remained nearly unaffected. The igniter wire is fabricated with a stack of Cr/Pt/Au on top of a Si_3N_4 layer. As Au does not catalyze H_2O_2 breakdown [32], local etching near the igniter wire is likely very low and the wire is able to withstand the galvanic etching process very nicely.

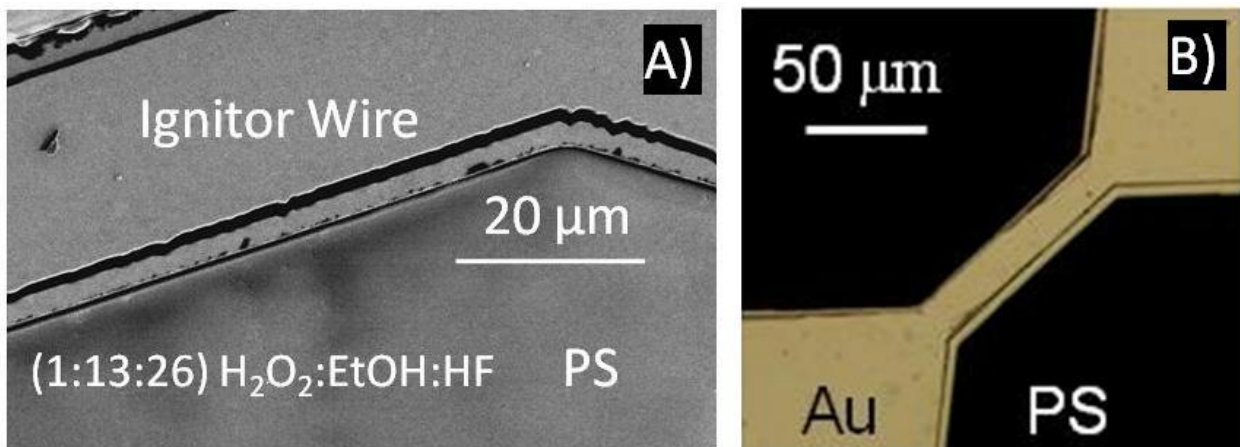


Figure 3.11: A) SEM image of the igniter wire after 10 minutes of galvanic etching. B) Optical image of the igniter wire.

The concentration of HF in an electrolyte solution is known to have limited impact on the etch rate of Si [3], however the current density can dramatically affect etch rate. For galvanic PS the current density is controlled by the SAR, oxidizer concentration (in this case H_2O_2), and the electrical connection of the Pt to the Si wafer. Figure 3.12 shows the general trend of etch depth

for a 10 minute etch in 3:1 HF:EtOH for various SAR values and H_2O_2 concentration. When this data is compared to that of Figure 3.9, the highest etch rates ($\sim 4 \mu\text{m}$ of PS formed per minute) are comparable to those of electrochemical PS using over $100 \text{ mA}/\text{cm}^2$. For SAR greater than 1, the cross sections of Si regions that had been opened from a Si_3N_4 mask were inspected by SEM after etching. In these cases, the Pt layer was deposited in direct contact with the backside Si, while the active Si regions for PS formation were on the top side of the Si wafer. It should be noted that for a $\text{SAR} > \sim 5$ the etch rate becomes very high for the 0.7% H_2O_2 concentration and considerable variability may be introduced into etches from sample to sample depending on exactly how robust the Pt:Si connection is, the exact dopant concentration of the wafer, etc.

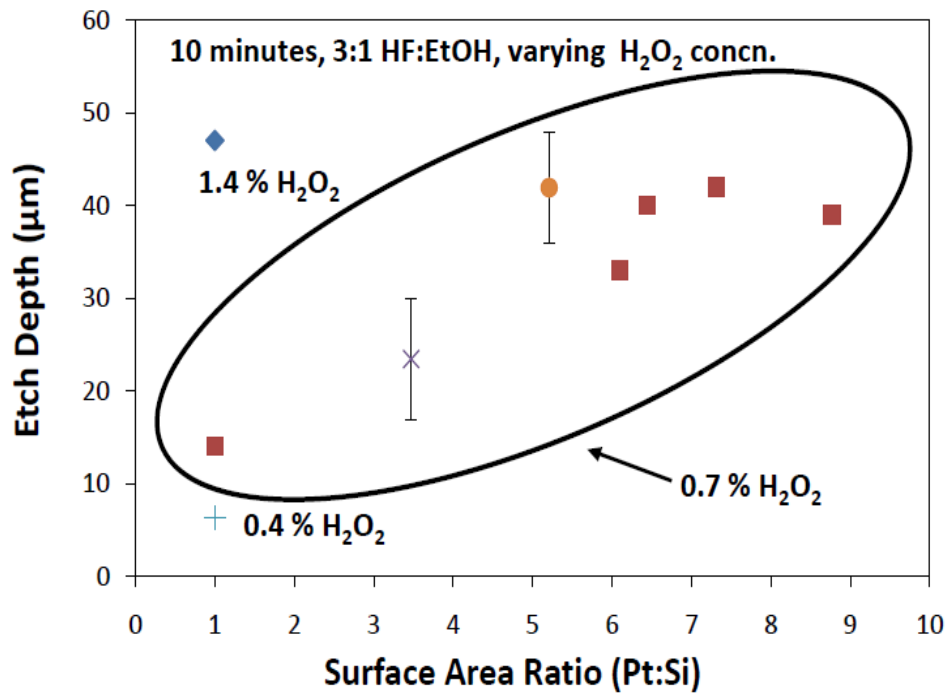


Figure 3.12: General etch depth trends based on H_2O_2 concentration and SAR for p^+ Si without performing an anneal after Pt deposition.

If the ratio of HF:EtOH is reduced below 3:1, the PS is highly susceptible to cracking during etching and if the concentration is increased above 20:1, the etching uniformity begins to degrade. In the former case this is a result of creating highly porous layers that lack structural integrity, in the latter case, this results from poor wetting of the Si with such a limited quantity of EtOH present. The 3:1 and 20:1 electrolyte compositions were used in the work presented in Chapter 6 for velocity studies, and gas adsorption results are presented here in Figure 3.13. The isotherms are IUPAC Type IV as mentioned in the previous section. Here the 20:1 PS isotherm has a very slight hysteresis as a result of pore sizes only 2.4-2.5 nm in diameter.

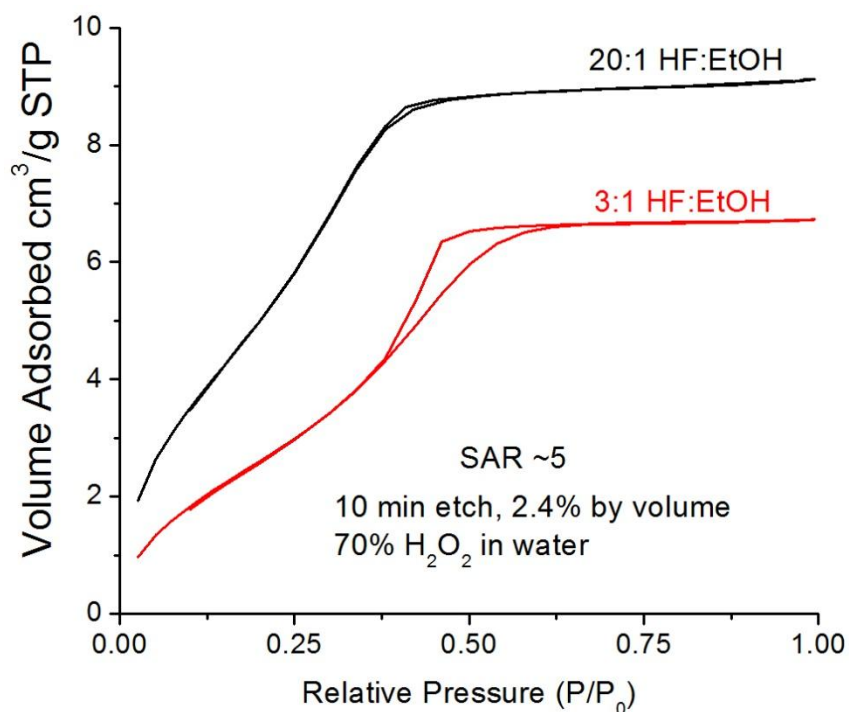


Figure 3.13: Gas Adsorption for galvanic PS

The surface area is computed using the BET method as is typically employed for PS measurements and is similar to 840 and 900 m²/g for 20:1 and 3:1 PS respectively (see Appendix B for experimental details). The specific surface area (m²/g) is calculated by destructively

measuring the mass of the samples. The mass of the entire velocity strip with PS is recorded using a Mettler Toledo XP26 microbalance with a 1 μg resolution. The PS is then removed by immersing the chip in a 5% NaOH solution at room temperature until all PS is removed. The samples are again weighed. The pre-NaOH and post-NaOH mass are subtracted to yield the mass of PS. The total surface area of the velocity strip sample is then divided by mass to give surface area in m^2/g . The porosity of the samples is measured as discussed in the previous section and is 65-67 and 79-83% for the 3:1 and 20:1 samples respectively.

3.4 Galvanic Porous Silicon Microstructure

The observation of room temperature photoluminescence (PL) from PS sparked an enormous interest in the material [3]. Countless studies have investigated PL of PS and the reader is directed to the introduction for a list of references discussing various aspects of PS photoluminescence. Typically studies involve high resolution TEM investigations, Raman spectroscopy, and XRD alongside PL measurements. With results from these tools a comprehensive knowledge of the structure of PS can be attained. Galvanic PS has not been investigated with these methods. The results presented here give an insight into the structure of galvanic PS. The samples analyzed here are the same samples used in Chapter 4. The goal of this work was to determine if amorphous Si is present in galvanic PS. Nanoscale amorphous Si may impact the exothermic reaction of nanoenergetic PS through re-crystallization of the amorphous Si during heating [115] or from direct combustion of amorphous rather than crystalline Si.

Figure 3.14 shows the PL spectra of the films. The 60 minute film has a dramatic increase in intensity and a blue shift relative to the 30 minute sample. The inset shows an optical image of the 30 and 60 minute films under white light and under UV light. The edges of the 30

minute sample have a more intense PL as a result of their proximity to the backside Pt coating and subsequent high etch rate and probable thinning of the PS structure. Additionally, it is suggested the etching process results in a “disordered”, possibly amorphous Si region surrounding the pores that can be dissolved during long etches[116]. This would also give rise to the increased PL.

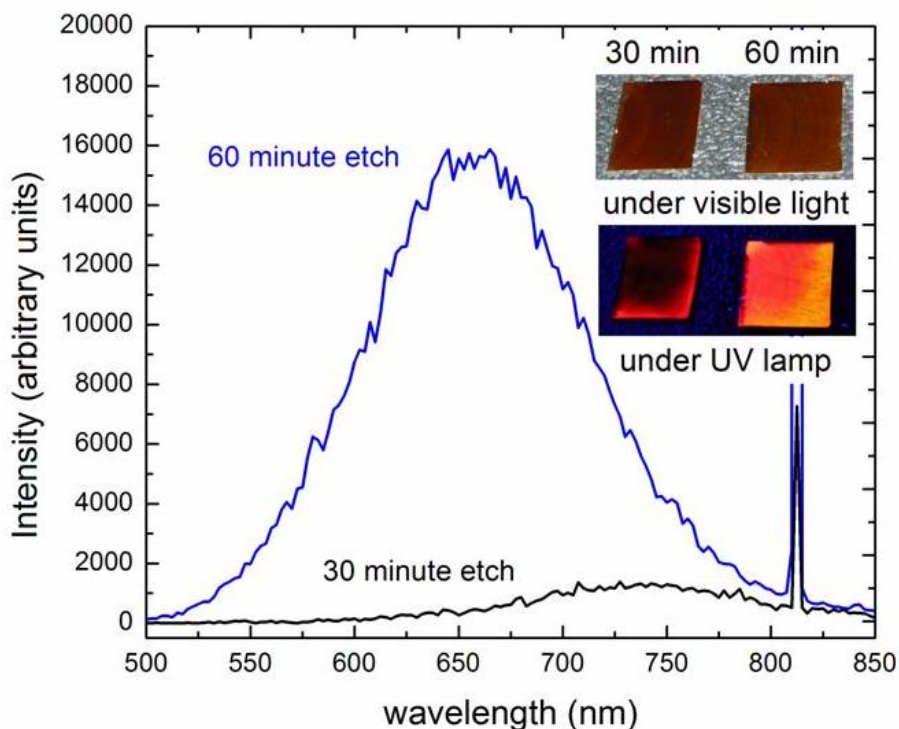


Figure 3.14: PL spectra of 30 min and 60 min galvanic PS

PS powder can be prepared from the PS films by either placing the PS in an ultrasonic bath to break apart the film [117], Figure 3.15, or by simply using a razor blade to scrape off the film[116]. In either case the powders are PL active. The powder maintains this PL even when exposed to air at room temperature.

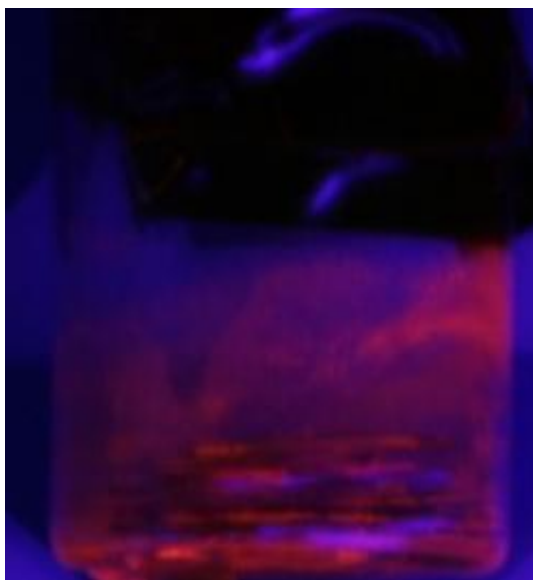


Figure 3.15: PS powder (orange PL) in a glass vial under UV illumination after being broken apart from the Si wafer in an ultrasonic bath. Some of the powder has coated the walls of the vial, while in the bottom the original PS chips are submerged in ethanol. The ethanol is not anhydrous and the vial was sealed in laboratory air.

In the following discussion we focus only on PS powder prepared by removal with a razor blade since no solvent is necessary in this technique. The powder can be analyzed by x-ray diffraction without any possible contributions from the Si substrate. Figure 3.16 shows the XRD pattern of 30 and 60 minute PS powder. There are two size domains indicated by the broad base of the Si peaks. Using a Scherrer analysis, the size domains are 117.4 and 5.7 nm for the 30 minute sample and 123.9 and 4.7 nm for the 60 minute sample. This indicates that the additional time in the etch solution does reduce the size of the Si crystallites, which is in agreement with the slight increase in specific surface area mentioned before. Additionally, this finding agrees well with a similar result for n-type PS studied with Raman spectroscopy[116].

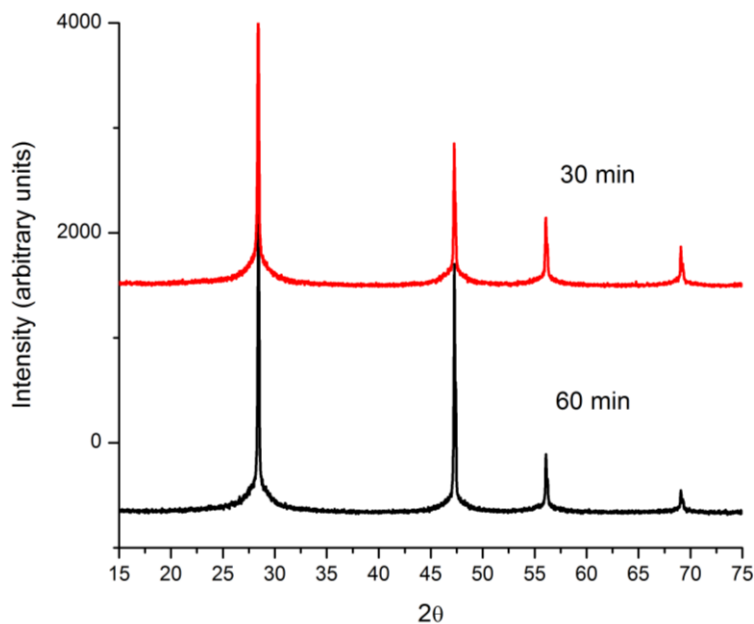


Figure 3.16: XRD spectra of 30 and 60 min PS powders.

Transmission electron microscopy is used to analyze the structure of the PS. Figure 3.17 a) shows the view of a large fragment of the 30 minute PS powder. The diffraction pattern of the powder shows arc shaped spots indicating the orientation of Si crystallites may deviate from the original single crystal structure. Figure 3.17 b) is a high resolution TEM image where crystalline fringes are clearly seen as well as regions (seen best in lower half of the figure) where no fringes are present and are indicative of the porous structure. Figure 3.17 c) is a high resolution TEM image of 60 minute PS powder. The upper left corner is on the boundary of the powder and the TEM grid, but in the lower right there are regions where the lattice fringes are distorted or missing indicating the porous structure. No obvious differences appear between 30 and 60 minute PS under TEM, and both samples seem to have very little amorphous or otherwise “disordered” material.

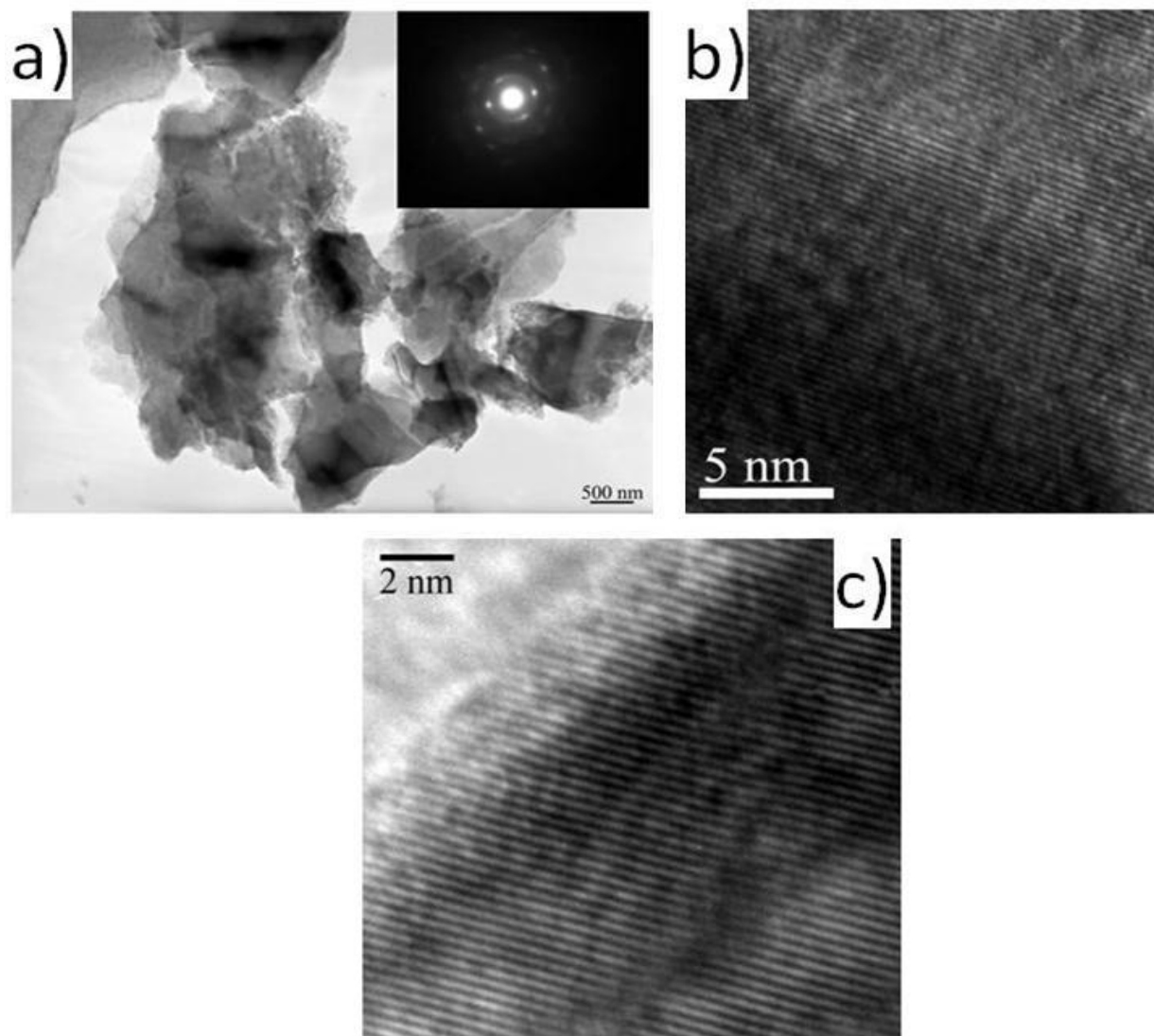


Figure 3.17: High resolution TEM images of PS powder. a),b) 30 minute PS powder. c) 60 minute PS powder.

We further investigate galvanic PS for amorphous material with TEM studies. Figure 3.18 shows a TEM image of 30 minute PS powder which indicates there are regions lacking a crystalline structure as no fringes are observed. This may indicate an amorphous region, however the Raman spectra, Figure 3.19, only reveals a crystalline Si signal. Additionally, in the crystalline region, lattice fringes are misaligned to one another, in agreement with the arcs in the

diffraction pattern. This also agrees with the XRD pattern in which two size regimes are distinguished: since some crystallites are misaligned, they will not produce a coherent signal and are seen as the broad region, however, the crystallites that are still aligned with the original substrate orientation produce a coherent signal and are seen as large size (100's of nm) crystallites[13]. A higher stress and smaller particle size are thought to result in increased PL intensity and a blue shift of the PL signal. The Raman results in Figure 3.19 seem to corroborate this theory as the 60 minute Raman peak is wider as a result of increased stress compared to the 30 minute sample. However, laser power density can have a dramatic effect on the Raman signal as heat induces stress into the sample and we have seen a shift in the spectrum even for very lower power densities but at long collection times. Therefore, while the Raman signal eliminates the possibility of amorphous Si regions, it is not clear if the 60 minute samples are indeed of higher stress.

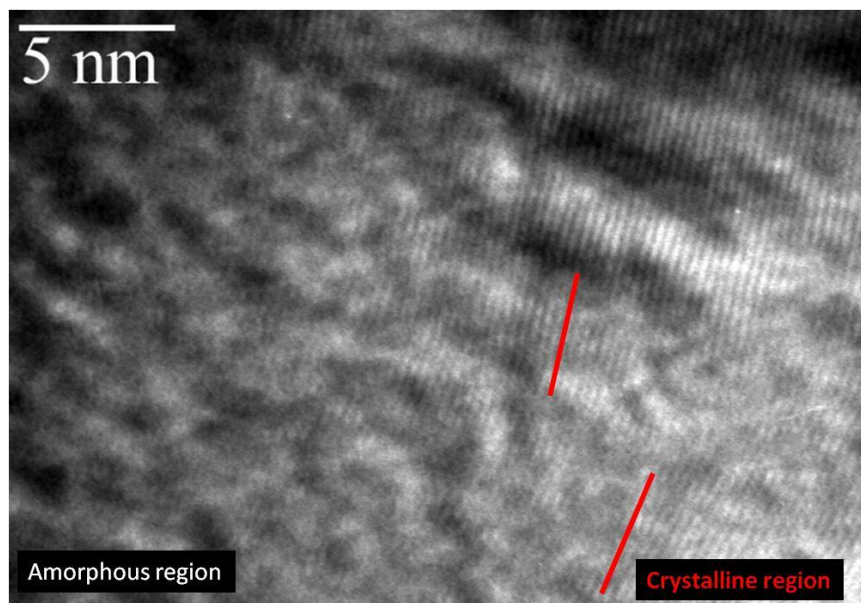


Figure 3.18 High resolution TEM image of 30 minute PS powder showing Si crystallites with unique alignment. The red lines help guide the eye to the alignment of the Si crystallites.

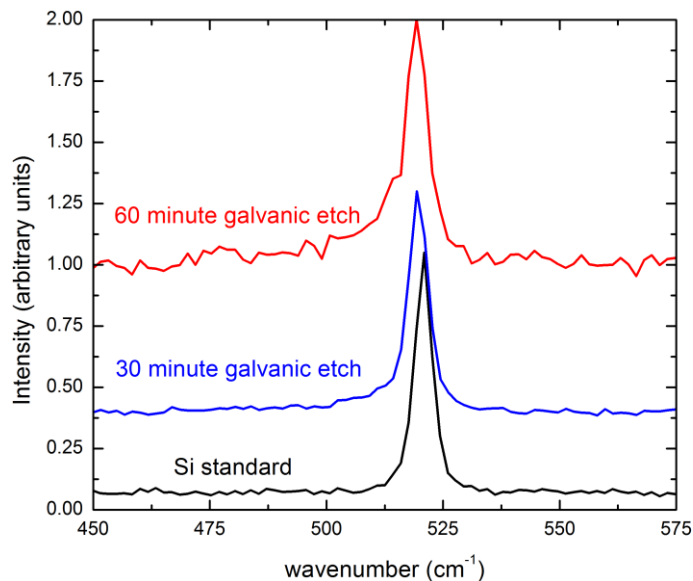


Figure 3.19: Raman spectra of 60 and 30 minute PS thin films and Si single crystal substrate.

3.5 Conclusion

The material in this chapter presents a characterization of both electrochemical and galvanic porous silicon. This characterization is necessary so that a better understanding of the nanoenergetic capabilities of PS can be gained. Techniques used for characterization include TEM, gas adsorption, SEM, PL measurements, XRD, and Raman spectroscopy. Unfortunately, much of the characterization of PS requires destruction of the PS film. Thus, for work in other chapters of this thesis one set of samples is typically prepared for nanoenergetic testing while the other set of samples is prepared for properties analysis. This has the drawback of being time intensive and great care must be taken to ensure sample preparation is identical for both sets of samples. However, characterization is absolutely critical to further improvements in the nanoenergetic capabilities of PS.

Chapter 4

Thermal Analysis of the Exothermic Reaction between Galvanic Porous Silicon and Sodium Perchlorate

4.1 Preface

This chapter contains text and figures from a published article by C.R. Becker in the journal *ACS Applied Materials and Interfaces*[118]. Permission to reproduce this work in a thesis is granted by the publisher. The work in this chapter represents the first differential scanning calorimetry (DSC) and bomb calorimetry studies performed on galvanic porous silicon. Additionally, to the author's knowledge this is the first successful report of DSC on any type of porous silicon (electrochemical or galvanic). In this chapter porous silicon films up to $\sim 150\ \mu\text{m}$ thick with specific surface area similar to $700\ \text{m}^2/\text{g}$ and pore diameters similar to $3\ \text{nm}$ are fabricated using a galvanic corrosion etching mechanism that does not require a power supply. After fabrication, the pores are impregnated with the strong oxidizer sodium perchlorate (NaClO_4) to create a composite that constitutes a highly energetic system capable of explosion. Using bomb calorimetry, the heat of reaction is determined to be $9.9 \pm 1.8\ \text{kJ/g}$ and $27.3 \pm 3.2\ \text{kJ/g}$ of PS when ignited under N_2 and O_2 , respectively. DSC reveals that the energy output is dependent on the hydrogen termination of the PS.

4.2 Introduction

Porous silicon (PS) is a widely studied material fabricated by electrochemically etching a silicon (Si) wafer to produce a porous structure that can have a thickness of a few nanometers to hundreds of micrometers [3]. When the pores of PS are loaded with any one of a number of oxidizers, PS can function as a highly energetic material [67, 68]. After loading with oxidizer,

the PS-oxidizer composite is typically stable until triggered by a mechanical impact, spark, or heating. Upon one of these stimuli, the composite demonstrates an exothermic reaction ranging from an explosion traveling several kilometers per second that produces a bright flash, a loud audible report, a shattered silicon (Si) substrate, and a significant pressure rise from gas evolution to a less powerful burning of the material traveling only centimeters per second that does not shatter the Si substrate. PS has the advantage of being monolithically integrated into a Si chip and fabricated alongside traditional Si microelectronics and MEMS [69]. With the success of achieving an on-chip energetic material, there is interest in fine-tuning PS to serve in applications that demand on-chip power, fuzing, propulsion, or heat. However, the reaction mechanism for energetic PS is not well understood and there is very limited data regarding the heat of reaction, ignition temperature, velocity, or pressure rise of the PS explosive reaction.

In this Letter, an explosive composite of PS and sodium perchlorate (NaClO_4) is investigated. The PS is fabricated using a galvanic corrosion technique in which thick (up to $\sim 150\ \mu\text{m}$) films are prepared without the requirement of a power supply, an approach well-suited for Microsystems batch processing. In a similar method to prior work in the literature [68, 71, 119], a solution of sodium NaClO_4 in methanol (MeOH) is drop cast on the material to fill the pores in the PS and function as the oxidizer. The composite is stabilized from oxidation by the hydrogen termination of the internal PS surface area as a FT-IR spectroscopic analysis demonstrates. The extent of the reaction is observed with bomb calorimetry in nitrogen (N_2) and oxygen (O_2) atmospheres. Without the supplementary O_2 environment, the heat of reaction is measured to be $9.9 \pm 1.8\ \text{kJ/g}$, but with supplementary O_2 the reaction yields $27.3 \pm 3.2\ \text{kJ/g}$ and approaches the theoretical value of $33.0\ \text{kJ/g}$ for complete Si oxidation by NaClO_4 .

As a complimentary technique to bomb calorimetry, DSC is used to heat the entire sample at a slow rate so that information regarding events prior to explosion is revealed. Results indicate that PS catalyzes complete NaClO_4 decomposition once the hydrogen termination has been removed; these surface hydrides desorb from the PS surface at temperatures above approximately 450°C . If decomposition is triggered locally, i.e. the global network of pores still retains hydrogen termination, an explosion is produced. This is evidenced by a shattered Si substrate and a dent in the copper seal of the stainless steel high pressure DSC pan resulting from high pressure gas evolution. However, if hydrogen termination has been completely removed from the PS, heat is evolved from Si oxidation but no explosion is observed. Additionally, little to no gas production occurs as even aluminum DSC sample pans not intended to withstand pressure are undamaged. These results demonstrate the important role hydrogen plays in the exothermic reaction of PS with NaClO_4 .

4.3 Galvanic PS Samples for Thermal Analysis

Traditional PS formation requires electrical connection to a Si chip immersed in a hydrofluoric (HF) acid-based electrolyte[3]. The Si is biased to promote holes to the semiconductor-electrolyte interface which serve to oxidize Si atoms and etch the wafer according to equations (4.1) and (4.1)(4.2) [34].



However, in the presence of a chemical oxidant such as dissolved oxygen or hydrogen peroxide (H_2O_2), a noble metal such as platinum or gold can be directly deposited on Si to serve as a cathode while the Si acts as the anode to form a galvanic cell that enables Si etching without requiring an external current source [34, 32, 75, 33, 36, 35, 31]. The reaction is cathode limited,

and by varying the surface area ratio (SAR) of metal to Si, the current can be controlled [33, 31]. Additionally, the choice of electrolyte composition, oxidizing agent, noble metal, Si resistivity, Si dopant type (p- or n-type), and reaction conditions such as stirring control the morphology of the material. Here, platinum (Pt) serves as the cathode and H_2O_2 as the oxidizing agent on P-type Si wafers with a resistivity of 1-20 $\Omega\text{-cm}$.

Thin film adhesion of Pt to Si is critical for the galvanic mechanism. Without robust Pt adhesion, the HF-based electrolyte will attack any oxide underlying the Pt film, remove the Pt, and inhibit PS formation. Here, Pt adhesion is achieved by performing a sputter etch to remove any native oxide (alternatively, a two minute immersion in 10:1 buffered oxide etch (10:1 (v:v) of 40% NH_4 in water to 49% HF in water, Honeywell) followed by sputtering of a 170 nm thick Pt film directly on the Si wafer. Subsequently, a 350°C anneal for two minutes promotes formation of a platinum silicide, which enhances electrical connectivity to the Si substrate[113]. With this method, an increase in etch rate and improved PS structural stability to previous reports of galvanic PS are achieved. The wafer can be etched in HF-based electrolytes for up to 60 minutes with minimal degradation to the Pt layer and at a high etch rate ($\sim 2 \mu\text{m}/\text{min}$) with only the backside of the Si wafer coated with Pt (1:1 SAR).

Figure 4.1 shows the cross sections of PS formed on Si wafers with a 1:1 SAR after an (a) 30 minute and (b) 60 minute galvanic etch in an HF-based electrolyte. The electrolyte is a 3:1 by volume solution of 49% HF in water (Honeywell) and ethanol (EtOH) respectively, with 2.4% by volume of 30% H_2O_2 in water (Honeywell). Mildly stirring the solution both increases the etch rate and improves uniformity of the PS layer across the Si wafer.

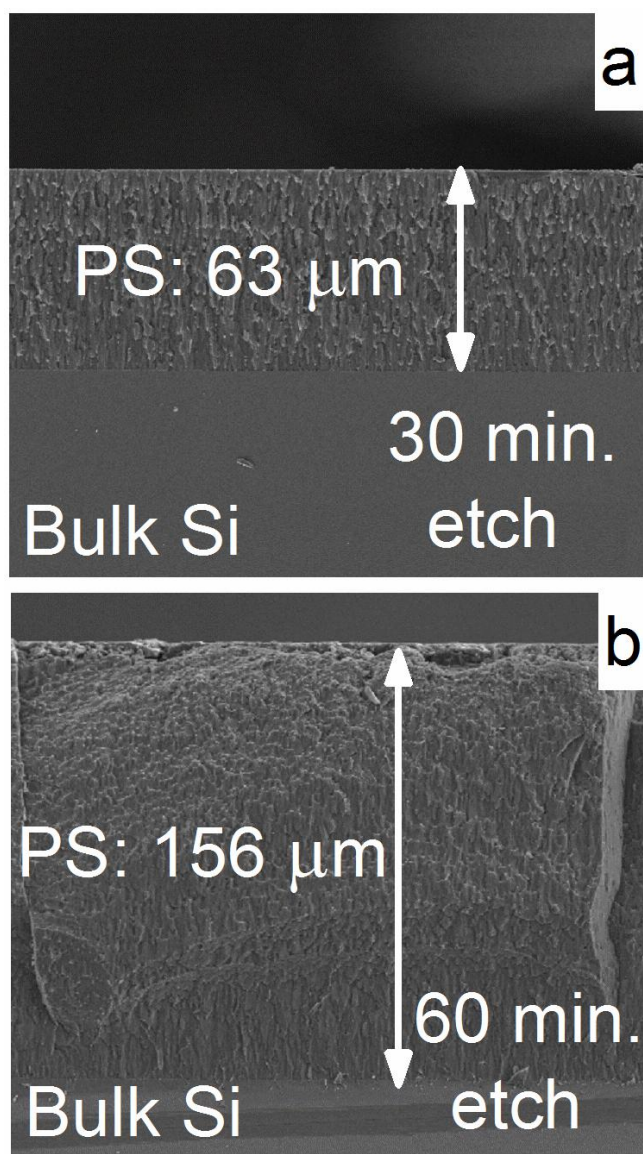


Figure 4.1: Cross sections of PS formed after (a) 30 minute and (b) 60 minute etch.

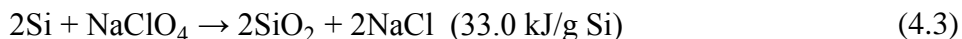
For thermal analysis, Si samples approximately 3 cm by 3 cm were etched for 30 or 60 minutes under the same conditions as in Figure 4.1. The porosity was measured gravimetrically as 63 and 68%, respectively. Gas adsorption analysis by the BET [112, 108, 109, 111] method finds the pore sizes to be 2.65-2.70 and 2.90-3.05 nm and surface areas of approximately 680 and 710 m²/g for the 30 minute and 60 minute samples, respectively. The mass of the PS layer was

determined by an indirect gravimetric technique. In this method, the calorimeter sample is fractured into several parts. One part is used for calorimetry while the PS mass is measured using a destructive gravimetric technique with the remaining parts [3]. The mass of PS per mass of PS plus Si substrate is calculated and assumed to hold for the sample in the calorimeter.

The PS- NaClO_4 energetic material is prepared by drop-casting a 3.2 M NaClO_4 (anhydrous) in MeOH solution onto the PS chip and drying for at least 15 minutes in a nitrogen (N_2) filled glove box. During drop-casting the solution is dispensed from a syringe such that a thin layer of liquid covers the PS. Upon drying, small white crystals of NaClO_4 are observed on top of the PS. Only the 30 minute PS was used for bomb calorimetry, with the mass of samples used for the experiments varying from 19.05 to 64.11 ± 0.01 mg ($1.4 - 4.6 \times 10^{-3}$ moles Si). Once dry, the samples are sealed in the calorimeter bomb (Parr Instruments 1109A) and tested in a combustion calorimeter (Parr Instruments 6725) using a nickel-chrome fuse wire (Parr Instruments 45C10) for ignition. The ignition of 60 minute samples was found to be very sensitive to friction, and since the fuse wire of the bomb calorimeter must physically contact the sample prior to ignition, the samples were too unstable for bomb calorimetric analysis. However, the 30 and 60 minute samples could be used for DSC (TA Instruments 2920) analysis. The mass of PS samples for DSC ranged from $0.52\text{-}0.69 \pm 0.01$ mg ($1.9\text{-}2.5 \times 10^{-5}$ moles Si) and $0.60 - 1.17 \pm 0.01$ mg ($2.2\text{-}3.9 \times 10^{-5}$ moles Si) for 30 and 60 minute PS respectively.

4.4 Gravimetric Analysis of PS- NaClO_4

Heats of reaction are estimated from standard heats of formation where the reaction most likely follows equation (4.3). As a reference, according to equation (4.4), 32.5 kJ/g are liberated when Si reacts with just O_2 .



For consistency, the computed heat of the reaction is given in terms of grams of Si only. There is a challenge in determining the mass of NaClO₄ oxidizer because it tends to coat the surface of the PS and crystallize outside the pores. Since the material is very friction sensitive, the exposed oxidizer is difficult to physically remove without unintentionally igniting the PS sample. Further, cleaving the sample to view the NaClO₄ within the pores in cross section would result in sample ignition. However, an upper limit for NaClO₄ loading in the pores is found by gravimetric analysis of PS-NaClO₄ samples used for DSC. This analysis indicates a 0.087 to 0.303 and 0.109 to 0.125 molar ratio of NaClO₄ to Si for 30 and 60 min PS, respectively. Equation 3) requires a molar ratio of 0.5 NaClO₄ to Si for complete oxidation of all of the PS, thus indicating that the expected experimental heat of reaction will range from 17-61% of theory. It is stressed though that some of this NaClO₄ mass may reside on top of the PS film and not actually be contained inside the pores where it most likely reacts with Si.

PS is organophilic such that the MeOH-NaClO₄ solution is drawn into the pores and it is assumed for the sponge-like network of pores that it is loaded uniformly. The simple model in Figure 4.2 a) demonstrates the theoretical capacity of a PS film to contain NaClO₄. From the density and molecular weight of Si and NaClO₄ the molar ratio of fuel to oxidizer (assuming all of the NaClO₄ is able to react with all of the Si) is computed versus porosity and plotted as the solid line in Figure 4.2 a). The only porosity that can achieve the 0.5 molar ratio required for complete combustion is 67% which also corresponds to the porosity of the 60 minute PS. The experimental molar ratios lie below the theoretical capacity, indicating the porous structure is not completely filled by NaClO₄.

4.5 Thermal Analysis Results and Discussion

The bomb calorimetry data in Figure 4.2 b confirms that the PS combustion reaction is most likely fuel-rich. When the calorimeter bomb is filled with either nitrogen or with dry air at atmospheric pressure the heat of the reaction, ΔH , is 10.8 ± 2.1 kJ/g and 9.9 ± 1.8 kJ/g respectively, well below the theoretical energy density. To confirm that the reaction is fuel rich, the bomb was filled with ~ 20 psig of O_2 ($\sim 1.2 \times 10^{-3}$ moles), which is slightly less O_2 than is theoretically needed to react with all the PS, but a low enough pressure to not spontaneously ignite the sample (note: high pressure O_2 at ~ 400 psig will spontaneously ignite the sample, and care should be taken when working with O_2 and energetic PS). In this case, the heat of reaction increases to 27.3 ± 3.2 kJ/g, which is near the theoretical limit of the reaction if all of the Si atoms in the PS network are oxidized. This indicates that the explosive reaction reaches temperatures such that oxidation by O_2 diffusion into the nanoscale Si domains of PS is possible, providing enough O_2 is present.

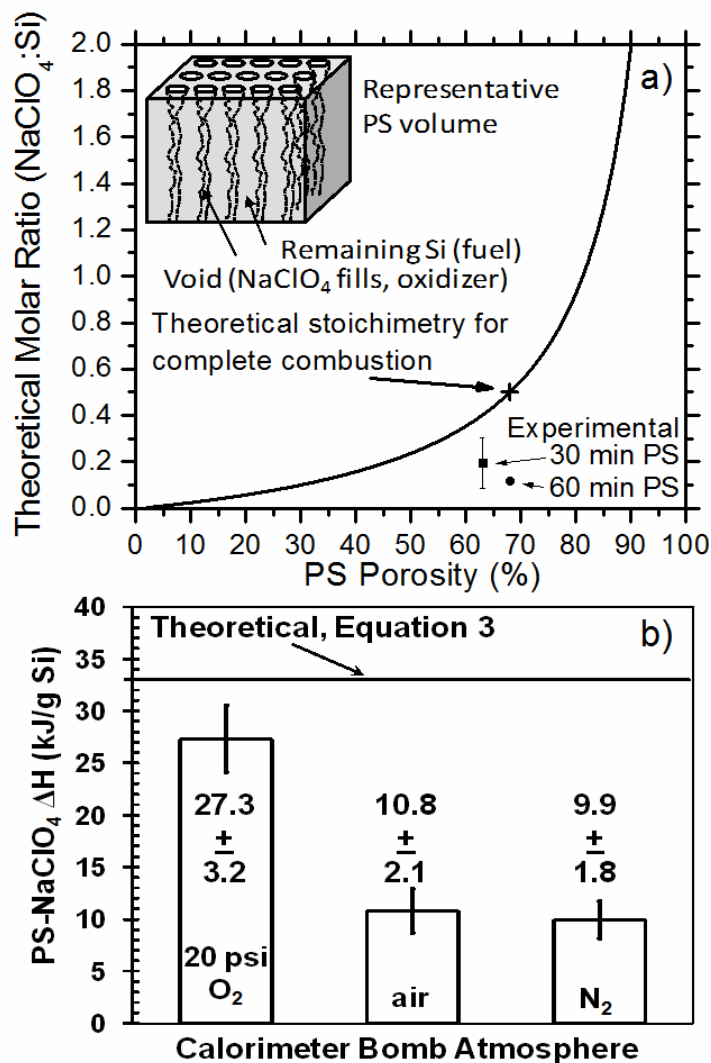


Figure 4.2: (a) The solid line represents the theoretical capacity of PS for NaClO_4 assuming all void space is filled with NaClO_4 . Experimental and theoretical data for the stoichiometry are also shown. Inset: Schematic showing an idealized PS structure filled with oxidizer. (b) Bomb calorimetry results for 30 minute PS. The theoretical heat of reaction corresponding to equation (4.3) is also given. All values are in terms of grams of Si and error bars represent the standard deviation of triplicate measurements.

DSC has been employed in the study of PS and amorphous Si primarily to investigate oxidation and hydrogen desorption [63, 120]. Here DSC is used to provide insight into PS oxidation, hydrogen desorption, and NaClO_4 decomposition in the context of our composite energetic material. Figure 4.3 a shows DSC traces that demonstrate an explosion of PS- NaClO_4 in N_2 (as evidenced by a shattered chip in the high-pressure stainless steel DSC pan) releasing 6.1 ± 0.1 kJ/g of PS and initiating near 133°C . The ΔH determined from DSC may be lower than that of bomb calorimetry due to the nature of the measurement which requires material to be in contact with the bottom of the DSC pan. During an explosion, this is not possible and some heat may be lost to the surroundings of the DSC sample compartment. Additionally, the observed decrease in molar ratio of NaClO_4 to Si in the 60 minute sample would result in a decreased ΔH .

The 30 minute PS sample does not react explosively in the DSC (although it does explode when an intense heat pulse is used as in the bomb calorimetry fuse wire) and does not react until 264°C releasing 1.0 ± 0.1 kJ/g of PS. This oxidation event is likely backbond oxidation of Si [63], and the source of the oxygen must come from partial decomposition of NaClO_4 . While the exact mechanism of decomposition is not known, it is noted that p-type semiconductors facilitate sodium chlorate (NaClO_3) decomposition by accepting an electron, and a similar mechanism may apply here [121]. Additionally, a scan of the 60 minute PS- NaClO_4 is shown after the PS is heat treated in N_2 up to 450°C , and demonstrates that the explosive reaction occurs near 162°C . Figure 4.3 b shows DSC data of NaClO_4 only and the 30 min PS- NaClO_4 . The NaClO_4 has an endothermic peak around 312°C that is associated with the orthorhombic to cubic phase transition and a shoulder near 250°C that coincides with the exothermic peak of the 30 minute PS- NaClO_4 sample [122].

Figure 4.3 c and d show DSC scans of PS powder and PS films on Si substrates without NaClO_4 . The scans are run in either air or N_2 . PS powder was prepared by scraping the PS film from the substrate with a razor blade.

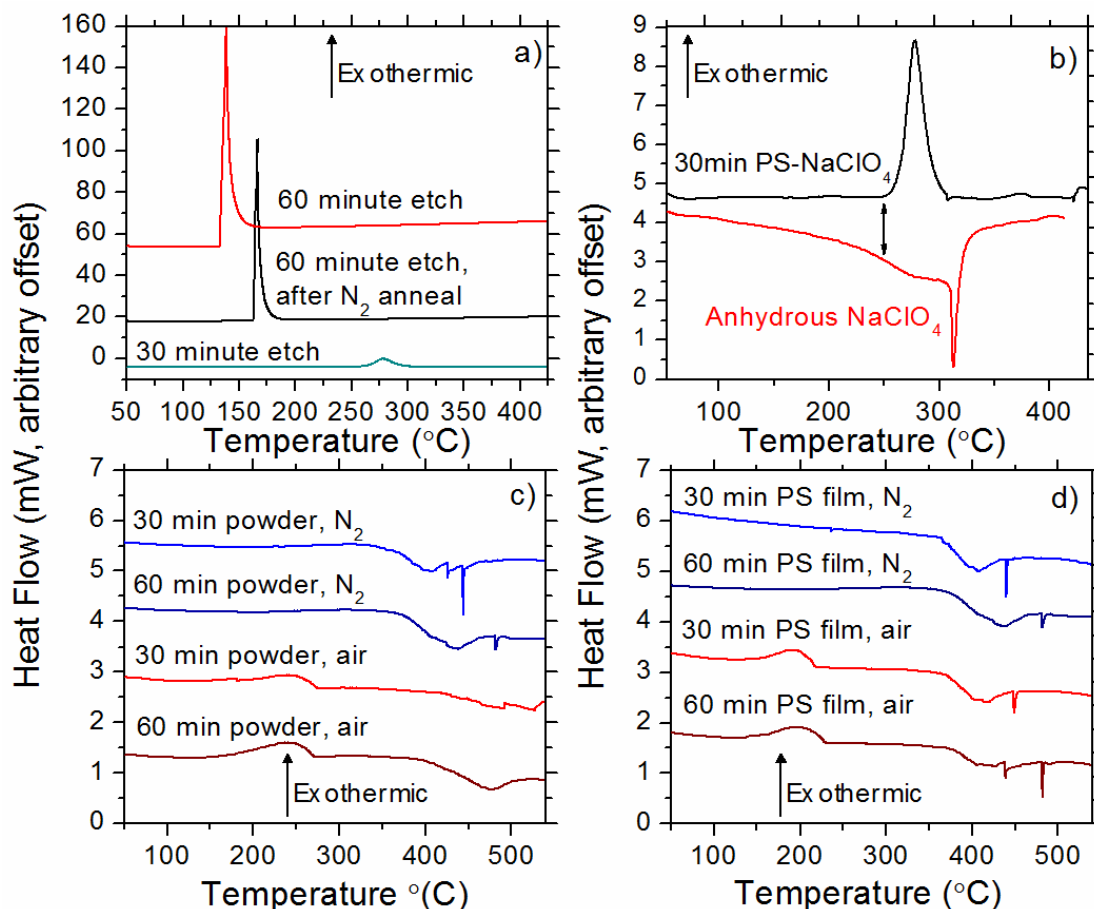


Figure 4.3: DSC scans (of absolute heat flow) of PS- NaClO_4 , NaClO_4 , PS powder, and PS films ($10^\circ\text{C}/\text{min}$) (a) 60 and 30 minute PS- NaClO_4 in N_2 , and 60 minute PS- NaClO_4 after the PS had been subjected to heat treatment up to 450°C in N_2 . (b) NaClO_4 and 30 min PS- NaClO_4 , the arrow indicates the endothermic peak of NaClO_4 initiates at the same temperature as the exothermic peak of PS- NaClO_4 . (c) 60 and 30 minute PS powders in air and N_2 (d) 60 and 30 minute PS films on Si substrate in air and nitrogen.

For a given atmosphere, PS powder and thin films behave very similarly, indicating thickness of the PS film does not hinder its ability to react. Since the first peak is absent in scans in N_2 , this peak is clearly associated with oxidation (most likely backbond oxidation of Si-H_x [63]) and

begins very near where the PS-NaClO₄ explosion begins. The endothermic peaks initiating near 350°C are associated with hydrogen desorption [64, 123]. Scanning the same sample twice results in a flat profile (not shown), indicating that the material has completely reacted during the initial scan.

Dropcasting NaClO₄ in MeOH onto PS results in variation of the NaClO₄:Si ratio as indicated earlier. Additionally, even lower molar ratios are realized by dropcasting a low molarity (0.2 M) NaClO₄-MeOH solution. Figure 4.4 a shows DSC scans of 30 min PS-NaClO₄ to higher temperatures than in Figure 4.3 a. Here the backbond oxidation peak is seen along with the thermal oxidation peak of Si that yields SiO₂[63]. The backbond oxidation peak is similar for 0.303 and 0.122 molar ratios but is reduced by roughly half and shifted to a lower temperature as the molar ratio drops to 0.02. Additionally, a scan of the decomposition of anhydrous NaClO₄ is shown where the endothermic peak near 480 °C represents melting and is followed by an exothermic peak representing decomposition [122, 124]. Figure 4.4 b explicitly shows that thermal oxidation does not occur until after hydrogen desorption. It is also noted that for this oxidation mechanism to progress, NaClO₄ must decompose, and in PS this decomposition actually occurs slightly before the melting point of NaClO₄, indicating the PS serves as a catalyst for NaClO₄ decomposition.

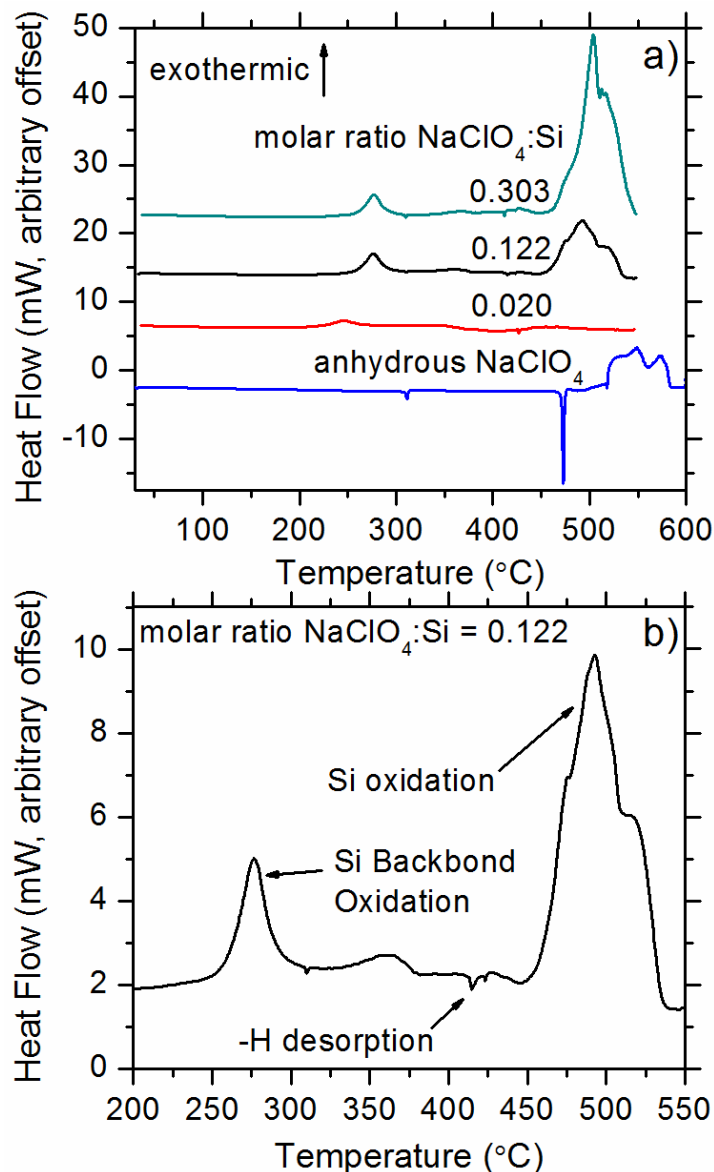


Figure 4.4: DSC scans of 30 minute PS-NaClO₄ and NaClO₄ (10°C/min) (a) Increase of SiO₂ oxidation peak with increasing molar ratio of NaClO₄:Si. Compared to pure NaClO₄, the decomposition of NaClO₄ in PS occurs slightly below the NaClO₄ melting point rather than after the melting point. (b) Enhanced view of the 0.122 molar ratio peak from a) showing the backbond oxidation peak, hydrogen desorption, and Si oxidation.

To verify the DSC results, Fourier transform infrared spectroscopy (FT-IR) was used to evaluate the surface termination of PS as a result of heat treatments and inclusion of NaClO₄.

Figure 4.5 a (30 minute PS) shows that fresh PS and PS that has been dried with NaClO_4 and then rinsed with MeOH to remove the NaClO_4 are nearly identical. Both show very little O-Si-O bond character. This indicates that as a result of the hydrogen termination NaClO_4 does not partially oxidize the PS during drop-casting and therefore does not decrease the amount of available fuel for the reaction. For a heat treatment up to 250°C in dry O_2 , the Si-H_x still remains but O-Si-O has become much more pronounced and a small backbond oxidation peak appears around 2300 cm^{-1} [63]. This confirms the DSC result that the oxidation peak seen with NaClO_4 near 250°C involves backbond oxidation. Additionally, curve 2 shows the 30 minute PS- NaClO_4 after a DSC run to 450°C (below the temperature for complete hydrogen desorption) and exhibits minor contributions of Si-H_x bonding but primarily O-Si-O which gives rise to the exothermic signal in DSC. The peaks near 2345 cm^{-1} and 1626 cm^{-1} correspond to CO_2 and H_2O respectively, where the H_2O likely results from the hygroscopic nature of residual NaClO_4 on the PS surface. Figure 4.5 b (60 minute PS) shows that in N_2 even up to 450°C , the Si-H bond remains as indicated by the peaks near 2100 and 910 cm^{-1} and the shoulder at 660 cm^{-1} on the Si-Si peak at 620 cm^{-1} [123]. The O-Si-O peak does increase somewhat indicating a small amount of O_2 was present during heating. For the heat treatments mentioned in N_2 or O_2 , PS is still capable of explosion by mechanical impact or initiator wire.

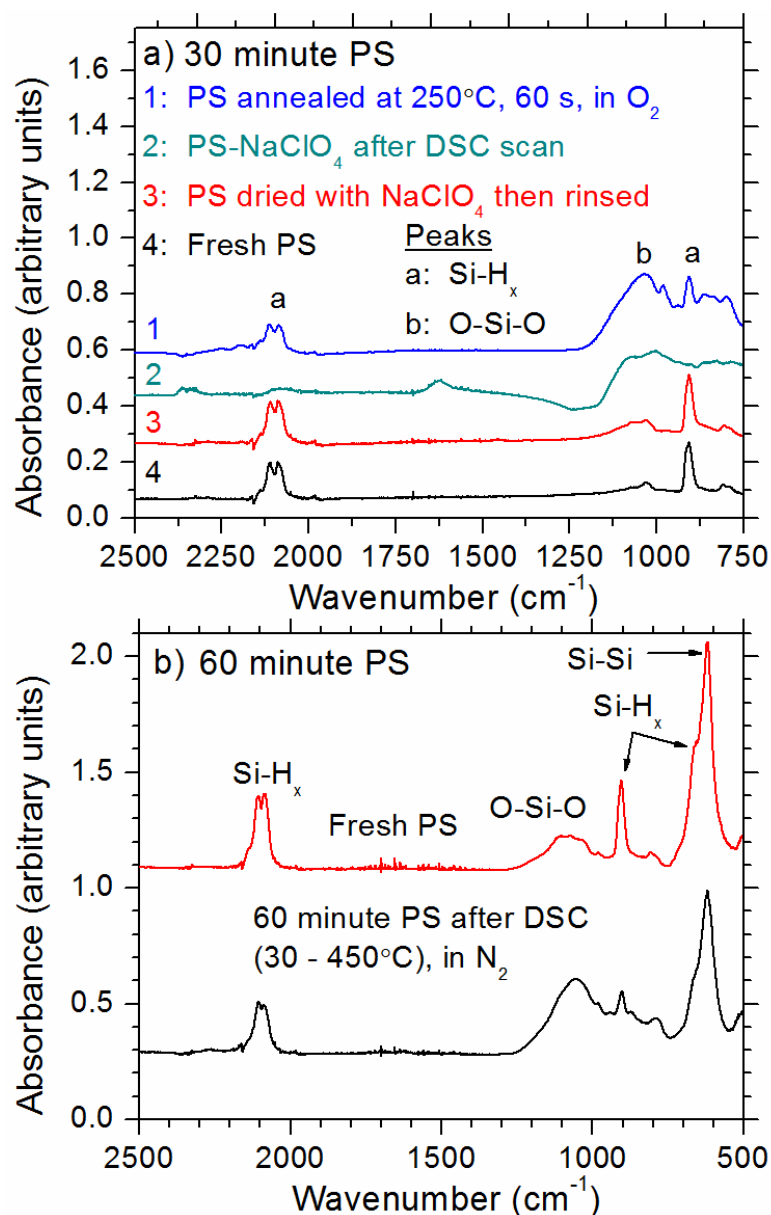


Figure 4.5: (a) Fourier Transform Infrared Spectroscopy (FTIR) of 30 minute PS. Curve 1 shows the PS after a mild anneal of 250°C in O₂ for 60s, curve 2 shows the PS-NaClO₄ after the DSC run, curve 3 shows PS that had NaClO₄ fill the pores but then was rinsed with MeOH, and curve 4 shows fresh PS. (b) FTIR of fresh 60 minute PS and 60 minute PS after a DSC scan from 30-450°C in N₂.

The FT-IR and DSC data suggest that PS-NaClO₄ can only produce an explosion if hydrogen termination is present at the time of initiation. FT-IR reveals that Si-H_x remains up to

450°C, well above the ignition temperature for PS-NaClO₄. Additionally, the O-Si-O bonding does increase after heat treatment of PS in oxygen at 250 °C and DSC reveals that oxidation begins approximately at the same temperature at which the 60 min PS-NaClO₄ ignites. Since the 30 min PS-NaClO₄ remains inert until just above 250 °C, simple oxidation is likely not serving as the ignition source. As suggested by Kovalev et al. [1], one possibility is that the reaction is triggered by exposure of a Si radical as might occur during cracking of the PS structure. Until this crack occurs from thermal stress or mechanical impact, the hydrogen termination prevents Si oxidation. The 60 minute PS structure is more fragile (as evidenced by cracks on the surface after etching) than the 30 minute PS structure and is therefore more susceptible to cracking from thermal stress, which likely explains why only the 60 minute sample explodes during the slow heating rate of the DSC scan. A locally occurring oxidation resulting from Si radical bonds reacting with NaClO₄ produces enough heat to initiate a chain reaction which heats rapidly to remove hydrogen and then oxidizes Si. This result yields H₂ gas that is likely a contributor to the large flames and pressures observed during PS-NaClO₄ explosions.

4.6 Conclusion

In summary, we have used a galvanic corrosion route to PS formation that yields PS layers thicker than 150 μm without the need for a power supply or custom etch cell. We show bomb calorimetry and DSC results of the galvanic PS material reacting with NaClO₄ oxidizer. Gravimetric analysis and bomb calorimetry confirm that the dropcasting of NaClO₄ into PS yields a fuel rich material capable of yielding 9.9 ± 1.8 kJ/g of PS when reacted in N₂. However, this reaction reaches sufficient temperature such that if gaseous O₂ is also present, all of the Si atoms in the PS are oxidized and the theoretical heat of reaction of PS-NaClO₄ is nearly achieved, producing 27.3 ± 3.2 kJ/g of PS. Finally, with DSC and FT-IR analysis, the initiation

temperature of PS-NaClO₄ is found to be as low as 133°C, while Si-H_x bonds on the PS surface are stable up to 450 °C. If hydrogen is desorbed from the PS film, an explosion does not occur despite a large heat of reaction from Si oxidation. If hydrogen is present, and the PS-NaClO₄ is triggered with a rapid heating initiator wire or mechanical impact, the composite reacts explosively. These results highlight the unique role of the hydrogen termination of PS that ultimately facilitates the explosive reaction of PS-NaClO₄.

Chapter 5

Nanometer Amorphous Silica Particles Resulting from the Combustion of Porous Silicon Based Nanoenergetic Composites

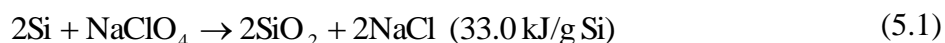
5.1 Preface

The solid products of the reaction of porous silicon (PS) produced with a galvanic corrosion mechanism with sodium perchlorate (NaClO_4) are studied. The reaction products of the PS- NaClO_4 reaction have not been thoroughly investigated, and a prior literature report only observed sodium chloride (NaCl) and NaClO_4 residue. By studying the products, insights into the reaction temperature, pressure, and possible side reactions may be gained. In this study, the composite is ignited in a stainless steel reaction bomb to contain the products which are shown to include a white fluffy powder similar in appearance to amorphous silica. Using scanning electron microscopy, transmission electron microscopy, X-ray diffraction, and Raman spectroscopy, the powder is revealed to be composed of ~50 - 1000 nm spherical particles joined in a chain-like fashion. The particles are amorphous and have a core and surface shell morphology typical of fumed silica. These results give insight into the mechanism of the explosive reaction, with the resulting particle morphology indicative of a very hot reaction ($>\sim 1300^\circ\text{C}$) capable of generating a nanoscale fumed silica product from solid-state reaction precursors.

5.2 Introduction

The oxidation of silicon (Si) is widely studied and holds importance for applications in fields ranging from electronics to biology. The oxidation of porous silicon (PS) is amongst the

most heavily studied aspects of Si oxidation [63, 125], where the large surface area of PS renders the material susceptible to oxidation which alters the optical, electronic, and chemical properties of the overall material [66]. Nanometer scale silica materials, especially fumed silica, have also received a great deal of attention in both fundamental and applied research [126, 127]. Fumed silica is typically produced by combusting silicon tetrachloride in an O₂/H₂ flame to yield a white, powdery solid composed of nanometer scale amorphous silica particles, often linked together forming larger agglomerates [127]. Here we present a solid-state reaction capable of producing fumed silica from a composite of two solid starting reactants, PS and sodium perchlorate (NaClO₄) which react explosively and are thought to follow the reaction presented in equation (5.1).



The term “explosion” here refers to the extremely rapid reaction rate, large heat of reaction[118], loud audible report (~120 dB), and visible flame of the solid-state oxidative reaction. Several groups have reported the explosive oxidation of porous silicon (PS) with strong oxidizers including liquid oxygen, concentrated nitric acid, and solid oxidizer salts [10, 67, 1]. To date, investigation into the mechanism, heat of reaction, and the composition and morphology of products of this reaction remains largely unexplored. Here, the analysis of the silica particles produced from this reaction provides insight into the temperature reached during the reaction as well as the composition of the flame observed during the explosion. We also note that research into the explosive oxidation of PS may provide further insight into the oxidation mechanisms of nanostructured Si under more standard conditions such as heating in air, as well as into the properties of nanoscale silica particles.

McCord et al. [10] reported generation of a white powder from an explosive reaction between PS and concentrated HNO_3 , but did not conduct analysis of this product. The product that results from the PS- NaClO_4 solid-state reaction is likely similar, and here, we use scanning electron microscopy (SEM) and transmission electron microscopy (TEM) to reveal that the powder is composed of polydisperse spherical particles composed primarily of amorphous silicon dioxide (a-SiO_2) with diameters ranging from about 50-1000 nm as revealed by selected area electron diffraction (SAED) and Electron Dispersive X-ray (EDX). The particles are interconnected to form agglomerates and possess a core and surface shell morphology. X-ray diffraction (XRD) and Raman spectroscopy verify the presence of a-SiO_2 and also reveal crystalline Si components likely arising from unreacted Si.

5.3 Sample Preparation

The galvanic etching of PS for nanoenergetics is discussed in prior work[118], and only a brief overview is provided here. For PS formation, double side polished p-type Si wafers of resistivity of 1-30 $\Omega\text{-cm}$ were used. The backside of the wafer is first subjected to a sputter etch to remove the native oxide and is directly sputtered with a Pt thin film of 170 nm without breaking vacuum. The wafer is then annealed at 350°C for 120 seconds to convert the Pt-Si interface to a platinum silicide that enhances electrical connection and drastically improves the adhesion of the Pt film to the Si. Next, the wafer is immersed in an electrolyte composed of a 3:1 by volume solution of 49% HF in water and ethanol (EtOH) respectively with 2.4% by volume composed of 30% H_2O_2 in water. The Pt serves as the cathode and the Si as the anode and an electrical current is autonomously generated to etch the Si to form PS. The thickness, porosity, surface area, and pore size of the film are similar to 60 μm , 63%, and 680 $\text{m}^2 \text{g}^{-1}$, and 2.9 nm respectively. To fabricate the PS- NaClO_4 composite, the PS pores are filled with NaClO_4

by dropcasting a solution of 3.2 M NaClO₄ in methanol onto the PS interface. Enough solution to just cover the entire PS area is used and the solution is allowed to dry for at least 15 minutes in a nitrogen (N₂) filled glove box. The samples (which consist of the PS film on the Si substrate) are then placed in a stainless steel bomb (Parr Instruments, 1109A) and ignited with a nickel-chromium fuse wire. The mass of PS placed in the bomb ranged from about 10-60 mg.

5.4 Results and Discussion

The solid products inside the bomb after the reaction consist of shattered Si substrate and clumps of a white fluffy powder. Figure 5.1 shows an SEM image of the residue with an optical image of the powder in the inset of Figure 5.1 (a), and a TEM image of the residue from the galvanic PS-NaClO₄, Figure 5.1n(b). The particles in Figure 5.1 (a) are typically much less than 1 μm in diameter, with sizes as small as 50 nm.

Figure 5.2 shows higher magnification TEM images of the powder product seen in Figure 5.1. As seen in Figure 5.2 (a), some particles are joined to neighboring particles, and additionally, a long neck connecting two particles is seen in Figure 5.2 (b). This characteristic is typical of fumed silica where particles are noted to interconnect to form chains and agglomerates[126, 128]. Figure 5.2 (b) also resolves the core and surface shell structure of the particles, which is visible as an ultra-thin layer (indicated by arrows) that encapsulates the larger spherical particles. The thickness of this surface shell is estimated to be $\sim 1\text{nm}$ and appears to be of similar thickness regardless of particle size. A representative Selected Area Electron Diffraction (SAED) pattern of the powder product, shown in Figure 5.2 (c), indicates primarily amorphous character. Furthermore, EDX analysis shows 31% Si and 69% O in the powder product, indicating a nearly perfect SiO₂ stoichiometry without Na or Cl impurities.

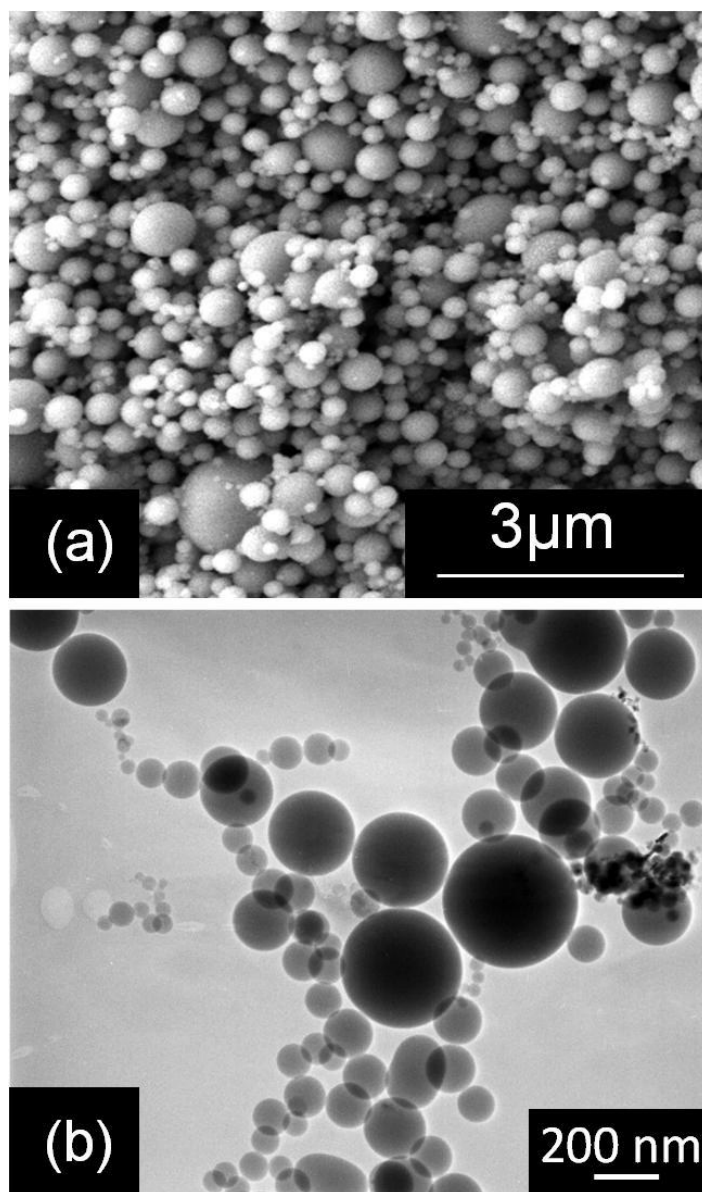


Figure 5.1: SEM, with optical inset, (a) and TEM (b) images of the powder residue from the PS- NaClO_4 composite.

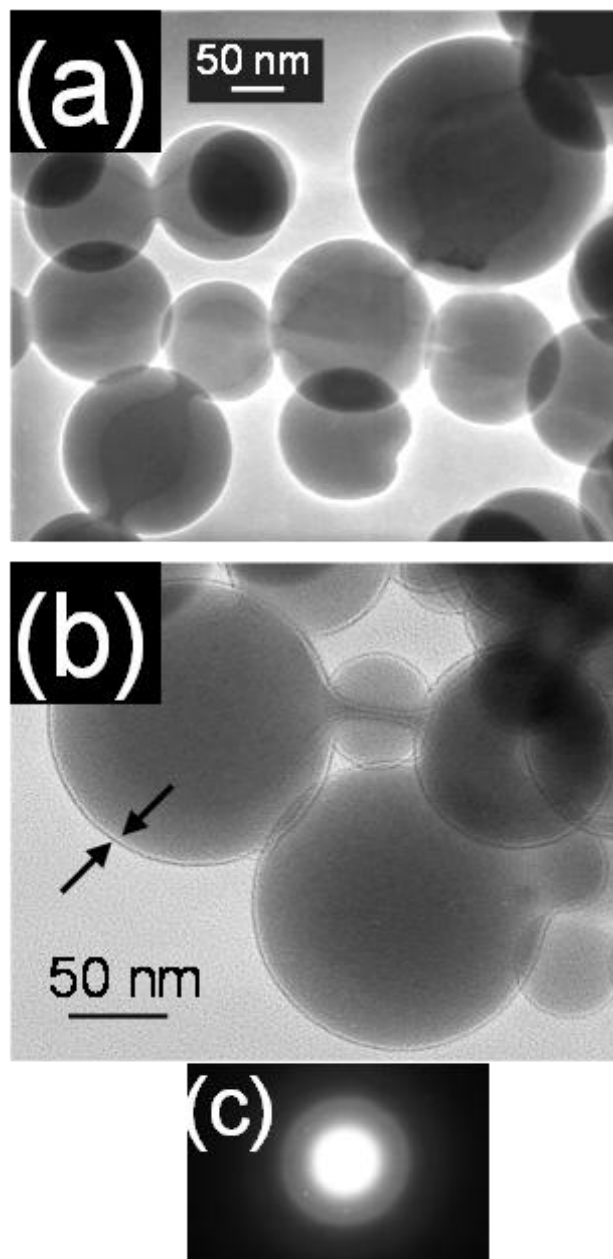


Figure 5.2: TEM images of the powder residue from (a) and (b) PS-NaClO₄ and (c) a representative SAED pattern.

To eliminate possible contamination of the powder product from small pieces of shattered Si substrate (i.e., remnants of the shattered Si substrate can mix with the white powder and give spurious Si signals in the Raman and XRD analyses), PS films were scraped from the Si substrate to create a PS powder that was subsequently mixed with NaClO₄ and then ignited in the

steel reaction bomb. The powder mixture is brown prior to combustion, and is converted to a white powder after combustion that is similar to that seen with the PS- NaClO_4 composite combustion product in Figure 5.1 and Figure 5.2. A TEM image and SAED pattern in Figure 5.3 (a) of the PS powder prior to combustion shows primary particles of crystalline Si ranging in size from several hundred nm to over 1 μm . XRD spectra taken of the powder mixture pre- and post-combustion are shown in Figure 5.3 (b).

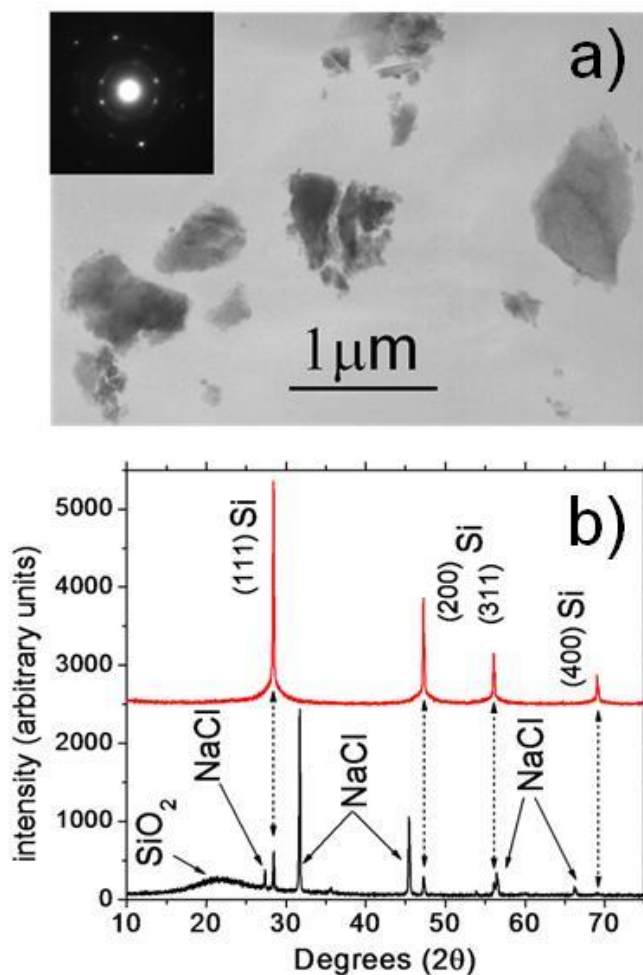


Figure 5.3: a) TEM of PS powder prior to combustion with SAED pattern inset. b) XRD spectra of PS- NaClO_4 mixture prior to combustion (top, red) and after combustion (bottom, black).

Prior to combustion, the XRD peaks have a broad base that tapers to a sharp peak, similar to spectra reported previously for PS[129, 13]. Using a Scherrer analysis, the size of the

domains for the (111) sharp peak and broad base are 120 and 6 nm, respectively. After the detonation, only one size domain of 120 nm is present which likely arises from traces of unreacted Si in the XRD sample. In addition, an amorphous region centered near $21^\circ 2\theta$ indicates amorphous SiO_2 as previously observed in XRD by Cisneros et al. after heating PS in O_2 from 300-700°C[66]. In addition to the amorphous SiO_2 , Cisneros et al. also observed amorphous Si while heating from 300-700°C, however both the amorphous Si and SiO_2 contributions vanished as crystalline SiO_2 appeared upon heating to 900°C. Some caution should be used in comparing results as we note those experiments were conducted on lower surface area PS ($\sim 284 \text{ m}^2/\text{g}$) with larger pores (5.3 nm), thus resulting in larger crystalline domains as compared to the samples here. However, no amorphous Si or crystalline SiO_2 was observed in our samples by Raman spectroscopic and XRD analyses, respectively, which indicates that the PS- NaClO_4 reaction is fundamentally different from the rather slow oxidation of PS in an O_2 atmosphere.

Raman spectra, shown in Figure 5.4, of PS pre- and PS- NaClO_4 post-combustion, were obtained with a 514 nm laser from a Renishaw InVia microscope. The post-combustion spectrum shows a large, broad peak at 445 cm^{-1} and two smaller, sharp peaks at 489 cm^{-1} and 604 cm^{-1} , a peak pattern characteristic of fumed silica [127, 130]. The peak at 489 cm^{-1} is indicative of ring structures in the amorphous SiO_2 network, and the slight increase in intensity relative to the peak at 445 cm^{-1} is indicative of nanostructured fumed silica[131]. In both spectra, a sharp peak at 519 cm^{-1} results from single crystal Si, again indicating some unreacted Si in the product.

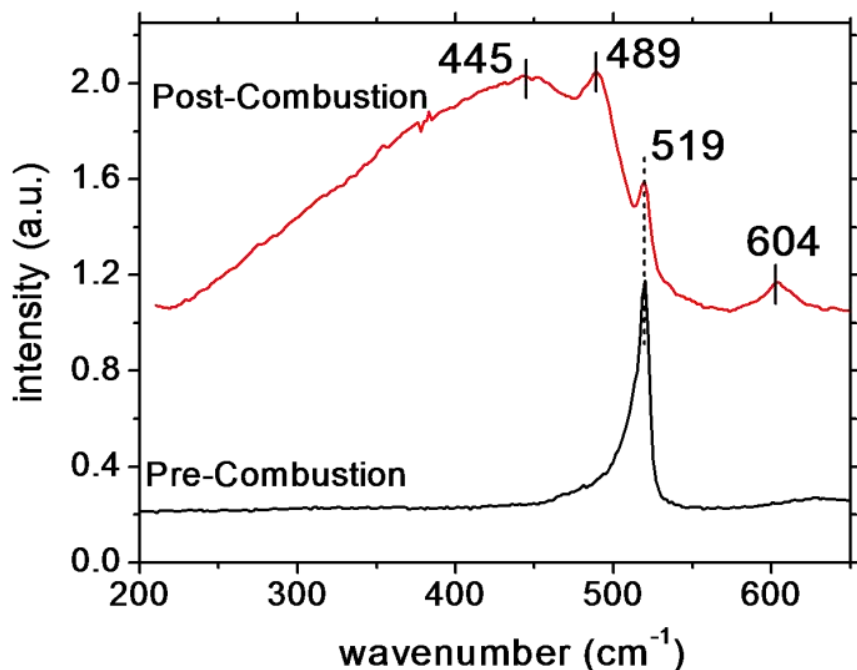


Figure 5.4: Raman spectra of PS pre- and PS- NaClO_4 post-combustion.

The solid-state reaction products here are composed of nanoscale amorphous silica particles, often interconnected, that constitute a fumed silica product. However, fumed silica is typically produced by the pyrolysis of silicon tetrachloride in an O_2/H_2 flame, forming small SiO_2 clusters that aggregate into larger primary particles[127]. In this study, the Si starting material is a solid but during the violent oxidation an intense flame is visible as shown in Figure 5.5 when a ~ 2 cm by 2 cm PS strip is ignited in an acrylic box under flowing nitrogen (the nitrogen purges the box of any water vapor as the NaClO_4 is very hygroscopic). The times indicated in Figure 5.5 a) and b) are taken from the time of the first visible light from the explosion and are recorded by a Phantom V. 9.1 (Vision Research) high speed camera at 6,400 frames per second with a $2 \mu\text{s}$ exposure time. Visible light from the flame persists for $1250 \mu\text{s}$, however, owing to the very short exposure time, the flame may be present for even longer but is not resolved by the camera.

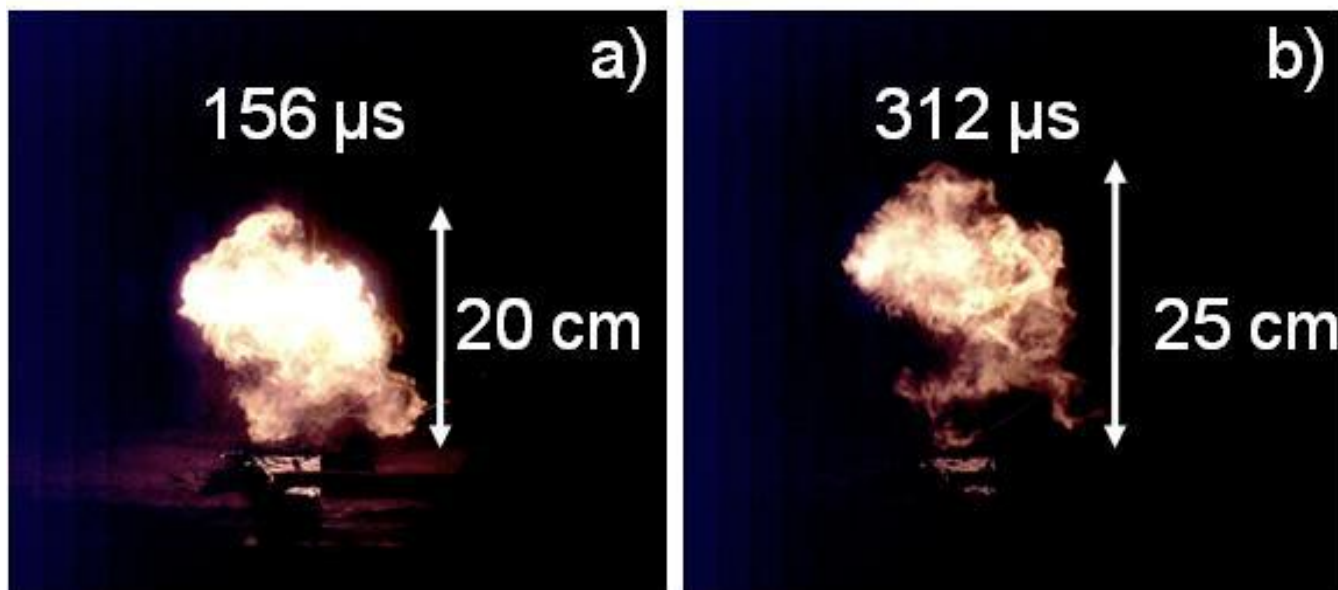


Figure 5.5: High speed video of a PS-NaClO₄ sample ignited in an acrylic dry box showing the flame from the reaction at 156 μ s (a) and 312 μ s (b) from the time of the first visible light from the explosion.

During the explosion that results from reacting PS with liquid O₂, Kovalev et al.[1] recorded an optical spectrum showing plasma lines related to atomic oxygen and ionized Si but did not have direct measurements of the reaction temperature. Additionally, prior work has noted that sintering necks in silica particles, as observed in Figure 5.2, were present only after temperatures exceeded 1300°C[126]. Therefore, while not direct evidence of the solid-state PS-NaClO₄ reaction temperature, the sintering observed here indicates that the reaction temperature may be quite high. This is an important finding, as a previous study measured the temperature of gases in the PS-NaClO₄ reaction to be near 460°C, but was unable to measure the surface temperature of the PS film during the reaction[132]. The results presented here thus suggest that PS network may actually be broken into small Si clusters that are then oxidized at high temperature, near 1300°C. These clusters coalesce into primary particles of amorphous silica. The rapid cooling experienced in the reaction facilitates formation of amorphous silica rather

than production of the crystalline silica, cristobalite [133]. Additionally, as seen in Figure 5.2 (b), a core and surface shell structure clearly exists with a shell thickness similar to that reported by Vaccaro et al.[127] for fumed silica.

5.5 Conclusion

In summary we have analyzed the solid products of the reaction of PS with NaClO_4 . The white, fluffy powder product, characteristic of amorphous silica, is found to be composed of particles, often interconnected, of a nearly perfect spherical shape with polydisperse sizes ranging from just under 50 nm to upwards of 1000 nm. The morphology and chemical composition of the product indicates that small clusters of SiO_2 are formed during combustion that coalesce to form larger particles. Particles are observed to have a core and surface shell structure similar to fumed silica particles produced by gas-phase pyrolysis. Based on the sintering observed in the particles and the structural analysis findings here, the highly exothermic reaction of PS with NaClO_4 likely reaches temperatures near 1300 °C, forming a nanoscale fumed silica product.

Chapter 6

Galvanic Porous Silicon Composites for High Velocity Nanoenergetics

6.1 Preface

Porous silicon (PS) films ~65-95 μm thick composed of pores with diameters less than 3 nm are fabricated using a galvanic corrosion etching mechanism that does not require an external power supply. A highly reactive nanoenergetic composite is created by impregnating the pores with the strong oxidizer, sodium perchlorate (NaClO_4). The combustion propagation velocity of the energetic is measured with a novel on-chip diagnostic and high-speed imagery up to 930,000 frames per second. Combustion velocity averaging 3,050 m/s is observed for PS with specific area ~840 m^2/g and porosity 65-67%.

6.2 Introduction

Porous silicon (PS) is a widely studied material with applications for fuel cells, [16, 17] solar cells, [134] and biology [135]. The large specific surface area resulting from the nanometer scale pores within the PS structure yields a highly reactive material that is especially susceptible to oxidation [118]. In addition to thermal oxidation in air and O_2 , it is known that PS is capable of rapid oxidation and possible explosion with liquid O_2 , [1] nitric acid, [10] sulfur, [68] and strong oxidizing salts [67]. This capability places PS alongside other nanoenergetic material systems [46, 50, 53] where the small scale of the Si crystallite domains and large surface areas allow for an oxidation reaction that proceeds through the material at velocities (i.e. the flame propagation velocity) in the km/s range [1]. Recently, nanoenergetic materials have received attention for their rapid energy release rates, [136, 137] their use as additives in conventional

energetic materials, [138] and their possible use in Microsystems based applications [69]. A prior report testing nanoscale aluminum and bismuth trioxide noted the highest velocity of any nanothermite with combustion velocities up to ~ 2500 m/s [139]. In this work, we improve upon this velocity and measure a flame propagation rate of ~ 3050 m/s for a PS-sodium perchlorate (PS- NaClO_4) composite having 2.4-2.5 nm pores.

One significant advantage of PS over other nanothermite materials composed of mixtures of fuel and oxidizer powders is its monolithic integration with a Si substrate, therefore making it compatible with Microsystems processing techniques. However, the conventional formation of PS requires the etching of Si with a hydrofluoric acid (HF) based electrolyte in a custom Teflon etch cell using an external power supply, an approach not well-suited for batch processing. Here we present a galvanic etching technique for formation of PS films that does not require a custom etch cell or an external power supply. This method has previously been reported [35, 118, 34], but we demonstrate significant improvements to the technique and produce Microsystems with integrated PS films having superior properties for nanoenergetics when PS is reacted with sodium perchlorate (NaClO_4). We also show the flexibility of the technique by using an on-chip method [140, 118] for determination of the flame velocity of the reaction that agrees well with high speed video taken of the reaction. The development of an on-chip diagnostic device for velocity measurement provides a complimentary measurement to high speed video analysis.

6.3 Results and Discussion

Here, we pattern resistive wires across a strip of PS such that a voltage placed across the wire is used to monitor the progression of the energetic reaction between PS and NaClO_4 . Figure 6.1 a) shows a typical PS layer integrated with resistive wires for velocity testing. The fabrication is similar to our previous report for PS energetic integration with Microsystems [69]

and a detailed process flow figure is presented in Appendix B. Briefly, we begin with a 1-20 Ω -cm Si wafer that has 600 nm of low-stress LPCVD Si_3N_4 to serve as an etch mask. A reactive ion etch removes a section of Si_3N_4 to expose Si where PS will be formed. Each gold (Au) resistive wire in Figure 6.1 a) is patterned on top of a Si_3N_4 /chrome (Cr)/platinum (Pt) stack where the Si_3N_4 prevents delamination during PS formation and the Cr/Pt serves as an adhesion layer for the Au. The wire on the far left of the diagnostic device in Figure 6.1 a) functions as the igniter for the PS- NaClO_4 reaction and tapers to a 25 μm wide strip where 3 μm of Cr, Pt, Au stack overhangs each side of the 19 μm wide Si_3N_4 to be in direct contact with the Si. Figure 6.1 b) shows an optical image of the igniter wire. The remaining wires are similar to the igniter, however they taper to a 50 μm wide strip and the Cr, Pt, Au stack does not overhang the Si_3N_4 . The wires in Figure 6.1 a) are spaced 5 mm apart, but devices were also made with 2.5 mm and 10 mm spacing for each of the 7 wires and one igniter on the chip. The length of the chips thus ranges from 1.75 cm to 7 cm.

These wires serve as resistors that can be monitored by a high speed oscilloscope during the explosive reaction. A deviation in the applied voltage across a wire indicates the time at which the flame front of the reaction passed. In Figure 6.2 a), an optical image of a representative diagnostic device prior to combustion is shown, including scale bars that indicate length of the PS strip from the igniter to the last resistive wire and the approximate height of the image. A single frame from a high speed video taken at 65,100 frames per second shows, in Figure 6.2 b), a flame propagating across the length of the chip upon ignition of the PS- NaClO_4 composite layer. The time stamp in Figure 6.2 b) is the elapsed time of the video. As Figure 6.2 c) clearly shows, the Au wires across the PS strip are completely removed by the explosive reaction when it passes.

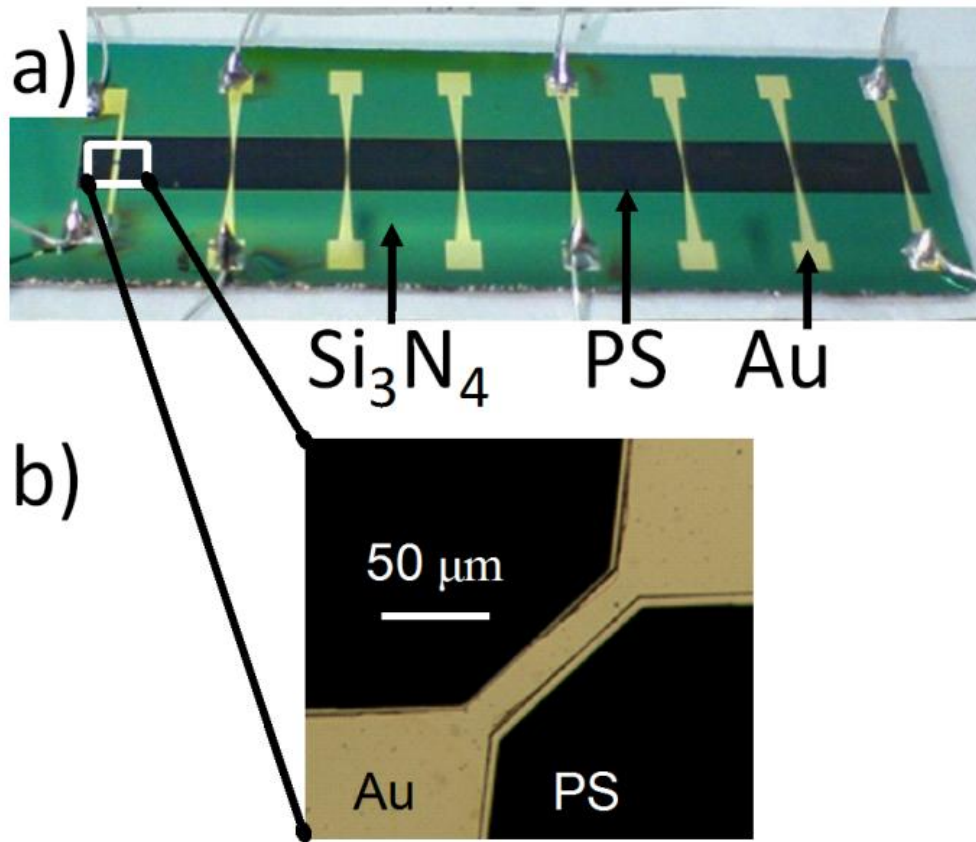


Figure 6.1: a) An optical image of the microfabricated velocity diagnostic device with integrated Au wire resistors spaced 5mm apart for velocity measurement along the length of the PS- NaClO_4 composite layer, and b) a close-up optical image of the Au igniter wire.

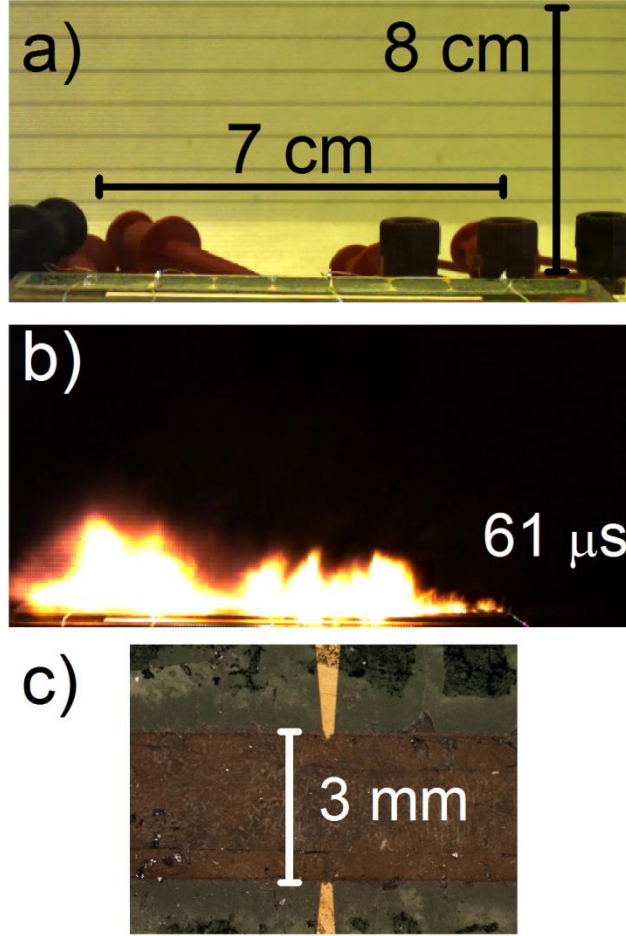


Figure 6.2: Images in profile of the on-chip velocity diagnostic device a) prior to ignition and b) 61 μs after ignition. The high speed camera captures the nearly 4 cm high flame as it propagates down the length of the device during PS- NaClO_4 combustion. c) Top-view of a remnant of a single velocity wire after the combustion reaction.

For on-chip PS formation, a sputtered 170 nm thick Pt layer on the backside of the chip serves as the cathode during galvanic etching. Upon immersing the entire lithographically patterned device in HF based electrolyte, the oxidizing agent (H_2O_2) [32] is reduced at the backside Pt cathode according to equation (6.1) and holes are injected into the Si substrate, as illustrated in Figure 6.3 a) [141].



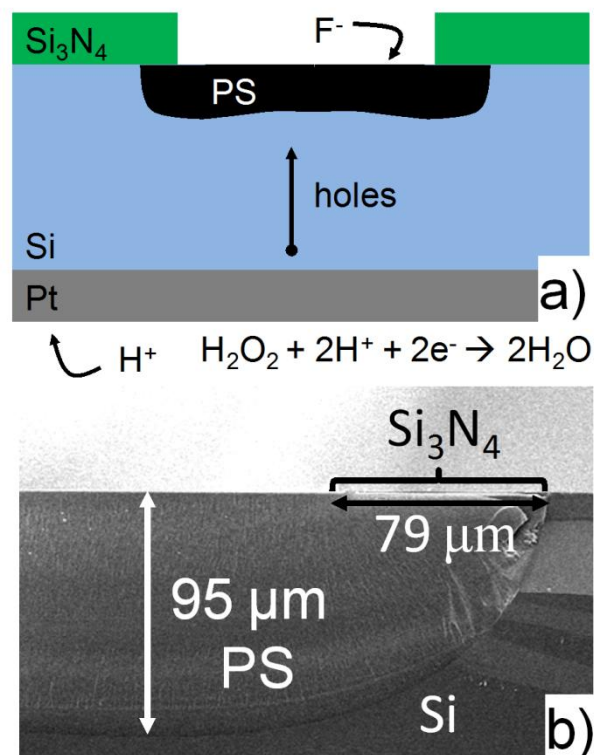


Figure 6.3: a) Illustration of the galvanic etching mechanism used for on-chip PS formation. b) SEM cross section of the 20:1 galvanic PS layer bordering the Si₃N₄ mask.

The circuit is completed as F⁻ oxidizes Si at the anode and H⁺ migrates to the cathode, where H⁺ and F⁻ arise from HF. The galvanic current is limited by the ratio of the cathode to anode surface areas and may be impacted by the electrode geometries which modify the etch rate and uniformity [31]. The surface area ratio (SAR) of Pt to Si used here is approximately 5 and the exposed Si on the top of the substrate is centered with respect to the backside Pt layer. The etch rate is approximately 4.5 times higher than our previous work using a 1:1 SAR [118]. With the conditions applied here, the etch depth typically fluctuates within 10 μm from sample to sample.

In order to fabricate PS with dramatically different porosities but similar thicknesses, surface areas, and pore sizes, as given in Table 6.1, two electrolyte compositions of 3:1 and 20:1 (vol:vol) of 49% HF in water and ethanol are used. The ethanol acts as a surfactant that enables

wetting of the Si during etching. Information in Appendix B provides further details on the BET [111, 118] method used for determination of the PS pore size and surface area, as well as the gravimetric technique used for porosity measurement.

Table 6.1: PS properties for 3:1 and 20:1 PS.

Electrolyte (HF:EtOH)	Thickness (μm)	Pore Size (nm)	Porosity (%)	Surface Area (m^2/g)
20:1	~65-95	2.4-2.5	65-67	830-850
3:1	~65-95	2.8-2.9	79-83	890-910

In both cases, 2.4% by volume of the etching solution is composed of 30% hydrogen peroxide (H_2O_2) in water. The solutions are mildly stirred with a magnetic stir bar and a 10 minute etch time is used. As the scanning electron microscope (SEM) image in Figure 6.3 b) shows, undercutting of the Si_3N_4 mask does occur as previously reported for both electrochemical and galvanic corrosion [35]. While the image in Figure 6.3 b) results from a 20:1 PS specimen, the PS thickness is similar for the 3:1 PS specimen as is expected since etch rate is primarily a function of H_2O_2 concentration and the ratio of exposed platinum to exposed silicon, and independent of HF concentration [34]. However, the use of higher HF concentrations leads to a decrease in both porosity and pore size.

An electrical schematic of the velocity measurement test setup is shown in Figure 6.4. Wire leads are soldered to the Au bond pads on the chip and connected to voltage supplies and resistors for velocity analysis. Once all the electrical leads are connected, the PS- NaClO_4 nanoenergetic composite is formed by dropcasting a 3.2M solution of NaClO_4 in methanol (MeOH) on the chip while inside an acrylic N_2 desiccator box under a constant N_2 purge to maintain relative humidity $< 2\%$ and to prevent the highly hygroscopic NaClO_4 from absorbing moisture. This procedure impregnates the pores with NaClO_4 , although most likely they are most likely not completely filled with NaClO_4 as our prior work indicates [118]. The chip is

allowed to dry for at least 20 minutes prior to testing. For consistent ignition, 27 V from a battery was applied across the igniter wire, which had a resistance near 3Ω . The wire heats when the voltage is applied and initiates the reaction. Prior to ignition, 27 V is also applied across select Au resistor wires on the chip, and this voltage is monitored (with voltage probes across each $100\text{ k}\Omega$ resistor) by a Tektronix DPO 3054 oscilloscope sampling at 10^8 samples per second. The $100\text{ k}\Omega$ resistors in series with the 27 V prevent significant current from flowing that might ignite the sample at these wires. In addition to the oscilloscope, the reaction is monitored by a Photron Fastcam SA5 high speed video camera. The camera and oscilloscope are triggered to record data simultaneously by the 27 V battery applied across the igniter wire. From high speed video analysis, ignition occurs typically within 1-10 μs of the trigger but has been observed to occur after several hundred microseconds. Seven wires are patterned on the chip in the event that a wire fails during metal wire deposition or etching.

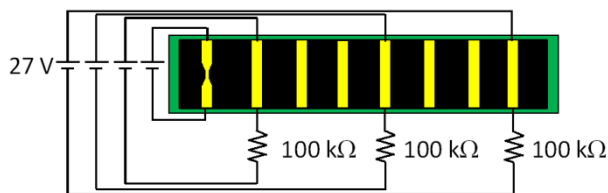


Figure 6.4: Electrical schematic of the on-chip velocity diagnostic device.

Figure 6.5 a) shows a velocity analysis composed of an oscilloscope readout and high speed camera images taken at 930,000 frames/s in a) and b), respectively, from a 20:1 nanoenergetic PS specimen. The uppermost image in Figure 6.5 b) is a top-view optical image used to reference the position of the flame front on the chip. The time stamps on the left of Figure 6.5 b) indicate the elapsed time from the triggering signal. The velocities listed on the right side of the figure are computed as the distance to the flame front measured from the first

visible flame front at 11.8 μs divided by the elapsed time from 11.8 μs . This method is used because, as the white circles indicate in Figure 6.5 b), gaps in the flame exist so measuring the velocity as the distance and time from the previous frame may lead to extremely large velocities approaching 7000 m/s, which are not believed to be accurate. The gaps may occur if there is a shock wave that travels either through the PS or Si substrate that ignites the sample ahead of the flame, or if a flame of weak visible intensity is present but not resolved optically by the camera. As determined from the high speed camera analysis, this representative specimen shown in Figure 6.5 displays an average velocity of 3,140 m/s from start to finish, and initiates near 1700 m/s. In Figure 6.5 a), wires 2, 4, and 7 were monitored with a spacing between each wire of 5 mm.

The dotted lines in Figure 6.5 a) indicate the time that a voltage drop in the wire occurs. Wires 2 and 7 show gradual negative slopes in the voltage prior to the sharp downward spike. We have observed this effect on multiple samples and believe it is the result of initial heating or partial damage to the wire before the wire is completely destroyed. The image at 15.1 μs shows that the leading flame is very near the wire, while at 16.1 μs , the white circle indicates a small flame now well past the wire. Therefore, the oscilloscope reading of 15.5 μs for the initial decrease in voltage aligns well with the high speed camera images. The measured velocity from wires 2 to 7 using the oscilloscope data is 3170 m/s. Between wire 2 and 4 the velocity is 3220 m/s and between wire 4 and 7 the velocity is 3140 m/s.

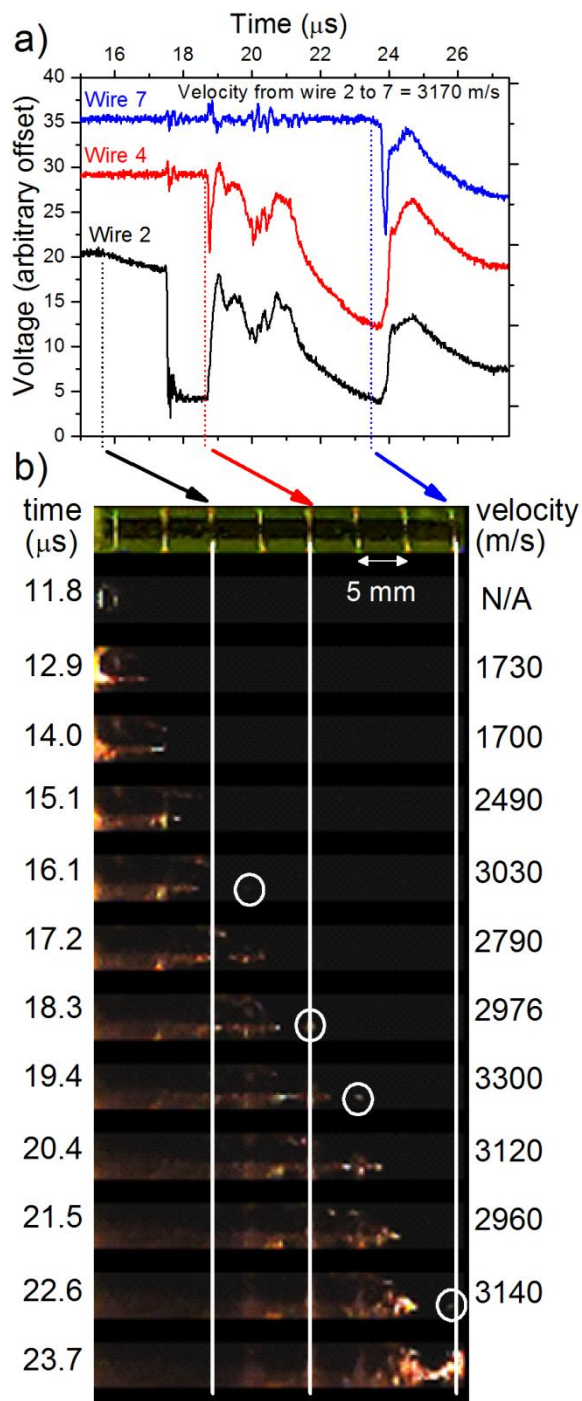


Figure 6.5: Velocity analysis of the PS-NaClO₄ reaction (20:1 PS). a) Voltage output from the on-chip velocity test with the dotted lines indicating the time at which the voltage drops. b) Selected frames from high speed video analysis of the reaction (930,000 frames/s) with the image time stamps on the left measured from the time of the sample trigger and the velocity (as measured from the position of the flame at 11.8 μs) on the right.

The electrical noise seen in Figure 6.5 a) is observed even after the flame passes the wire. This is consistently observed in all samples and the voltage generally does not fall to zero until one or two milliseconds after the trigger. High resolution images similar to Figure 6.2 b) show a flame that persists for several hundred microseconds and is likely composed of ionized Si, atomic oxygen, and sodium [132, 1]. The flame is visible on the order of the time scale that spurious electrical events are noted in the oscilloscope traces. Since the voltage profiles of individual wires are often identical as in wires 2 and 4 between 19 and 21 μs in Figure 6.5 b), a conductive flame may be responsible for the noise and is capable of completing the electrical circuit even after the wires are destroyed.

The average reaction rates observed here are greater than 3000 m/s for the 20:1 PS specimens and are dramatically faster than previously observed [119]. Table 6.2 provides the average and maximum velocities measured for the 3:1 and 20:1 galvanic PS. The average velocity from the beginning to the end of the chip for at least three different PS- NaClO_4 measurements is reported from high speed video and oscilloscope data. A further discussion of the velocity measurement details is provided in Appendix B.

Table 6.2: Flame propagation velocities for 3:1 and 20:1 PS.

Electrolyte (HF:EtOH)	H.S. Video Velocity (Avg, +/-)	Oscilloscope Velocity (Avg, +/-)
20:1	3050, 230	3100, 230
3:1	2170, 120	2150, 200

The reaction mechanism of PS- NaClO_4 is likely dependent on the exposed surface area of hydrogen terminated Si [1]. The 20:1 and 3:1 PS specimens both have surface areas approaching the maximum measured for PS, but the 20:1 has a lower porosity and smaller pores than the 3:1 PS samples. A decrease in porosity may raise the velocity, as Fan et al. [142] have reported a dependence on porosity of the speed of sound in PS. Thus, if an acoustic or a

supersonic shock wave helps to drive the reaction, it will travel faster in lower porosity PS. Additionally, the thermal conductivity will be higher and thermal energy will conduct faster. Furthermore, an ideal oxidizer:fuel (NaClO_4 :PS) ratio of 0.5 is met with the 65-67% porosity of the 20:1 sample, whereas the 3:1 sample with 79-83% porosity accommodates excess NaClO_4 and will yield an over-oxidized sample as discussed in our prior work [118]. Excess oxidizer adds thermal mass to the system that is not necessary for combustion and likely slows the reaction.

6.4 Conclusion

In summary, we have used a galvanic etching approach to fabricate PS without the need of a power supply or custom etch cell. This method allows for batch fabrication of PS with pore sizes ranging from 2.4-2.9 nm. Through conventional Microsystems lithography, galvanic PS is integrated with resistor wires that enable an on-chip flame propagation rate measurement of PS- NaClO_4 combustion. High speed video analysis confirms that the on-chip technique can be used to determine the reaction velocity. The average velocity of PS- NaClO_4 was 2170 and 3050 m/s for PS with surface areas of $\sim 900 \text{ m}^2/\text{g}$ and $\sim 840 \text{ m}^2/\text{g}$, respectively, and porosities of 79-83 % and 65-67 %, respectively. We attributed the increased reaction velocity of the lower porosity PS to a combination of the nearly ideal oxidizer:fuel ratio and an increased speed of sound in the PS relative to the higher porosity counterpart.

Chapter 7

Conclusions and Future Directions

7.1 Conclusions

The work in this thesis is presented from a materials science point of view. The goal of the thesis was to process silicon (Si) to generate a nanoscale porous silicon (PS) material. This processing can be considered a synthesis technique for a nanoscale Si product. Many properties of Si are altered as the Si is scaled to the nano- from the bulk scale, but here the emphasis was placed on the reactivity of Si, specifically oxidation at the nanoscale. In addition to fundamental studies of the material using thermal analysis, spectroscopy, and electron microscopy, the material was integrated into a simple, on-chip device which allowed further study of reactivity. The information presented in this thesis provides a solid foundation for future research into targeted applications of nanoenergetic PS or use of oxidizers other than sodium perchlorate.

In Chapter 2, a finite element method (FEM) model to predict galvanic corrosion on small scale Si devices is presented. Additionally, focused ion beam (FIB) is used to analyze devices in cross section to visually inspect the uniformity of the galvanic corrosion across the device. Prior work had assumed corrosion was uniform across the device, but from both modeling and FIB results, this is not the case. For small scale devices if a surfactant is used, the corrosion will be uniform at micron scale distances but uniformity is not expected as the device approaches the centimeter scale. The work in this chapter is significant as studies in the literature had examined the effects of galvanic corrosion on small scale devices but had not considered geometrical effects on corrosion. This study was also the first to investigate PS thickness formed from a galvanic technique in which the cathode is placed on the topside of the

Si wafer rather than on the underside. In general previous studies of MEMS galvanic corrosion during processing treated corrosion as an unwanted effect that should simply be avoided by MEMS engineers. However, the results in Chapter 2 help to set the stage for designers who may want PS in devices for applications in fields such as fuel cells, batteries, or nanoenergetics. The chapter highlights some considerations designers must be aware of in targeting PS growth on a device.

The work in Chapter 3 presents the analysis of the effects of varying processing conditions on PS growth by both galvanic and electrochemical methods. A detailed characterization of galvanic PS by gas adsorption measurements and cross-section SEM is presented. Pore sizes, etch rates, and porosity had previously not been reported for galvanic PS formed on lightly doped PS. Extremely high specific surface area $> 800 \text{ m}^2/\text{g}$ PS is fabricated using a very high ratio of HF to EtOH of 20:1. A discussion of annealing Pt on Si to form a strong adhesion with Si is presented and is critical to etching in high ratios of HF:EtOH. Further studies in the chapter use Raman spectroscopy and TEM to investigate the microstructure of selected galvanic PS. Similar to electrochemical PS, amorphous Si is not found, however misalignment of Si crystallites is observed. This chapter explicitly outlines testing methods used for galvanic PS evaluation and these methods are critical for the evaluation of the material for nanoenergetics in subsequent chapters.

Chapter 4 presents the first thermal analysis to the author's knowledge of nanoenergetic PS- NaClO_4 energetic composites. A bomb calorimetry analysis reveals that the addition of O_2 to the bomb atmosphere leads to a dramatic increase in the heat of reaction. This indicates that during the explosive reaction, unreacted material is present and the heat evolved is sufficient to enable a complete reaction of the material with available gaseous oxygen. With the added

oxygen, the heat of reaction approaches the theoretical maximum. A differential scanning calorimetry (DSC) analysis is also performed and reveals that hydrogen termination of PS is necessary for a violent explosive reaction to occur. The ignition temperature is also seen to be as low as 133°C. The results confirm that the reaction is initiated by a locally occurring oxidation of Si radicals that then propagates through the material as presented theoretically by prior work [1]. The chapter also investigates the effect of decreasing the oxidizer:fuel ratio. This is the first approach where the oxidizer:fuel ratio has been analyzed for PS- NaClO_4 in a DSC instrument. A decrease in the heat of reaction of PS oxidation is observed. This work is relevant to PS nanoenergetics as it demonstrates the first quantitative information available about the heat of reaction for the system. PS is challenging to work with because much of its characterization is destructive (i.e. measuring thickness, mass, and porosity all require damaging the sample) but attaining quantitative data about the explosive reaction is critical to future development of the material.

Results of Chapter 5 indicate that amorphous silicon oxide nanoparticles are produced from the explosive reaction of PS- NaClO_4 . This result is significant as such particles are typically produced from a reaction of gaseous precursors in an oxygen or hydrogen flame. However, the reactants in this case are in solid form initially. Likely, small silicon clusters are produced during the explosion that then oxidize and aggregate into a core and surface shell arrangement as TEM images show. As judged by the sintering present in the particles, the reaction temperature likely exceeds 1300°C. The particles are visible with the un-aided eye in the form of a white, fluffy powder that had been reported when nitric acid (HNO_3) was dropped on PS and an explosion occurred [10]. While micrographs of PS- HNO_3 product were not made available, it is likely that similar particles were produced. Other than that report, to the author's

knowledge no other observation of amorphous silica particles from PS has been reported. With a more extensive study, it may be possible for future studies to use the formation of this product as an indicator of the pressures or temperatures of the reaction and the product may change if other oxidizers are considered.

Finally, in Chapter 6, a velocity study of galvanic PS is presented using an extremely high frame rate camera (930,000 frames per second) and an on-chip measurement technique. Here it is demonstrated that small pores in a moderate porosity PS of high surface area give rise to flame propagation rates greater than 3 km/s. To date, this is the fastest known nanoenergetic material. The velocity observed by the video and the oscilloscope method are comparable. Video analysis is both expensive and time intensive, so an option to use an oscilloscope method to measure velocity is very useful. Video studies are certainly necessary to verify the on-chip method, but for rapid testing, the on-chip method works very well. The high velocities reported here approach that of conventional explosives and may indicate generation of a shock wave. Especially for fuzing applications, where high power is necessary to ignite less-sensitive energetic compounds, a shock wave is necessary.

7.2 Future Directions

This work consists of two primary components, both of which have room for development: galvanic porous silicon and nanoenergetics. First, galvanic PS research should pursue those applications where electrochemical PS has certain disadvantages such as a requirement for a power supply and custom etching chamber. Antireflection coatings for solar cells based on porous silicon have attracted a great deal of attention for improving solar cell efficiency. Some of these reports make use of a method where deposition of nanoscale noble metal particles on a Si surface followed by subsequent immersion in an HF-based solution gives

rise to etching. A true galvanic cell etching technique has not been employed however and may offer some advantages in that actual pores are generated rather than wires as is the case with the metal-assist technique. The surface of these pores is likely more stable over time than the surface of wires.

Another area where galvanic porous silicon offers use is in creating channels of tapered depth in a Si substrate. As discussed in Chapter 2, a tapered galvanic etch will occur when a Si anode is placed at increasing distance from a noble metal cathode. In other words, the PS etch will be deeper near the cathode and decrease away from the cathode. Researchers may find use for PS of tapered depth on chip for nanoenergetics analysis or could remove the PS to realize a channel in Si of tapered depth.

PS membranes may be manufactured by patterning noble metal on the top and bottom of a wafer and leaving an exposed area of Si. This offers a one step method for etching PS through an entire wafer. Current wafers require etching partially through a wafer and then using techniques such as deep reactive ion etching to remove the remaining Si and generate a membrane. PS membranes are finding use in fuel cell applications [17] and galvanic PS could certainly provide a convenient route towards fabrication. Furthermore, in terms of energy applications, galvanic PS may be considered for lithium ion battery anode use. Si is being considered for anodes in Li-ion batteries because it has a high specific capacity for Li. However, Si has a large volume increase and can crack during Li insertion. Nanoscale Si is thought to avoid some of these problems [143]. PS should be evaluated for battery use as it has nanoscale Si domains and an open structure that may accommodate some volumetric increase.

Lastly, further research for etching protocols and characterization is necessary to provide a more comprehensive guide to galvanic PS formation than given in this thesis. Electrochemical

measurements of Pt and Si in the various HF-based electrolytes can be made and predictions on etch depth may arise from those results. Additionally, modeling can be employed to plan PS thickness on devices. Modeling may be especially useful in planning for tapered PS etches.

For nanoenergetics further development of PS may be necessary, but a comprehensive look at the entire fuel and oxidizer system should be considered. Currently, NaClO_4 is very hygroscopic and difficult to determine how much is actually inside the pores. A possible substitute is sulfur. Sulfur can be applied in a molten form which then solidifies in the pores of the PS. Preliminary work from other groups as well as the group at ARL shows sulfur as a promising oxidizer. Care should be taken as SiS_2 is generated which in a humid environment hydrolyzes to H_2S , a toxic gas. Another avenue for an oxidizer is fluorine based oxidizers such as Teflon®. However, these have difficulty fitting into the small pores of the PS, and Teflon® only has a few solvents such as Fluorinert™ (available from DuPont™) in which Teflon® is only slightly soluble. Again, caution should be used as dangerous HF vapor or liquid may result following a combustion reaction.

As another route, researchers have observed that PS powder can react with nanoscale copper oxide and bismuth oxide[74]. This is promising from the standpoint that PS and nanoscale metal oxides are in fact reactive. This specific result is curious as the metal oxide particles are on the order of 10's of nm in diameter while the PS pores are only 4-5 nm. If a means of depositing nanoscale metal oxide particles in PS films can be developed a very robust system may be realized as the metal oxide materials are quite stable relative to highly hygroscopic NaClO_4 .

Depending on the application requirements, PS powder may also be explored in more depth. Galvanic PS powder is prepared very quickly as an entire wafer can be etched to yield PS

and then the PS can be mechanically scraped from the wafer. The powder can then be mixed with oxidizers to form an energetic composite.

Since PS and any oxidizer may always be very susceptible to ignition by mechanical or electrical impulse, device designs separating the oxidizer and fuel until the moment they are needed might be considered. For example, the author has found that hydrogen peroxide is a viable oxidizer for the material. A microfluidics system could be used to deliver the liquid oxidizer at a specific time to initiate the reaction.

Aside from improvements to the fuel-oxidizer system, measurements of the pressures in the PS nanoenergetic system should be made. For example, the destruction of the Si chip during explosions indicates extreme pressure may result from the explosion. Nanoindentation tests of Si indicate amorphous Si or metastable Si phases occur at pressures of several GPa as a result of the transformation from the diamond cubic to the β -tin structure [144]. Kovalev et. al. [1] suggested that destruction of PS+Si substrate requires ~ 10 GPa. It is known that a phase change in Si to a metallic phase is possible by impacting Si with a shock impact of several GPa [145]. An in-situ measurement can be made to observe the change from semiconductor to conductor [145]. A similar analysis should be possible with PS. However, knowledge of the pressure generated would be good to have as well. Prior work from the U.S. Army Research Lab has found that a piezoelectric pressure transducer is not capable of resolving the pressure produced by PS. However, a manganin pressure gauge might be employed here for accurate pressure measurement. A detailed knowledge of the pressure produced by the material will allow for prediction of the power the energetic system might produce for a variety of applications.

Lastly, the term “explosion” has been used rather loosely in this work. It is as yet unclear if a shockwave is present during the PS- NaClO_4 reaction. It may be possible that the PS- NaClO_4

is in fact a very fast combustion reaction lacking true detonation properties. There are many unanswered questions about the nature of the reaction occurring inside the pores as well as in the observed “fireball” as pictured in Figure 5.5 and Figure 6.2. Some of these questions may be resolved by employing techniques that can determine if a shockwave travels ahead of the flame front. Computer modeling of the reaction may be necessary also to determine how the dimensions of the pores and possibly the thickness of the PS layer influence reactivity. Some guidance for these studies can be found in the literature that explores metal and metal oxide nanothermite materials. Very interesting work, both experimental and computational, has analyzed how aluminum nanoparticles differ from bulk materials in a thermite reaction. Similar studies may be necessary to gain more insight into PS nanoenergetic composites.

There are many areas for improvements in galvanic PS and PS nanoenergetics in general. Both basic and applied research is possible. The researcher should keep in mind the interdisciplinary nature of this work. In other words, working with PS nanoenergetics involves the study of oxidation of Si, fabrication of PS, and energetics. It is a very broad topic and this thesis explores a great deal, but as indicated in this chapter plenty of room for future work exists.

Bibliography

- [1] Kovalev D, Timoshenko V Y, Kunzner N, Gross E and Koch F 2001 Strong explosive interaction of hydrogenated porous silicon with oxygen at cryogenic temperatures *Physical Review Letters* **87** 068301
- [2] Canham L T 1990 Silicon Quantum wire array fabrication by electrochemical and chemical dissolution of wafers *Applied Physics Letters* **57** 1064-8
- [3] Canham L ed 1997 *Properties of Porous Silicon* (London: INSPEC, The Institution of Electrical Engineers)
- [4] Feng Z C and Tsu R 1994 *Porous Silicon* (Singapore: World Scientific Publishing Co.)
- [5] Vial J-C and Derrien J eds 1995 *Porous Silicon Science and Technology* (Verlag: Springer)
- [6] Foll H, Christophersen M, Carstensen J and Hasse G 2002 Formation and application of porous silicon *Materials Science & Engineering R-Reports* **39** 93-141
- [7] Cullis A G, Canham L T and Calcott P D J 1997 The structural and luminescence properties of porous silicon *Journal of Applied Physics* **82** 909-65
- [8] Kolasinski K W 2005 Silicon nanostructures from electroless electrochemical etching *Current Opinion in Solid State & Materials Science* **9** 73-83
- [9] Perez J M, Villalobos J, McNeill P, Prasad J, Cheek R, Kelber J, Estrera J P, Stevens P D and Glosser R 1992 Direct Evidence for the Amorphous-Silicon Phase in Visible Photoluminescent Porous Silicon *Applied Physics Letters* **61** 563-5
- [10] McCord P, Yau S-L and Bard A J 1992 Chemiluminescence of Anodized and Etched Silicon: Evidence for a Luminescent Siloxene-Like Layer on Porous Silicon *Science* **257** 68-9
- [11] Liu S, Palsule C, Yi S and Gangopadhyay S 1994 Characterization of Stain-Etched Porous Silicon *Physical Review B* **49** 10318-25
- [12] Sham T K, Jiang D T, Coulthard I, Lorimer J W, Feng X H, Tan K H, Frigo S P, Rosenberg R A, Houghton D C and Bryskiewicz B 1993 Origin of Luminescence from Porous Silicon Deduced by Synchrotron-Light-Induced Optical Luminescence *Nature* **363** 331-4
- [13] Lehmann V, Jobst B, Muschik T, Kux A and Petrova-Koch V 1993 Correlation between Optical Properties and Crystallite Size in Porous Silicon *Japanese Journal of Applied Physics* **32** 2095-9
- [14] Sivakov V A, Voigt F, Berger A, Bauer G and Christiansen S H Roughness of silicon nanowire sidewalls and room temperature photoluminescence *Physical Review B* **82**
- [15] Cruz S, Honig-dOrville A and Muller J 2005 Fabrication and optimization of porous silicon substrates for diffusion membrane applications *Journal of the Electrochemical Society* **152** C418-C24

- [16] Pichonat T and Gauthier-Manuel B 2005 Development of porous silicon-based miniature fuel cells *Journal of Micromechanics and Microengineering* **15** S179-S84
- [17] Moghaddam S, Pengwang E, Jiang Y-B, Garcia A R, Burnett D J, Brinker C J, Masel R I and Shannon M A 2010 An inorganic-organic proton exchange membrane for fuel cells with a controlled nanoscale pore structure *Nat Nano* **5** 230-6
- [18] Teva J, Davis Z J and Hansen O Electroless porous silicon formation applied to fabrication of boron-silica-glass cantilevers *Journal of Micromechanics and Microengineering* **20**
- [19] Kim J W, Ryu J H, Lee K T and Oh S M 2005 Improvement of silicon powder negative electrodes by copper electroless deposition for lithium secondary batteries *Journal of Power Sources* **147** 227-33
- [20] Shin H C, Corno J A, Gole J L and Liu M L 2005 Porous silicon negative electrodes for rechargeable lithium batteries *Journal of Power Sources* **139** 314-20
- [21] Yuan H-C, Yost V E, Page M R, Stradins P, Meier D L and Branz H M 2009 Efficient black silicon solar cell with a density-graded nanoporous surface: Optical properties, performance limitations, and design rules *Applied Physics Letters* **95** 123501
- [22] Sun W, Kherani N P, Hirschman K D, Gadeken L L and Fauchet P M 2005 A three-dimensional porous silicon p-n diode for betavoltaics and photovoltaics *Advanced Materials* **17** 1230-+
- [23] Ruminski A M, King B H, Salonen J, Snyder J L and Sailor M J Porous Silicon-Based Optical Microsensors for Volatile Organic Analytes: Effect of Surface Chemistry on Stability and Specificity *Advanced Functional Materials* **20** 2874-83
- [24] Park J H, Gu L, von Maltzahn G, Ruoslahti E, Bhatia S N and Sailor M J 2009 Biodegradable luminescent porous silicon nanoparticles for in vivo applications *Nature Materials* **8** 331-6
- [25] Sailor M J 2007 Color me sensitive: Amplification and discrimination in photonic silicon nanostructures *Acs Nano* **1** 248-52
- [26] Fathauer R W, George T, Ksendzov A and Vasquez R P 1992 Visible Luminescence from Silicon-Wafers Subjected to Stain Etches *Applied Physics Letters* **60** 995-7
- [27] Sarathy J, Shih S, Jung K, Tsai C, Li K H, Kwong D L, Campbell J C, Yau S L and Bard A J 1992 Demonstration of Photoluminescence in Nonanodized Silicon *Applied Physics Letters* **60** 1532-4
- [28] Xu Y K and Adachi S 2008 Properties of light-emitting porous silicon formed by stain etching in HF/KIO₃ solution under light illumination *Journal of Applied Physics* **103**
- [29] Canham L T 1997 *Properties of Porous Silicon: Institution of Engineering and Technology*
- [30] Marrero N, Guerrero-Lemus R, Gonzalez-Diaz B and Borchert D 2009 Effect of porous silicon stain etched on large area alkaline textured crystalline silicon solar cells *Thin Solid Films* **517** 2648-50

- [31] Becker C R, Miller D C and Stoldt C R 2010 Galvanically coupled gold/silicon-on-insulator microstructures in hydrofluoric acid electrolytes: finite element simulation and morphological analysis of electrochemical corrosion *Journal of Micromechanics and Microengineering* **20** 085017
- [32] Kelly J J, Xia X H, Ashruf C M A and French P J 2001 Galvanic cell formation: a review of approaches to silicon etching for sensor fabrication *IEEE Sensors Journal* **1** 127-42
- [33] Miller D C, Becker C R and Stoldt C R 2008 Relation Between Morphology, Etch Rate, Surface Wetting, and Electrochemical Characteristics for Micromachined Silicon Subject to Galvanic Corrosion *Journal of the Electrochemical Society* **155** F253-F65
- [34] Ashruf C M A, French P J, Bressers P and Kelly J J 1999 Galvanic porous silicon formation without external contacts *Sensors and Actuators a-Physical* **74** 118-22
- [35] Splinter A, Sturmman J and Benecke W 2001 New porous silicon formation technology using internal current generation with galvanic elements *Sensors and Actuators a-Physical* **92** 394-9
- [36] Pierron O N, Macdonald D D and Muhlstein C L 2005 Galvanic effects in Si-based microelectromechanical systems: Thick oxide formation and its implications for fatigue reliability *Applied Physics Letters* **86**
- [37] Huh M, Yu Y, Kahn H, Payer J H and Heuer A H 2006 Galvanic corrosion during processing of polysilicon microelectromechanical systems - The effect of Au metallization *Journal of the Electrochemical Society* **153** G644-G9
- [38] Zhang X G 2001 *Electrochemistry of Silicon and Its Oxide* (New York: Kluwer Academic)
- [39] Lehmann V 2002 *Electrochemistry of Silicon* (Germany: Wiley-VCH)
- [40] Stansbury E E and Buchanan R A 2000 *Fundamentals of Electrochemical Corrosion* (Materials Park: ASM International)
- [41] Zhang G X 2006 Porous Silicon: Morphology and Formation Mechanisms *Modern Aspects of Electrochemistry* **39** 65-133
- [42] Zhang X G 2004 Morphology and formation mechanisms of porous silicon *Journal of the Electrochemical Society* **151** C69-C80
- [43] Lehmann V and Gosele U 1991 Porous Silicon Formation - a Quantum Wire Effect *Applied Physics Letters* **58** 856-8
- [44] Peng K, Lu A, Zhang R and Lee S T 2008 Motility of Metal Nanoparticles in Silicon and Induced Anisotropic Silicon Etching *Advanced Functional Materials* **18** 3026-35
- [45] Rossi C, Zhang K, Esteve D, Alphonse P, Tailhades P and Vahlas C 2007 Nanoenergetic materials for MEMS: A review *Journal of Microelectromechanical Systems* **16** 919-31
- [46] Apperson S, Shende R V, Subramanian S, Tappmeyer D, Gangopadhyay S, Chen Z, Gangopadhyay K, Redner P, Nicholich S and Kapoor D 2007 Generation of fast propagating

- combustion and shock waves with copper oxide/aluminum nanothermite composites *Applied Physics Letters* **91**
- [47] Puszynski J A 2009 Processing and characterization of aluminum-based nanothermites *Journal of Thermal Analysis and Calorimetry* **96** 677-85
 - [48] Ferguson J D, Buechler K J, Weimer A W and George S M 2005 SnO₂ atomic layer deposition on ZrO₂ and Al nanoparticles: Pathway to enhanced thermite materials *Powder Technology* **156** 154-63
 - [49] Blobaum K J, Reiss M E, Lawrence J M P and Weihs T P 2003 Deposition and characterization of a self-propagating CuOx/Al thermite reaction in a multilayer foil geometry *Journal of Applied Physics* **94** 2915-22
 - [50] Son S F, Asay B W, Foley T J, Yetter R A, Wu M H and Risha G A 2007 Combustion of nanoscale Al/MoO₃ thermite in microchannels *Journal of Propulsion and Power* **23** 715-21
 - [51] Puszynski J A, Bulian C J and Swiatkiewicz J J 2007 Processing and ignition characteristics of aluminum-bismuth trioxide nanothermite system *Journal of Propulsion and Power* **23** 698-706
 - [52] Zhou L, Piekiet N, Chowdhury S, Lee D and Zachariah M R 2009 Transient ion ejection during nanocomposite thermite reactions *Journal of Applied Physics* **106**
 - [53] Sullivan K and Zachariah M R 2010 Simultaneous Pressure and Optical Measurements of Nanoaluminum Thermites: Investigating the Reaction Mechanism *Journal of Propulsion and Power* **26** 467-72
 - [54] Levitas V I, Pantoya M L, Chauhan G and Rivero I 2009 Effect of the Alumina Shell on the Melting Temperature Depression for Aluminum Nanoparticles *Journal of Physical Chemistry C* **113** 14088-96
 - [55] Levitas V I, Pantoya M L and Dikici B 2008 Melt dispersion versus diffusive oxidation mechanism for aluminum nanoparticles: Critical experiments and controlling parameters *Applied Physics Letters* **92**
 - [56] Levitas V I, Asay B W, Son S F and Pantoya M 2007 Mechanochemical mechanism for fast reaction of metastable intermolecular composites based on dispersion of liquid metal *Journal of Applied Physics* **101**
 - [57] Gur'ev D L, Gordopolov Y A, Batsanov S S, Merzhanov A G and Fortov V E 2006 Solid-state detonation in the zinc-sulfur system *Applied Physics Letters* **88**
 - [58] Merzhanov A G, Gordopolov Y A and Trofimov V S 1996 On the possibility of gasless detonation in condensed systems *Shock Waves* **6** 157-9
 - [59] Zhang K, Rossi C, Rodriguez G A A, Tenailleau C and Alphonse P 2007 Development of a nano-Al/CuO based energetic material on silicon substrate *Applied Physics Letters* **91**
 - [60] Apperson S J, Bezmelnitsyn A V, Thiruvengadathan R, Gangopadhyay K, Gangopadhyay S, Balas W A, Anderson P E and Nicolich S M 2009 Characterization of Nanothermite Material for Solid-Fuel Microthruster Applications *Journal of Propulsion and Power* **25** 1086-91

- [61] Singh S K, Schlup J R, Fan L T and Sur B 1988 Modeling of Thermal-Oxidation of Silicon *Industrial & Engineering Chemistry Research* **27** 1707-14
- [62] Deal B E and Grove A S 1965 General Relationship for Thermal Oxidation of Silicon *Journal of Applied Physics* **36** 3770-&
- [63] Salonen J, Lehto V P and Laine E 1997 Thermal oxidation of free-standing porous silicon films *Applied Physics Letters* **70** 637-9
- [64] Salonen J, Lehto V P and Laine E 2000 Investigations of activation energy of porous silicon oxidation using calorimetric methods *Journal of Porous Materials* **7** 335-8
- [65] Salonen J, Lehto V P and Laine E 1997 The room temperature oxidation of porous silicon *Applied Surface Science* **120** 191-8
- [66] Cisneros R, Pfeiffer H and Wang C M 2010 Oxygen Absorption in Free-Standing Porous Silicon: A Structural, Optical and Kinetic Analysis *Nanoscale Research Letters* **5** 686-91
- [67] Mikulec F V, Kirtland J D and Sailor M J 2002 Explosive nanocrystalline porous silicon and its use in atomic emission spectroscopy *Advanced Materials* **14** 38-41
- [68] Clement D, Diener J, Gross E, Kunzner N, Timoshenko V Y and Kovalev D 2005 Highly explosive nanosilicon-based composite materials *Physica Status Solidi a-Applications and Materials Science* **202** 1357-64
- [69] Currano L J and Churaman W A 2009 Energetic Nanoporous Silicon Devices *Journal of Microelectromechanical Systems* **18** 799-807
- [70] du Plessis M 2007 Properties of porous silicon nano-explosive devices *Sensors and Actuators a-Physical* **135** 666-74
- [71] du Plessis M 2007 Relationship between specific surface area and pore dimension of high porosity nanoporous silicon - Model and experiment *Physica Status Solidi a-Applications and Materials Science* **204** 2319-28
- [72] Lazarouk S K, Dolbik A V, Labunov V A and Borisenko V E 2007 Spherical plasmoids formed upon the combustion and explosion of nanostructured hydrated silicon *Jetp Letters* **84** 581-4
- [73] Abrahamson J and Dinniss J 2000 Ball lightning caused by oxidation of nanoparticle networks from normal lightning strikes on soil *Nature* **403** 519-21
- [74] Subramanian S, Tiegs T, Limaye S, Kapoor D and Redner P 2008 NANOPOROUS SILICON BASED ENERGETIC MATERIALS. In: *Army Science Conference*,
- [75] Miller D C, Boyce B L, Gall K and Stoldt C R 2007 Galvanic corrosion induced degradation of tensile properties in micromachined polycrystalline silicon *Applied Physics Letters* **90** 191902
- [76] Ball R J, Evans R and Stevens R 2002 Finite element (FE) modelling of current density on the valve regulated lead/acid battery positive grid *Journal of Power Sources* **103** 213-22
- [77] Kovacs G T A 1998 *Micromachined Transducers Sourcebook* (Boston: WCB McGraw-Hill)

- [78] Madou M J 2002 *Fundamentals of Microfabrication: The Science of Miniaturization*: CRC)
- [79] Ashurst W R, Wijesundara M B J, Carraro C and Maboudian R 2004 Tribological impact of SiC encapsulation of released polycrystalline silicon microstructures *Tribology Letters* **17** 195-8
- [80] Williams J A and Le H R 2006 Tribology and MEMS *Journal of Physics D: Applied Physics* **39** R201-R14
- [81] Miller D C, Boyce B L, Gall K and Stoldt C R 2007 Galvanic corrosion induced degradation of tensile properties in micromachined polycrystalline silicon *Applied Physics Letters* **90**
- [82] Chasiotis I and Knauss W G 2003 *Comprehensive Structural Integrity Vol. 8: Interfacial and Nanoscale Failure* (Boston: Elsevier Science)
- [83] Buehler M G, Grant S D and Thurber W R 1978 Bridge and Van-Der-Pauw Sheet Resistors for Characterizing Line-Width of Conducting Layers *Journal of the Electrochemical Society* **125** 650-4
- [84] Miller K, Cowen A, Hames G and Hardy B 2005 *SOIMUMPS Design Handbook, Rev. 4* (Research Triangle Park: MEMSCAP, Inc.)
- [85] Doan V V and Sailor M J 1992 Luminescent Color Image Generation on Porous Silicon *Science* **256** 1791-2
- [86] Miller D C, Boyce B L, Kotula P G and Stoldt C R 2008 Connections between morphological and mechanical evolution during galvanic corrosion of micromachined polycrystalline and monocrystalline silicon *Journal of Applied Physics* **103**
- [87] Redaelli E, Bertolini L, Peelen W and Polder R 2006 FEM-models for the propagation period of chloride induced reinforcement corrosion *Materials and Corrosion-Werkstoffe Und Korrosion* **57** 628-35
- [88] Lindeman D 1996 Steady-state current conduction analysis featuring electrochemical kinetics *Finite Elements in Analysis and Design* **22** 187-94
- [89] Herbstritt D, Weber A and Ivers-Tiffée E 2001 Modelling and DC-polarisation of a three dimensional electrode/electrolyte interface *Journal of the European Ceramic Society* **21** 1813-6
- [90] Vankeerberghen M, Gavrilov S and Nelissen G 2001 Finite element calculation of the polarisation behaviour of a metal in an aqueous solution using the dilute solution model *Corrosion Science* **43** 37-51
- [91] Jia J X, Song G, Atrens A, St John D, Baynham J and Chandler G 2004 Evaluation of the BEASY program using linear and piecewise linear approaches for the boundary conditions *Materials and Corrosion-Werkstoffe Und Korrosion* **55** 845-52
- [92] Teva J, Davis Z and Hansen O 2010 Electroless porous silicon formation applied to fabrication of boron-silica-glass cantilevers *Journal of Micromechanics and Microengineering* **20** 015034
- [93] Doig P and Flewitt P E J 1979 A Finite-Difference Numerical-Analysis of Galvanic Corrosion for Semi-Infinite Linear Coplanar Electrodes *Journal of the Electrochemical Society* **126** 2057-63

- [94] Miller D C, Boyce B L, Dugger M T, Buchheit T E and Gall K 2007 Characteristics of a commercially available silicon-on-insulator MEMS material *Sensors and Actuators a-Physical* **138** 130-44
- [95] Burrows B and Jasinski R 1968 Cu/CuF₂ Couple in Anhydrous Hydrogen Fluoride *Journal of the Electrochemical Society* **115** 348-&
- [96] Totir G G, Chottiner G S, Gross C L and Scherson D A 2002 XPS studies of the chemical and electrochemical behavior of copper in anhydrous hydrogen fluoride *Journal of Electroanalytical Chemistry* **532** 151-6
- [97] Hill E G and Sirkar A P 1909 The electric conductivity and density of solutions of hydrogen fluoride *Proceedings of the Royal Society of London Series a-Containing Papers of a Mathematical and Physical Character* **83** 130-48
- [98] Broderick S J 1962 Conductivity of Hydrofluoric Acid Solutions and the Effect of the Impurities, Sulfurous and Hydrofluosilicic Acids *Journal of Chemical & Engineering Data* **7** 55-7
- [99] Jia J X, Song G L and Atrens A 2006 Influence of geometry on galvanic corrosion of AZ91D coupled to steel *Corrosion Science* **48** 2133-53
- [100] Munn R S and Devereux O F 1991 Numerical Modeling and Solution of Galvanic Corrosion Systems .1. Governing Differential-Equation and Electrode Boundary-Conditions *Corrosion* **47** 612-8
- [101] Munn R S and Devereux O F 1991 Numerical Modeling and Solution of Galvanic Corrosion Systems .2. Finite-Element Formulation and Descriptive Examples *Corrosion* **47** 618-34
- [102] Jorcin J B, Blanc C, Pebere N, Tribollet B and Vivier V 2008 Galvanic coupling between pure copper and pure aluminum experimental approach and mathematical model *Journal of the Electrochemical Society* **155** C46-C51
- [103] Perez N 2004 *Electrochemistry and Corrosion Science* (Boston: Kluwer)
- [104] Jia J X, Song G L and Atrens A 2007 Experimental measurement and computer simulation of galvanic corrosion of magnesium coupled to steel *Advanced Engineering Materials* **9** 65-74
- [105] Li X and Bohn P W 2000 Metal-assisted chemical etching in HF/H₂O₂ produces porous silicon *Applied Physics Letters* **77** 2572-4
- [106] Bouchaour M, Ould-Abbas A, Diaf N and Sari N C 2004 Effect of drying on porous silicon *Journal of Thermal Analysis and Calorimetry* **76** 677-84
- [107] Kritwattanakhorn J, Bauersfeld M L, Kovacs A, Muller B, Mescheder U, Rademacher S and Wollenstein J 2007 Optimization of platinum adhesion in electrochemical etching process for multi-sensor systems *Sensors and Actuators B-Chemical* **127** 126-31
- [108] Bomchil G, Herino R, Barla K and Pfister J C 1983 PORE-SIZE DISTRIBUTION IN POROUS SILICON STUDIED BY ADSORPTION-ISOTHERMS *Journal of the Electrochemical Society* **130** 1611-4

- [109] Herino R, Bomchil G, Barla K, Bertrand C and Ginoux J L 1987 POROSITY AND PORE-SIZE DISTRIBUTIONS OF POROUS SILICON LAYERS *Journal of the Electrochemical Society* **134** 1994-2000
- [110] Lowell S, Shields J E, Thomas M A and Thommes M 2004 *Characterization of Porous Solids and Powders: Surface Area, Pore Size and Density* (Dordrecht: Kluwer Academic Publishers)
- [111] Ruike M, Houzouji M, Motohashi A, Murase N, Kinoshita A and Kaneko K 1996 Pore structure of porous silicon formed on a lightly doped crystal silicon *Langmuir* **12** 4828-31
- [112] Barrett E P, Joyner L G and Halenda P P 1951 THE DETERMINATION OF PORE VOLUME AND AREA DISTRIBUTIONS IN POROUS SUBSTANCES .1. COMPUTATIONS FROM NITROGEN ISOTHERMS *Journal of the American Chemical Society* **73** 373-80
- [113] Pant A K, Murarka S P, Shepard C and Lanford W 1992 Kinetics of Platinum Silicide Formation During Rapid Thermal-Processing *Journal of Applied Physics* **72** 1833-6
- [114] Conforto E and Schmid P E 2008 Platinum silicide phase transformations controlled by a nanometric interfacial oxide layer *Thin Solid Films* **516** 7467-74
- [115] Hossain M, Subramanian S, Bhattacharya S, Gao Y F, Apperson S, Shende R, Guha S, Arif M, Bai M, Gangopadhyay K and Gangopadhyay S 2007 Crystallization of amorphous silicon by self-propagation of nanoengineered thermites *Journal of Applied Physics* **101**
- [116] Prabakaran R, Kesavamoorthy R and Singh A 2005 Optical and microstructural investigations of porous silicon *Bulletin of Materials Science* **28** 219-25
- [117] Troia A, Giovannozzi A and Amato G 2009 Preparation of tunable silicon q-dots through ultrasound *Ultrasonics Sonochemistry* **16** 448-51
- [118] Becker C R, Currano L J, Churaman W A and Stoldt C R 2010 Thermal Analysis of the Exothermic Reaction between Galvanic Porous Silicon and Sodium Perchlorate *ACS Applied Materials and Interfaces* **2** 2298-3003
- [119] Churaman W A, Currano L J and Becker C R 2010 Initiation and reaction tuning of nanoporous energetic silicon *Journal of Physics and Chemistry of Solids* **71** 69-74
- [120] Roura P, Farjas J and Cabarrocas P R I 2009 Characterization of amorphous and nanostructured Si films by differential scanning calorimetry *Thin Solid Films* **517** 6239-42
- [121] Wydeven T 1970 Catalytic Decomposition of Sodium Chlorate *Journal of Catalysis* **19** 162
- [122] Devlin D J and Herley P J 1987 Thermal-Decomposition and Dehydration of Sodium-Perchlorate Monohydrate *Reactivity of Solids* **3** 75-84
- [123] Gupta P, Colvin V L and George S M 1988 hydrogen desorption kinetics from monohydride and dihydride species on silicon surfaces *Physical Review B* **37** 8234-43
- [124] Shimada S 1992 Acoustic emission in the process of dehydration and thermal decomposition of NaClO₄•H₂O *Thermochimica Acta* **196** 237-46

- [125] Arita Y, Kuranari K and Sunohara Y 1976 Thermal-Behavior of Porous Silicon *Japanese Journal of Applied Physics* **15** 1655-64
- [126] Seipenbusch M, Rothenbacher S, Kirchhoff M, Schmid H J, Kasper G and Weber A P Interparticle forces in silica nanoparticle agglomerates *Journal of Nanoparticle Research* **12** 2037-44
- [127] Vaccaro G, Agnello S, Buscarino G and Gelardi F M 2010 Thermally Induced Structural Modification of Silica Nanoparticles Investigated by Raman and Infrared Absorption Spectroscopies *The Journal of Physical Chemistry C* **114** 13991-7
- [128] Barthel H, Heinemann M, Stintz M and Wessely B 1999 Particle sizes of fumed silica *Particle & Particle Systems Characterization* **16** 169-76
- [129] Ogata Y H, Yoshimi N, Yasuda R, Tsuboi T, Sakka T and Otsuki A 2001 Structural change in p-type porous silicon by thermal annealing *Journal of Applied Physics* **90** 6487-92
- [130] Hibino Y, Hanafusa H, Ema K and Hyodo S 1985 Raman-Study on Silica Optical Fibers Subjected to High-Tensile Stress *Applied Physics Letters* **47** 812-4
- [131] Buscarino G, Ardizzone V, Vaccaro G, Agnello S and Gelardi F M Atomic force microscopy and Raman investigation on the sintering process of amorphous SiO₂ nanoparticles *Journal of Applied Physics* **108**
- [132] Churaman W A, Currano L J, Singh A K, Rai U S, Dubey M, Amirtharaj P and Ray P C 2008 Understanding the high energetic behavior of nano-energetic porous silicon *Chemical Physics Letters* **464** 198-201
- [133] Ehrman S H, Friedlander S K and Zachariah M R 1998 Characteristics of SiO₂/TiO₂ nanocomposite particles formed in a premixed flat flame *Journal of Aerosol Science* **29** 687-706
- [134] Singh P, Sharma S N and Ravindra N M 2010 Applications of Porous Silicon Thin Films in Solar Cells and Biosensors *JOM Journal of the Minerals Metals and Materials Society* **62** 15-24
- [135] Orosco M M, Pacholski C and Sailor M J 2009 Real-time monitoring of enzyme activity in a mesoporous silicon double layer *Nature Nanotechnology* **4** 255-8
- [136] Prakash A, McCormick A V and Zachariah M R 2005 Synthesis and reactivity of a super-reactive metastable intermolecular composite formulation of Al/KMnO₄ *Advanced Materials* **17** 900-3
- [137] Prakash A, McCormick A V and Zachariah M R 2005 Tuning the reactivity of energetic nanoparticles by creation of a core-shell nanostructure *Nano Letters* **5** 1357-60
- [138] Reid D L, Russo A E, Carro R V, Stephens M A, LePage A R, Spalding T C, Petersen E L and Seal S 2007 Nanoscale additives tailor energetic materials *Nano Letters* **7** 2157-61
- [139] Martirosyan K S, Wang L, Vicent A and Luss D 2009 Synthesis and performance of bismuth trioxide nanoparticles for high energy gas generator use *Nanotechnology* **20**

- [140] Bhattacharya S, Gao Y F, Apperson S, Subramaniam S, Shende R, Gangopadhyay S and Talantsev E 2006 A novel on-chip diagnostic method to measure burn rates of energetic materials *Journal of Energetic Materials* **24** 1-15
- [141] Chattopadhyay S, Li X L and Bohn P W 2002 In-plane control of morphology and tunable photoluminescence in porous silicon produced by metal-assisted electroless chemical etching *Journal of Applied Physics* **91** 6134-40
- [142] Fan H J, Kuok M H, Ng S C, Boukherroub R, Baribeau J M, Fraser J W and Lockwood D J 2002 Brillouin spectroscopy of acoustic modes in porous silicon films *Physical Review B* **65** 165330
- [143] Urbonaite S, Baglien I, Ensling D and Edstrom K Effect of ethanol-assisted electrode fabrication on the performance of silicon anodes *Journal of Power Sources* **195** 5370-3
- [144] Jang J I, Lance M J, Wen S Q, Tsui T Y and Pharr G M 2005 Indentation-induced phase transformations in silicon: influences of load, rate and indenter angle on the transformation behavior *Acta Materialia* **53** 1759-70
- [145] Gilev S D and Trubachev A M 2004 Metallization of silicon in a shock wave: the metallization threshold and ultrahigh defect densities *Journal of Physics-Condensed Matter* **16** 8139-53
- [146] Churaman W A, Becker C R, Metcalfe G D, Hanrahan B M, Currano L J and Stoldt C R 2010 Optical initiation of nanoporous energetic silicon for safing and arming technologies *Proceedings of SPIE* **7795** 779506
- [147] Sharma S N, Sharma R K, Bhagavannarayana G, Samanta S B, Sood K N and Lakshmikumar S T 2006 Demonstration of the formation of porous silicon films with superior mechanical properties, morphology and stability *Materials Letters* **60** 1166-9
- [148] du Plessis M 2008 Nanoporous silicon explosive devices *Materials Science and Engineering B-Solid State Materials for Advanced Technology* **147** 226-9
- [149] Sui Z F, Leong P P, Herman I P, Higashi G S and Temkin H 1992 Raman Analysis of Light-Emitting Porous Silicon *Applied Physics Letters* **60** 2086-8
- [150] Campbell I H and Fauchet P M 1986 The Effects of Microcrystal Size and Shape on the One Phonon Raman-Spectra of Crystalline Semiconductors *Solid State Communications* **58** 739-41
- [151] Yang M, Huang D M, Hao P H, Zhang F L, Hou X Y and Wang X 1994 Study of the Raman Peak Shift and the Linewidth of Light-Emitting Porous Silicon *Journal of Applied Physics* **75** 651-3
- [152] Manotas S, Agullo-Rueda F, Moreno J D, Ben-Hander F, Guerrero-Lemus R and Martinez-Duart J M 2000 Determination of stress in porous silicon by micro-Raman spectroscopy *Physica Status Solidi a-Applied Research* **182** 245-8
- [153] Kozlowski F and Lang W 1992 Spatially Resolved Raman Measurements at Electroluminescent Porous N-Silicon *Journal of Applied Physics* **72** 5401-8
- [154] Lei Z K, Kang Y L, Cen H and Ming H 2006 Variability on Raman shift to stress coefficient of porous silicon *Chinese Physics Letters* **23** 1623-6

- [155] Bellet D, Lamagnere P, Vincent A and Brechet Y 1996 Nanoindentation investigation of the Young's modulus of porous silicon *Journal of Applied Physics* **80** 3772-6

Appendix A

Techniques for Preparation of Highly reactive Electrochemical Porous Silicon

A.1. Preface

The research presented in Appendix A describes early work in evaluation of electrochemical porous silicon for nanoenergetics. It complements the data presented in Chapter 3. The chapter focuses on improving the mechanical stability of PS (i.e. eliminating cracking of the PS layer which can ultimately lead to spontaneous combustion) and evaluating various etching conditions and morphologies for energetic strength. The information in this chapter is beneficial as so many methods for the production of PS are possible, that the characterization presented here helps fill in some gaps. The data presented here is similar to that of ARL tech report 4717, by C.R. Becker. Section A.3 of this appendix is composed of material similar to that of a section written by C.R. Becker for a paper titled “Optical initiation of nanoporous energetic silicon for safing and arming technologies” published in 2010 in: SPIE Proceedings Vol. 7795, Optical Technologies for Arming, Safing, Fuzing, and Firing VI, Fred M. Dickey; Richard A. Beyer, Editors, 779506, Ref. [146]. This work discusses using Raman spectroscopy to estimate the stress in PS as it is heated and has been adapted for publication in this thesis. In this case the study investigated the critical laser power density necessary for ignition. It may be used in future work to analyze the sensitivity, i.e. the susceptibility of PS to ignition by mechanical or thermal stimuli. The work is also based on a process in which the wafer is textured prior to etching, a process that appeared in the literature [147] as a means to make high porosity PS films that were not prone to cracking. C.R. Becker was responsible for the development of the technique first discussed in the literature for use in PS nanoenergetics, and a

study on the velocity of the materials was published under Churaman, W.A., Currano L.J., and Becker C.R. [119].

A.2. Summary of Electrochemical PS Ignition Studies

From past work at ARL, it has been determined that PS samples prepared at 18 mA/cm^2 and filled with a saturated solution of NaClO_4 in ethanol result in the most dramatic exothermic reactions. As of yet, no groups have reported an experimentally measured value for the energy released upon ignition of PS/oxidant. Researchers, however, report qualitative results from sight and sound. In principle, a sample with the largest specific surface area is desired to produce the most exothermic reaction. However, the porosity and pore size are important in that highly porous samples are mechanically unstable and if the pore size is too small the oxidizer cannot fill the pores. It is thought that a pore diameter on the order of 3.5 nm is optimal for PS energetics[148].

Recently we have found that samples etched at 36 mA/cm^2 show a pronounced increase in reaction energy over our previous work with 18 mA/cm^2 samples. This current density corresponds to a thickness of 57.5 μm and pore diameter of 4.4 nm. At this etch current however, the layers are mechanically unstable. Two methods to reduce the instability have been investigated: tapering the etch current density and pentane drying.

It is thought that by tapering the etch, a finer pore structure can be realized at the Si/PS boundary, and the PS can be anchored better to the substrate. Additionally, the residual stress created from transitioning to a large pore diameter to the bulk Si, may be reduced by decreasing the pore diameter with time. We have found that a die etched at 36 mA/cm^2 for 30 minutes in 25% HF is unstable after drying, although this can be reduced with pentane drying. However, a die that is anodized for 30 min at 36 mA/cm^2 , then reduced to 27 mA/cm^2 for 5 minutes, then to

18 mA/cm² for 5 minutes is mechanically stable after drying, even without the aid of pentane. Additionally we find that reducing to 18 mA/cm² for 5 minutes then to 9 mA/cm² is stable, but simply reducing to 9 mA/cm² is not stable even with pentane drying. It is worthy to note that in 33% HF/EtOH solutions, layers are stable up to 90 mA/cm². Table A.1 and Table A.2 summarize our results.

Table A.1: Etch conditions, drying methods, and energetic reaction strength: 25% HF/EtOH.

Electrolyte Composition	25% HF/EtOH						
Initial current density	9	18	27	36	36	36	36
Initial etch time	30	30	30	30	30	30	30
Current reduction 1 (5 min)	na	na	na	na	na	27	18
Current reduction 2 (5 min)	na	na	na	na	na	18	9
Pentane drying	n	n	n	n	y	y	n
Anneal (y/n)	n	n	n	n	y	n	n
Stable layer (y/n)	y	y	y	n	y	y	y
Layer stable after oxidant	y	y	y	n	y	n	n
Reaction	na	moderate	na	strong	weak	strong	strong

Table A.2: Etch conditions, drying methods, and energetic reaction strength: 33% HF/EtOH.

Electrolyte Composition	33 % HF/EtOH (2:1) 1-30 ohm-cm						
Initial Current Density	9	18	27	36	54	72	90
initial etch time	30	30	30	30	30	30	30
pentane drying	n	n	n	n	n	n	n
anneal (y/n)	n	n	n	n	n	n	n
stable layer (y/n)	y	y	y	y	y	y	y
layer stable after oxidant	y	y	y	y	y	y	n
reaction	na	na	na	weak	moderate	moderate	strong

The tables also indicate whether a PS layer cracked after filling with the oxidant solution. While the layers may be stable after initial drying, maintaining their integrity after the oxidant

solution is deposited is difficult. Despite PS layer cracking, strong exothermic reactions are realized. Annealing at 300 °C for one hour in air did stabilize the layer, but the resulting reaction was very weak. The PS layer grows an oxide layer in these annealing conditions that may be inhibiting the reaction strength. A benefit, however, is that the PS becomes hydrophilic under these conditions and while it may also be inhibiting pore filling, it may allow for water soluble oxidants to be introduced to the pores. A weak reaction is typical of a very low sound similar to a “puff”, a moderate reaction results in a more intense sound, and a strong reaction has a very loud, sharp, “bang” that approached 120-130 decibels.

Videos of the ignition tend to show either a large flame or blue plasma-like halo. Since we are not recording with a high speed camera, the blue plasma-like halo could be a matter of not having the speed to catch a fast moving flame. Our most energetic reaction to date of a 36 mA/cm² die is shown in Figure A.1 on the left. In this reaction the die broke in half. Figure A.1 on the right shows another strong reaction with a flame visible, but the die did not break.

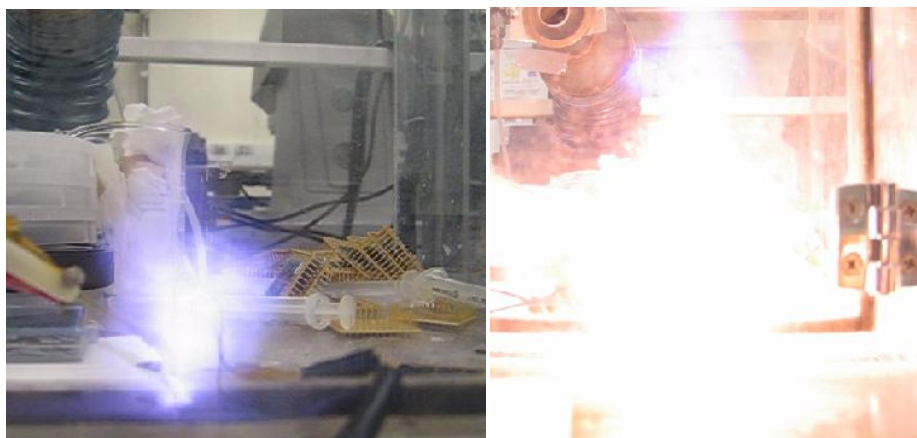


Figure A.1: 36 mA/cm² ignition tests. The chip on the left broke in half, the chip on the right did not.

Of the electrochemical etch conditions, the most successful in terms of leading to highly reactive explosions that typically destroyed the Si chip is a technique in which the Si wafer is textured in a KOH etching solution prior to electrochemical etching.

A.3. Raman Characterization of PS Stress

A.3.1. Sample Preparation

The PS is fabricated on a double-side polished, 1-20 ohm-cm, boron doped, <100> oriented wafer. Prior to PS formation, the surface of the wafer is roughened by submerging it in a heated mixture of sodium hydroxide and water. Thick PS films of high porosity are typically susceptible to cracking as they dry after the etch process; however, using this texturing process[147], PS films ~130 μm thick and with porosity ~74% (determined by a gravimetric method), can be fabricated. A thick PS film compared to a thin PS film is favorable for maximum Si fuel to be available in the reaction. A layer of 20nm-Ti/85nm-Pt is deposited on the backside of the wafer to provide electrical contact. The contact resistance of the Ti/Pt layer is reduced by annealing the wafer in nitrogen at 700°C for 60 seconds. The sample is then placed in a Teflon etch cell, where electrical contact is made to the Ti/Pt backside. While protecting the backside with an o-ring seal, the top-side of the wafer is exposed to a 2:1 mixture of HF:ethanol etchant that is added to the etch cell. With the electrolyte solution in contact with the silicon substrate, a gold wire, serving as the cathode, is submerged in the solution. Electrical contact is made between the cathode and Ti/Pt anode. Applying a current from an external power supply causes the formation of nanopores with a hydrogen passivated surface. The samples are allowed to dry in pentane which further reduces the chances of cracking because pentane has very low surface tension. The fabrication process is similar to that presented by Churaman et al.[119]. Figure A.2 A) shows an SEM image of the pyramids at the surface that result from the texturing process, Figure A.2 B) shows the full thickness of the film, and Figure A.2 C) shows an oblique view of the surface.

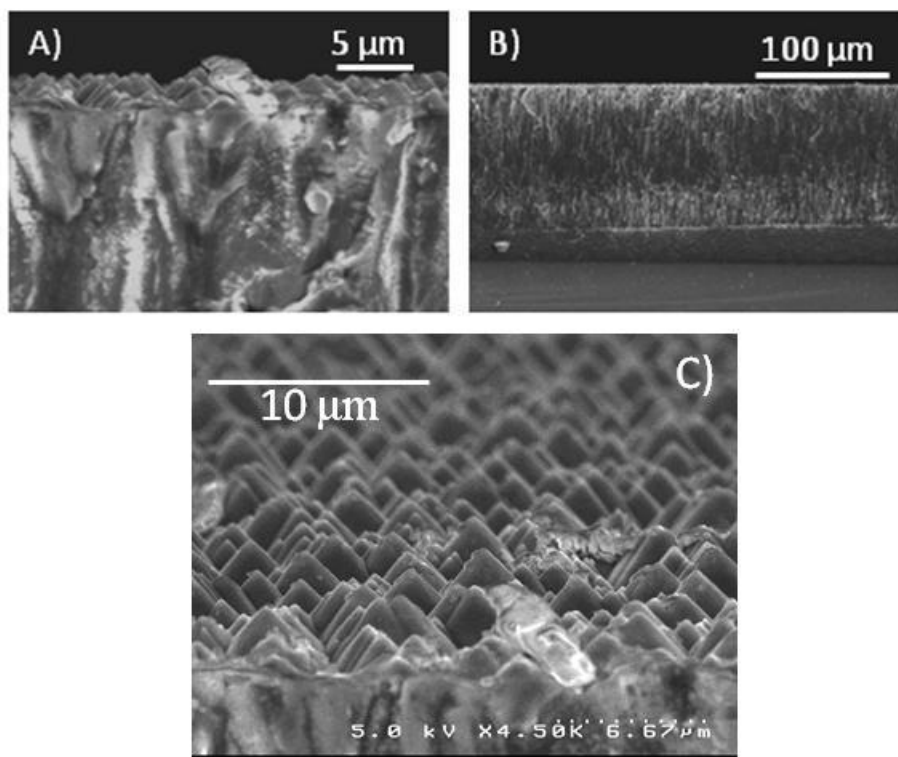


Figure A.2: SEM images of PS. A) Cross section near surface of PS, B) full cross-section of PS film, and C) oblique view of the textured surface.

A.3.2. Laser Ignition Testing

Further figures, not the production of C.R. Becker, that describe the test apparatus are available in Ref. [146]. The continuous wave laser used in this test was a Model 177G Series air-cooled argon laser designed by Spectra Physics. The continuous wave laser outputs at 514nm. The laser can output a maximum power of 420mW, and has a beam diameter of approximately 0.82mm. The PS was placed in direct line of sight of the laser, approximately 23cm away from the beam. The sample was dried for 6.5 minutes in ambient air, rather than in nitrogen, and was successfully ignited instantaneously at 37.7mW, or a power density of $2.7\text{kW}/\text{cm}^2$. This was the lowest output power available for the laser.

A.3.3. Raman Spectroscopy Characterization

Our results indicated that PS-NaClO₄ is ignited at a critical laser power density of 2.71kW/cm². Using Raman spectroscopy, we examine the effect the laser heating has on the PS structure. The crystallite sizes of silicon in PS, strain in the structure, and strain effects induced by heating can be characterized using Raman spectroscopy[149-155]. The peak in the Raman spectrum of PS typically is red shifted and broader than that of the standard Si peak at ~520 cm⁻¹ and FWHM of ~4 cm⁻¹. When heated, this peak is further shifted and broader. This shift and broadening is a result of stress in the sample. Figure A.3 shows Raman spectroscopy (Renishaw inVia, 514nm laser wavelength, 100x objective lens) results of a single crystal Si sample and of a PS sample prepared under the same conditions as the PS used for ignition. The pores are not filled with NaClO₄ in these measurements as the laser could ignite the sample and damage the instrument.

The literature reports that power densities between 0.3 and 1kW/cm² will not induce stress from heating[152, 153]. Additionally, we find that long signal accumulation times can induce heating effects as the sample slowly heats from the laser illumination. The lowest power setting, 0.16kW/cm², produces very similar Raman spectra for accumulation times up to 250s. However, as the accumulation times increases to 750s, we see a peak broadening and shift. At 1.62kW/cm² with an accumulation time of 150s, which illuminates the sample with the same energy (243kJ/cm²) as 0.16kW/cm² for 750s, very similar spectra are produced. The spectrum is also very similar at 8.1kW/cm² for 30s (243kJ/cm²). At 8.1kW/cm² for 10s (810 kJ/cm²), the spectrum shifts even further.

The results in Figure A.3 demonstrate that as laser power increases, the time to induce a shift in the PS spectrum, which corresponds to a stress, decreases. An exact numerical comparison of Raman results to the laser ignition results is difficult because a Raman spectrum requires at least several seconds to collect; however, in the ignition tests, at several kW/cm² of power, the laser instantaneously ignites the sample. A good estimate of the laser power necessary for ignition is made by comparing the results at 0.16kW/cm² and at 1.62kW/cm² with calculated Raman spectra shown as dotted curves in Figure A.3. The calculated spectra, which are reproduced from a model proposed by Sui et al.[149], equation (A.1), and is similar to the model by Campbell and Fauchet [150] fit the data well for the Raman spectra without heat induced effects. In equation (A.1), $I(\omega)$ is the intensity, q is expressed in units of $2\pi/a$, L is the crystallite size in units of a , a is the lattice constant of Si of 0.54nm, Γ is the natural linewidth for crystalline Si ($\sim 4 \text{ cm}^{-1}$), and $\omega(q) = A - Bq^2$ is the dispersion relation for LO phonons along [001] in Si where $A = 520.5 \text{ cm}^{-1}$ and $B = 120 \text{ cm}^{-1}$.

$$I(\omega) \propto \int e^{\frac{-q^2 L^2}{4}} \frac{d^3 q}{[\omega - \omega(q)]^2 + (\frac{\Gamma}{2})^2} \quad (\text{A.1})$$

The modeled data assume crystallite sizes of either 2 or 3nm, and do not account for stress in the sample. The measured spectrum lies between the curves for 2 and 3 nm, indicating the sample probably has a crystallite size between those two values. For power densities greater than 0.16kW/cm², or for long accumulation times, the spectrum is shifted and broadened and the model no longer fits the data. The error in the fit results from stress in the PS structure induced by heating effects.

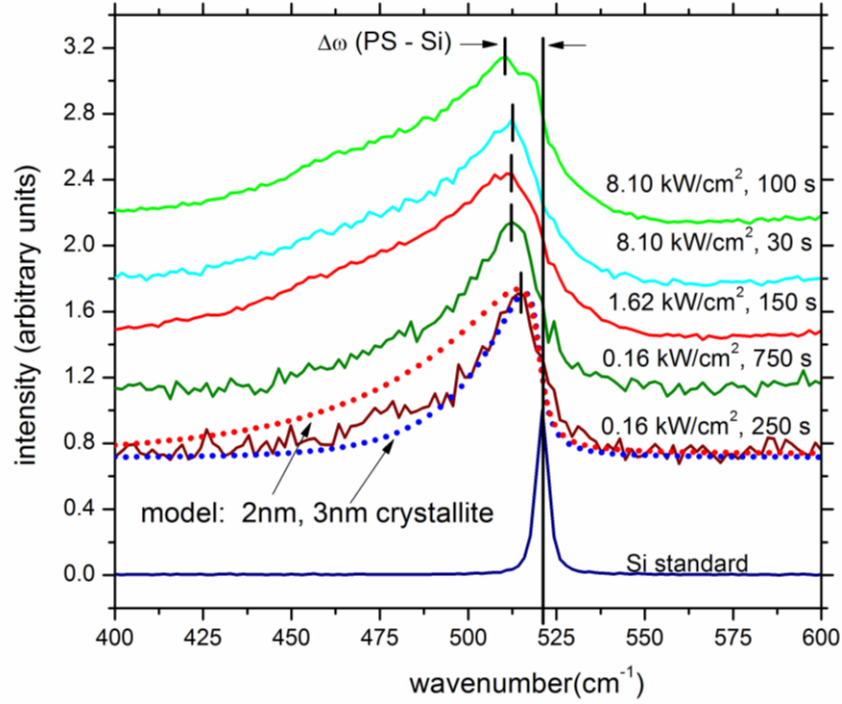


Figure A.3: Raman spectroscopy results of PS samples without NaClO₄. The solid curves are spectra collected at unique power densities and accumulation times. The dotted curves represent predicted spectra. The vertical bars aid in visualizing the shift of each sample.

The Raman peak shift, $\Delta\omega$, can be used to predict the stress, σ , in the PS structure[154], equation (A.2).

$$\frac{\Delta\omega}{2} = \frac{1}{2\omega_0} (pS_{12} + q(S_{11} + S_{12}))\sigma \quad (\text{A.2})$$

In equation (A.2), S_{ij} are the strain tensor components and vary depending on the porosity of the sample, p and q are the phonon deformation potentials, and ω_0 ($\sim 520\text{cm}^{-1}$) is the Raman peak shift for single crystal Si[154, 155]. For porosities ranging from 70-80%, the stress values of the peaks are calculated in Table A.3. These values reveal the sensitivity to ignition of the PS sample. The intrinsic stress of the PS lies in the range of 35-83MPa, and the stress of the PS

under laser heating that leads to ignition is in the range of 43-123MPa. These values are quite similar and explain why only a small mechanical force can ignite the PS.

Table A.3: Raman spectroscopy results and predicted stress in the sample at several laser power densities and accumulation times.

laser power density (kW/cm ²)	duration (s)	energy density (kJ/cm ²)	peak position (cm ⁻¹)	$\Delta\omega$ (cm ⁻¹)	σ (MPa)
8.10	100	810	510.8	-10.1	52-123
8.10	30	243	512.5	-8.4	43-102
1.62	150	243	511.7	-9.3	48-113
0.16	750	120	512.5	-8.4	43-102
0.16	250	40	514.2	-6.8	35-83

Appendix B

Porous Silicon Velocity Strips: Processing and Additional Characterization

B.1. Preface

Information in this appendix is intended to clarify the processing steps for fabrication of the PS velocity strips presented in Chapter 6. A discussion of the technique used to determine specific surface area of the samples is also discussed. Scanning electron microscope images of the 3:1 PS are presented to demonstrate that the 3:1 and 20:1 samples are of similar thickness. Lastly, additional velocity data of the 20:1 and 3:1 PS- NaClO_4 reactions is presented.

B.2. Porous silicon velocity strip process flow

Figure B.1 shows the process flow for porous silicon (PS) velocity strips. The process begins with a 1-20 $\Omega\text{-cm}$ Si wafer that has 600 nm of low-stress LPCVD Si_3N_4 to serve as an etch mask. In Step 2 the backside Si_3N_4 is removed and a 1700 nm Pt film is sputtered onto the exposed Si. Prior to sputtering Pt, the Si is sputter etched to remove any native oxide. Following Pt deposition, the Pt is annealed in a rapid thermal anneal tool at 350°C for 120s. This promotes adhesion to the Si through formation of a platinum silicide layer. Next, in Step 3b), regions of the Si_3N_4 are removed to expose Si channels where PS will be formed. As shown in Step 3a) “bridges” of Si_3N_4 remain which will form the base layer of the resistive wires used in monitoring the velocity. Step 3 also shows that a gold layer is patterned on the wafer to form the resistive wires. The gold layer is actually composed of a stack of Cr,Pt,Au with thicknesses of 20, 100, and 380 nm respectively. The layers are all deposited using electron beam evaporation. Steps 4a) and b) show the lithographically patterned wires that span the Si channel in a) to form

the 7 resistive wires and 1 igniter wire and are completely removed in all other areas of the Si channel in b). In Step 5, galvanic PS formation occurs as discussed in the primary manuscript. Step 5a) specifically shows that PS undercuts the resistive wire and a continuous PS film is realized along the length of the channel.

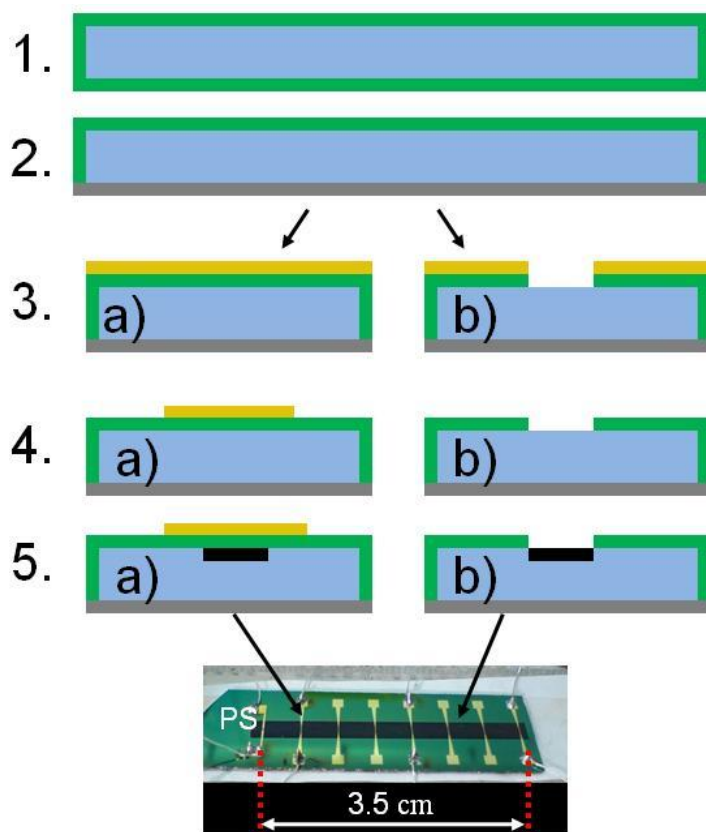


Figure B.1: Process flow for PS velocity strips

B.3. Gas Adsorption Measurements

The gas adsorption measurements to determine pore size and specific surface area were made with a Micromeritics ASAP 2010 using N_2 as the adsorbing gas. For these measurements a PS velocity strip was fabricated as described in the main document. The strip was cleaved into several parts so that it could fit in the narrow diameter glass sample tube of the ASAP 2010. The samples were de-gassed under vacuum and 100°C until the residual gas pressure rise was < 10

$\mu\text{mHg/min}$. De-gassing generally required 6 hours or more. The sample analysis then commenced and the total area of the sample and the pore size distribution were measured. Isotherms of the 3:1 and 20:1 PS are shown in Figure B.2. In Figure B.2 the isotherms have not been normalized for the volume adsorbed.

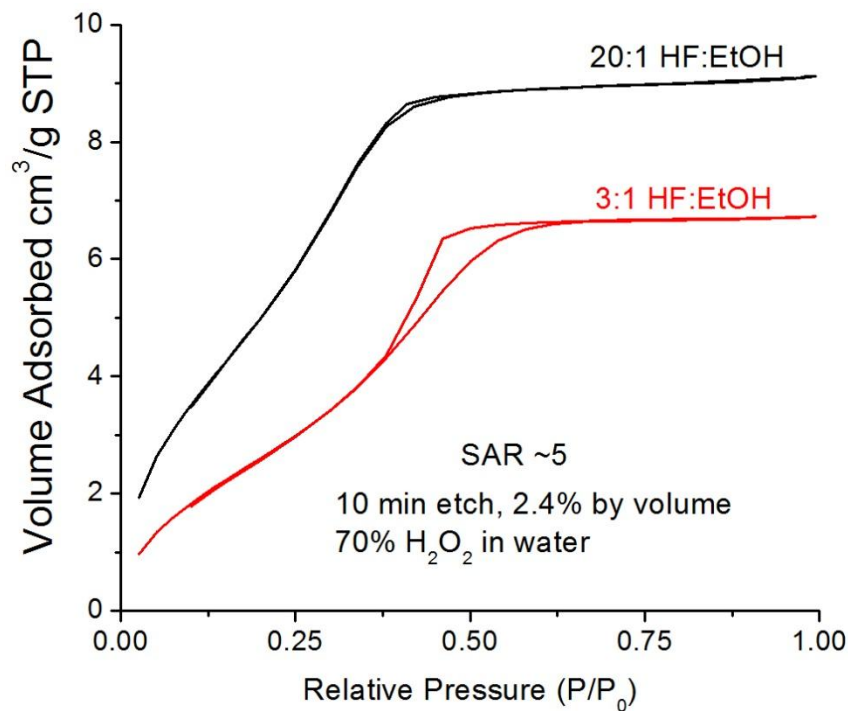


Figure B.2: Gas adsorption isotherms for 20:1 and 3:1 PS.

These isotherms are characteristic of type IV isotherms. The 20:1 sample only shows slight hysteresis, indicative of the smaller pores relative to the 3:1 sample. The surface area is computed using the BET method as is typically employed for PS measurements. The specific surface area (m^2/g) is calculated by destructively measuring the mass of the samples. The mass of the entire velocity strip with PS is recorded using a Mettler Toledo XP26 microbalance. The PS is then removed by immersing the chip in a 5% NaOH solution at room temperature until all PS is removed. The samples are again weighed. The pre-NaOH etch and post-NaOH etch mass

are subtracted to yield the mass of PS. The total surface area of the velocity strip sample is then divided by the mass to give m^2/g .

B.4. Porous Silicon SEM Analysis

As mentioned in Chapter 6, the etch rate is typically independent of HF concentration. Figure B.3 a) and c) are cross section images taken from 3:1 PS. The thickness is within $10\ \mu\text{m}$ of that of the 20:1 sample. Figure B.3 b) is an SEM image of the igniter wire on the 3:1 PS showing excellent adhesion to the PS.

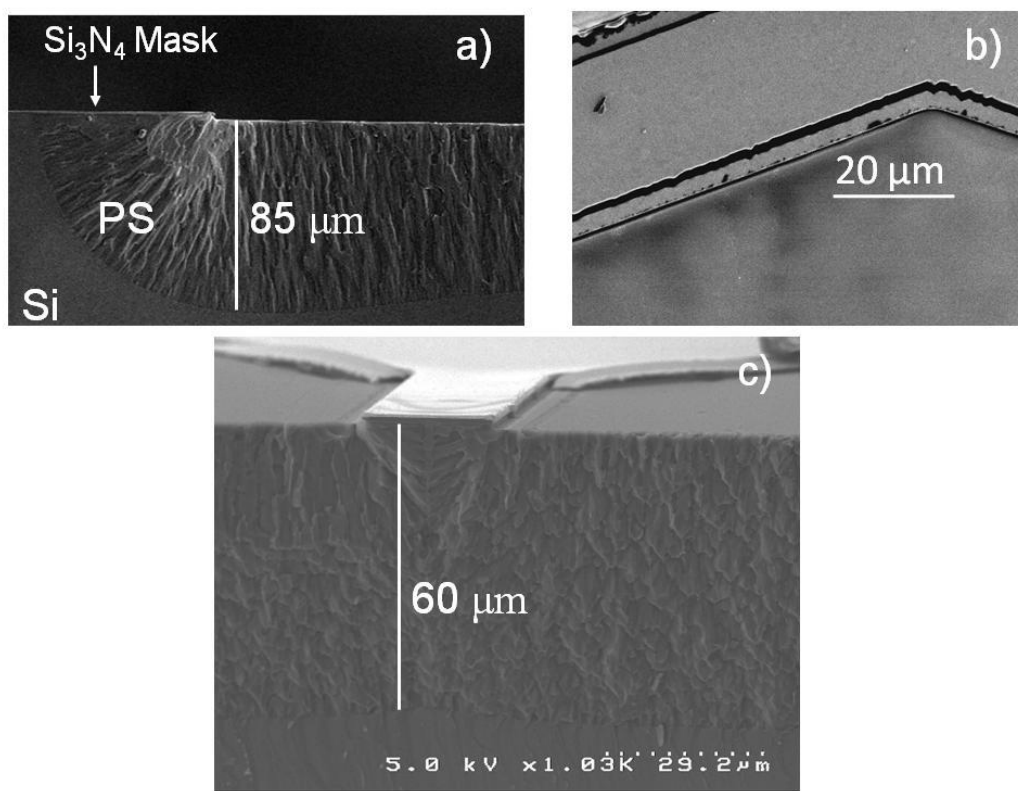


Figure B.3: SEM cross sections of 3:1 PS near the Si_3N_4 etch mask a) and under the igniter wire c). An SEM image of the igniter wire on the PS is shown in b).

B.5. Velocity Analysis

Figure B.4 shows a representative oscilloscope readout (a) and frames (b) from a high speed video of 3:1 PS.

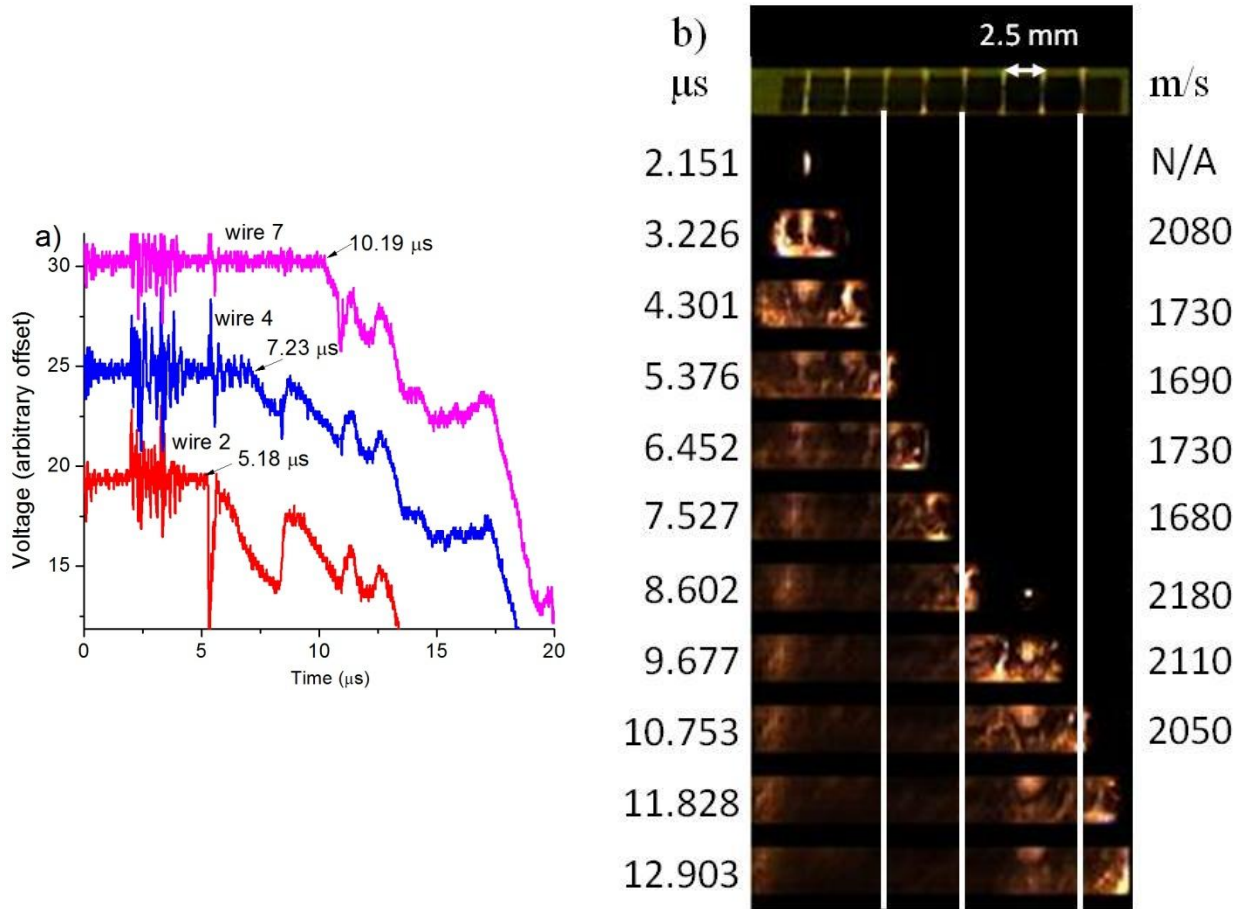


Figure B.4: Oscilloscope data from 3:1 PS (a) and frames from high speed video (b).

In Figure B.4 the voltage across the wires begins to drop very near to the time a flame is observed to across the wire for wires 2 and 7. Wire 4 shows a voltage drop slightly prior to the flame crossing the wire which may result from wire heating prior to the actual breaking of the wire. The velocity measured between wires 2 and 7 is 2490 m/s . While this is higher than the 2050 m/s velocity measured across the entire sample, it compares better to the calculated velocity of 2260 m/s from high speed video analysis between 5.4 and $10.8 \mu\text{s}$. The error in this

sample may also be brought about by the small spacing of resistive wires of 2.5 mm. A larger spacing provides for some inherent averaging of the velocity between wire.

Figure B.5 a) shows the voltage drop for 20:1 PS. The voltage drop is sloped in this sample across each wire prior to a sharp spike in the voltage (the upward spike in the voltage of wire 7 may result from conductance of the flame). The time the voltage slope begins aligns well with the flame front in the frames from the high speed video in Figure B.5 b). This further illustrates that the wires are most likely heating prior to completely breaking as the flame front passes as discussed in the primary manuscript. The velocity of the reaction is not computed at 30.1 μ s as the flame position was unclear.

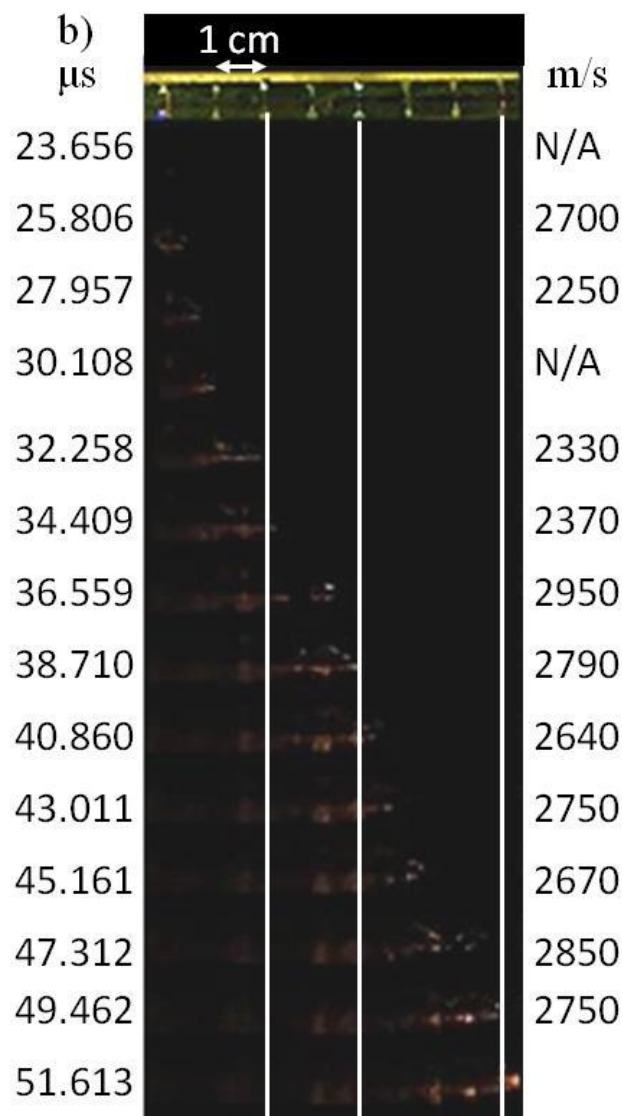
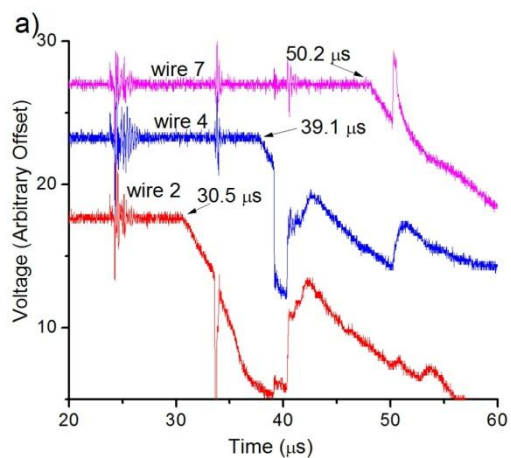


Figure B.5: Oscilloscope data from 20:1 PS (a) and frames from high speed video (b).